Analysis of the optical properties of droplets of different fluids in high-pressure environments by rainbow optical diagnostic

Chanisa Kanjanasakul

Chanisa Kanjanasakul. Analysis of the optical properties of droplets of different fluids in high-pressure environments by rainbow optical diagnostic. Physics [physics]. Normandie Université, 2017. English. NNT : 2017NORMIR22 . tel-01791028v1

HAL Id: tel-01791028
https://theses.hal.science/tel-01791028v1

Submitted on 14 May 2018 (v1), last revised 14 May 2018 (v2)

Normandie Université

THESE

Pour obtenir le diplôme de doctorat

Spécialité Physique & Énergétique

Préparée au sein de INSA de Rouen - Normandie

Analysis of the optical properties of droplets of different fluids in high-pressure environments by rainbow optical diagnostic

Présentée et soutenue par
Chanisa KANJANASAKUL

Thèse soutenue publiquement le 27 Novembre 2017
devant le jury composé de

Mme. Grazia LAMANNA	Directeur de Recherche, Institut für Thermodynamik der Luft- and Raumfahrt, Germany	Rapporteur
M. Jeroen VAN BEECK	Professeur, Von Karman Institute for Fluid dynamics, Belgium	Rapporteur
Mme. Christine MOUNAIM ROUSSELLE	Professeur, PRISME/Polytech'Orléans	Examinateur
M. Guillaume RIBERT	Maître de Conférences, INSA Rouen Normandie - CORIA	Examinateur
M. Frédéric GRISCH	Professeur, INSA Rouen Normandie - CORIA	Directeur de thèse
M. Gérard GRÉHAN	Directeur de Recherche CNRS, UMR 6614 - CORIA	Codirecteur de thèse

Thèse dirigée par Frédéric GRISCH et Gérard GRÉHAN, laboratoire CORIA

INSA INSTITUT NATIONAL DES SCIENCES APPLIQUÉES ROUEN

ED PSIME

UMR 6614 CORIA COMPLEXE DE RECHERCHE INTERPROFESSIONNEL EN AEROTHERMOCHIMIE

ACKNOWLEDGEMENTS

This work would have not been complete without supports from numerous people. First, I would like to express my gratitude to my supervisor, Prof. Frédéric Grisch who gave advice, support and encouragement throughout my PhD. Along the journey of my thesis, he was always the light to guide me the way to the destination when it was dark. Thanks to him for always being kind and nice to me. I would also like to express my appreciation to my co-supervisor, Prof. Gérard Gréhan who also taught and supervised me. His comments, wisdom and insights ultimately made this thesis possible and helped me learn throughout the years in my PhD program. Both are the model of the great teacher and researcher for me. I learned to be positive to overcome all obstacles from them. I am very grateful to their support.

I also would like to express my appreciation to the reviewers, Dr. Grazia Lamanna and Prof. Jeroen Van Beeck, for invaluable comments and advice that go toward completion of this thesis .

Next, I would like to thank to Bijohn Rossow for helping and teaching me the practical work for electronics connections between computer and pressure and temperature controllers.

Next, I would like to express my sincere gratitude to Jacky Galle who helped me a lot for the engineering work during my second and third year. I learned a lot and gained more experience from him. He is also one of the most important person to help this work complete. Next, my thanks go to Benjamin Quevreux, Bruno Mille, Romain Guillot and others mechanical workshop staffs for their quality workmanship. Special mentioned go to Bruno Mille who helped me the last modified of fluid supply system. Thanks to Yohan Manuel Marin Ospina for his technical support and Stanilas Gare for some equipment used in my experiments until my work has been done. Thanks to Prof. Marc Brunel for lending me the laser one of the most important stuff of my work.

Next, I would like to express my sincere appreciation to Dr. Sawitree Seangkeaw who gave me an opportunity to be a Ph.D. student here and always gave me a support and encouragement. Thanks to her for being warm Thai family in Rouen. I also thank Darawan Pejchang to show me the first door of Ph.D position here. She is my first sister here who helped me and gave all support since I arrived until she graduated. She is one of DPST family who stayed with me and understand me when I have any problems. Thanks to Suttiya Chiewudomrat who always listened everything about my life and my work every lunch time. Thanks for her encouragement and being nice sister. Thanks also to Wisuttida Wichitwong, Jantarat Promvongsa and Viphaphorn Srinavawongs for being great family and friend in Rouen.

Next, I would like to thank to Frédéric Berthillier. Thanks for working late together in the last step of our thesis and going back home together.

Finally, special thanks to my family and friends for their love and mental support that make my heart be strong. They filled my heart with happiness. My life in France could not be completed without them.

ABSTRACT

The characterization of the optical properties of fuel drops around the critical pressure is a challenge. The aim of the thesis is to measure the size and the refractive index of fluids under high pressure conditions close to the critical point. For this purpose, an experimental installation of injection of high-pressure drops has been designed. Rainbow refractometry has been developed and adapted to work first on water and ethanol droplets in the pressure range 1-45 bar. Evolutions of their index of refraction with the pressure were obtained. For measurements approaching a fluid near the critical point, ethane was selected because its critical point is 48.7 bar and 32.2°C. Index refractive measurements on liquid drops of ethane were then carried out in the range 40-42 bar and 18-25°C. A measurement of the refractive index of ethane drops then gives a value of 1.255 ± 0.002.

Keywords : Rainbow refractometry, refractive index, droplets, pressure, ethane, water, ethyl alcohol

CONTENTS

LIST OF FIGURES

LIST OF TABLES

NOMENCLATURE

Acronyms

$a.u.$	Arbitrary unit
DA	Direct-coupled amplifier
DWT	Deadweight tester
GA	Gauge
GRT	Global rainbow refractometry technique
$L1$	Lens
$L2$	Lens
LA	Laser
LIF	Laser-induced fluorescence
$M1$	Mirror-1
$M2$	Half-mirror-2
$M3$	Mirror-3
$M4$	Mirror-4
$MDRs$	Morphology-dependent resonances
OCT	Optical coherence tomography
OP	Oil pump
OT	Oil tank

PC	Personal computer
PDA	Phase doppler anemometry
PR	Pen recorder
PT	Phototransistor
PT phase diagram	Pressure-Temperature phase diagram
RC	Reference cell
$S1$	Slit-1
$S2$	Slit-2
$S3$	Slit-3
$S4$	Slit-4
$S5$	Slit-5
$S6$	Slit-6
SC	High-pressure sample cell
SRT	Standard rainbow refractometry technique
SV	Stop valve
TH	Thermostat
WT	Water pump

Constants

A_0	Polynomial dispersion constants $= 2.104025406$
A_1	Polynomial dispersion constants $= -1.456000330 \times 10^{-4}$
A_2	Polynomial dispersion constants $= -9.049135390 \times 10^{-3}$
A_3	Polynomial dispersion constants $= 8.801830992 \times 10^{-3}$

A_4	Polynomial dispersion constants = $8.435237228 \times 10^{-5}$
A_5	Polynomial dispersion constants = $1.681656789 \times 10^{-6}$
A_6	Polynomial dispersion constants = $-1.675425449 \times 10^{-8}$
A_7	Polynomial dispersion constants = $8.326602461 \times 10^{-10}$
R	Ideal gas constant = 8.3144598 J/(K·mol)
π	Mathematical constant = 3.14159265359

Greek Alphabets

δ	Minimum deviation angle - degree (°)
Δ	Angle difference - degree (°)
ε	Scattered angle of droplet around rainbow angle - degree (°)
$\varepsilon_{exp,m^{th}}$	Scattering angle of each maximum intensity position of rainbow's bright pattern, where m is the order of bright pattern (i.e. 1^{st}, 2^{nd}, 3^{rd}, 4^{th}, etc.) - degree (°)
ε_j	Scattering angle from computation corresponding to each $\theta_{1,j}$ - degree (°)
$\varepsilon_{l_a,match}$	Scattering angle from computation corresponding to each n_{gas,l_a} and x_{exp} - degree (°)
θ	Incident angle - degree (°)
θ'	Incident angle - degree (°)
θ''	Emergent angle - degree (°)
θ_1	Incident angle of scattered light to the internal surface normal of the optical window - degree (°)
$\theta_{1,j}$	Incident angle of scattered light to the internal surface normal of the optical window for computation generated from 1.000°-25.000° step by 0.001° where j = 1 to 25000 - degree (°)

$\theta_{1'}$	Incident angle of scattered light to the internal surface normal of the inclined optical window - degree (°)
$\theta_{1',j}$	Computed incident angle of scattered light to the internal surface normal of the inclined optical window corresponding to $\theta_{1,j}$ - degree (°)
θ_2	Refraction angle of the propagating light in optical window - degree (°)
$\theta_{2,j}$	Computed refraction angle of the propagating light in optical window corresponding to each $\theta_{1,j}$ - degree (°)
$\theta_{2'}$	Refraction angle of the propagating light in optical window, assumed to be incline - degree (°)
$\theta_{2',j}$	Computed refraction angle of the propagating light in inclined optical window corresponding to each $\theta_{1',j}$ - degree (°)
θ_3	Refraction angle of the propagating light outside chamber - degree (°)
$\theta_{3,j}$	Computed refraction angle of the propagating light outside chamber corresponding to each $\theta_{1,j}$ - degree (°)
$\theta_{3'}$	Refraction angle of the propagating light outside chamber in case window is assumed to be incline - degree (°)
$\theta_{3',j}$	Computed refraction angle of the propagating light outside chamber corresponding to each $\theta_{1',j}$ - degree (°)
θ_a	Incident angle of incident light to the external surface normal of the optical window - degree (°)
$\theta_{a'}$	Incident angle of incident light ,illuminated by 0.532 μm laser, to the external surface normal of the optical window - degree (°)
$\theta_{a',k}$	Computed incident angle of incident light (0.532 μm) to the external surface normal of the optical window corresponding to each i_k - degree (°)
θ_b	Refraction angle of the propagating light in optical window - degree (°)

$\theta_{b'}$	Refraction angle of the propagating light in optical window - degree (°)
θ_c	Refraction angle of the propagating light in high-pressure test chamber - degree (°)
$\theta_{c'}$	Critical angle - degree (°)
θ_{cr}	Refraction angle of the propagating light in high-pressure test chamber - degree (°)
λ	Wavelength of incident laser - μm
λ_a	Wavelength of incident laser at the atmospheric pressure - μm
λ_b	Wavelength of incident laser in optical window - μm
λ_c	Wavelength of incident laser in high-pressure test chamber - μm
λ_{c,l_a}	Wavelength of incident laser in high-pressure test chamber corresponding to n_{gas,l_a} - μm
λ_{vac}	Wavelength of the radiation in vacuum - μm
σ	Vacuum wavenumber - μm^{-1}
φ	Incident angle on the droplet-air interface - degree (°)
φ_{cr}	Critical angle - degree (°)

Latin Alphabets

a	Particle radius - μm
A	Cross section area of pinhole - cm^2
A'	Vertex angle - degree (°)
A_N	Polynomial dispersion constants, where N = 0 - 7
b_1	Constant to be determined from fitting

b_2	Constant to be determined from fitting
b_3	Constant to be determined from fitting
d	Droplet diameter - μm
D	Pinhole diameter - μm
d'	Sample thickness
d_{cal}	Droplet diameter calculated from volume flow rate and excitation frequency - μm
$d_{fitting}$	Droplet diameter determined from data fitting - μm
$d_{l_a,fit}$	Droplet diameter producing the best fitting-position corresponding to each n_{gas,l_a} - μm
d_{l_a,l_b}	Droplet diameter generated from 101 to 250 step by 1, where $l_b = 1$ to 150, and corresponding to each n_{gas,l_a} - μm
$d_{l_{a-min},fit}$	Droplet diameter corresponding to the smallest associated error ($err_{l_{a-min},fit}$) - μm
$err_{l_a,fit}$	Associated error from fitting corresponding to $d_{l_a,fit}$
$err_{l_{a-min},fit}$	The smallest associated error from fitting
f_G	Excitation frequency - kHz
h	Distance in the x direction from droplets illuminated by laser to a desktop - mm
i	Window inclination angle - degree (°)
I_1	Intensity of light traveling directly to power meter - mW
I_2	Intensity of light passing through the test chamber - mW
i_k	Window inclination angle generated from 0.001° to 5° step by 0.001°, where $k = 1$ to 5000 - degree (°)
j	Integer number

k	Integer number
k	Dimensionless wavelength (Appendix A)
k_1	Distance in the x direction from the point of incidence of 0.532 μm laser at the external surface of window to the first reflection point measured at the atmospheric pressure - mm
k_{11}	Distance in the x direction from the position of 0.532 μm laser at a screen plane to the incident point at the external surface of the optical window measured under high pressure - mm
$k_{11,k}$	Computed distance in the x direction from the position of 0.532 μm laser at a screen plane to the incident point at the external surface of the optical window measured under high pressure corresponding to each i_k - mm
k_{12}	Distance in the x direction from the incident point at the external surface of the optical window to the new reflection point measured under high pressure - mm
$k_{12,k}$	Computed distance in the x direction from the incident point at the external surface of the optical window to the new reflection point measured under high pressure corresponding to each i_k - mm
Δk_1	Distance between reflection point recorded at atmospheric pressure and the new reflection point recorded when air in test chamber is under high-pressure - mm
$\Delta k_{1,exp}$	Distance measured from experiment between reflection point recorded at atmospheric pressure and the new reflection point recorded when air in test chamber is under high-pressure - mm
$\Delta k_{1,k}$	Computed distance between reflection point recorded at atmospheric pressure and the new reflection point recorded when air in test chamber is under high-pressure corresponding to each i_k - mm
$\Delta k_{1,k_{match}}$	Computed distance between reflection point recorded at atmospheric pressure and the new reflection point recorded when air in test chamber is under high-pressure which matches with $\Delta k_{1,exp}$ - mm
Ł	Transversed pathlength - μm

l_1	Distance between point o_2 and point o_1 - mm
l_2	Distance between droplets illuminated by laser and point o_2 - mm
l_3	Perpendicular distance from droplets illuminated by laser to the internal surface of the inclined optical window - mm
l_4	Distance from droplets to the incident point of scattered light at the internal surface of the inclined optical window - mm
$l_{4,j}$	Distance from droplets to the incident point of scattered light at internal surface of the inclined optical window corresponding to each $\theta_{1,j}$ - mm
l_5	Distance from the incident point of scattered light at window's internal surface to the point of scattered light entering to air outside the test chamber - mm
$l_{5,j}$	Computed distance from the incident point of scattered light at window's internal surface to the point of scattered light entering to air outside the test chamber corresponding to each $\theta_{2',j}$ - mm
l_a	Integer number from 1 to 800
l_b	Integer number from 1 to 150
$Ł_j$	Path of light where j is integer number - μm
m	Order of bright pattern (i.e. 1^{st}, 2^{nd}, 3^{rd}, 4^{th}, etc.)
M	Molar mass - grams per mole
m_{air}	Mass of the air - grams
m_{ethane}	Mass of the ethane - grams
m_{gas}	Total mass of the gas - grams
n	Amount of substance - moles
$n_{632.8}$	Absolute refractive index of ethane for the wavelength 632.8 nm
n_{abs}	Absolute refractive index of liquid droplet

$n_{air,1}$	Absolute refractive index of air at atmospheric pressure
$n_{air,P}$	Absolute refractive index of air in the test chamber related to the pressure in the chamber
n_{ethane}	Absolute refractive index of ethane droplet
$n_{ethane,P}$	Absolute refractive index of ethane droplet under high-pressure
n'_{ethane,l_a}	Computed relative refractive index of ethane for simulation corresponding to each n_{gas,l_a}
$n'_{ethane,l_{a-min}}$	Computed relative refractive index of ethane corresponding to the smallest associated error $(err_{l_{a-min},fit})$
$n'_{ethane,P}$	Relative refractive index of ethane droplet under high-pressure
$n_{ethane-vapor,P}$	Absolute refractive index of ethane vapor under high-pressure
n_{gas,l_a}	Absolute refractive index of gas generated from 1.0001 to 1.0800 step by 0.0001, where $l_a = 1$ to 800
$n_{gas,l_{a-min}}$	Absolute refractive index of gas providing the smallest associated error $(err_{l_{a-min},fit})$
$n_{gas,P}$	Absolute refractive index of gas in the test chamber related to the pressure in the chamber
n_{liquid}	Absolute refractive index of liquid droplet
$n_{liquid,P}$	Absolute refractive index of liquid droplet under high-pressure
$n'_{liquid,P}$	Relative refractive index of liquid droplet under high-pressure
n_{rela}	Relative refractive index of liquid droplet
n_{water}	Absolute refractive index of water
$n'_{water,P}$	Absolute refractive index of water under high-pressure
n_{win}	Absolute refractive index of the optical window

o_1	Droplet projection point on external surface of the inclined optical window
o_2	Droplet projection point on internal surface of the inclined optical window
p	Van de Hulst's notation
P	Pressure of gas - Pa
P_{air}	Air pressure - bar
P_{AIR}	Air pressure - Pa
P_{cr}	Critical pressure - bar
P_{inside}	Gas pressure inside the test chamber - bar
P_{liquid}	Liquid pressure - bar
P_{max}	Maximum pressure reached from all experiments - bar
P_{tp}	Triple-point pressure - bar
ΔP	Difference between air pressure and liquid pressure - bar
r	Distance between the point of incidence of 0.532 μm laser at the external surface of the optical window and the first reflection point at the external surface of the optical window - mm
T	Temperature - °C
T_1	First transmission
T_2	Second transmission
T_3	Third transmission
T_4	Fourth transmission
T_{air}	Temperature of air - °C
$T_{air,inside}$	Temperature of air inside chamber - °C

$T_{air1,inside}$	Temperature of air inside chamber measured by using thermocouple-1 - °C
$T_{air2,inside}$	Temperature of air inside chamber measured by using thermocouple-2 - °C
$T_{air3,inside}$	Temperature of air inside chamber measured by using thermocouple-3 - °C
$T_{air,outside}$	Temperature of air outside chamber - °C
T_{cr}	Critical temperature - °C
$T_{ethanol}$	Temperature of ethanol - °C
T_{inside}	Temperature of gas inside the test chamber - °C
T_{tp}	Triple-point temperature - °C
T_{wall}	Temperature of chamber wall - °C
T_{water}	Temperature of water - °C
u_D	Jet velocity in - cm/min
V	Volume of gas - m^3
$\dot{V}$	Volume flow rate in ml/min
v_1	Speed of light in medium 1 - m/s^2
v_2	Speed of light in medium 2 - m/s^2
$v_{air,P}$	Speed of light in high-pressure air - m/s^2
$v_{liquid,P}$	Speed of light in liquid droplet - m/s^2
x	Concentration of ethane vapor in the test chamber - %
x_1	Distance in the x direction from droplets illuminated by laser to the position of scattered light at the internal surface of the optical window - mm
$x_{1,j}$	Computed distance in the x direction from droplets illuminated by laser to the position of scattered light at the internal surface of the optical window corresponding to each $\theta_{1,j}$ - mm

x_{123}	Distance in the x direction from droplets illuminated by laser to the rainbow signal - mm
$x_{123,exp}$	Distance in the x direction from droplets illuminated by laser to the each peak of rainbow signal measured from experiment - mm
$x_{123,j}$	Computed distance in the x direction from droplets illuminated by laser to the rainbow signal corresponding to each $\theta_{1,j}$ - mm
x_2	Distance in the x direction from the position of scattered light at the internal surface of the optical window to the position of scattered light at the external surface of the optical window - mm
$x_{2,j}$	Computed distance in the x direction from the position of scattered light at the internal surface of the optical window to the position of scattered light at the external surface of the optical window corresponding to each $\theta_{1,j}$ - mm
x_3	Distance in the x direction from the position of scattered light at the external surface of the optical window to the rainbow signal position - mm
$x_{3,j}$	Computed distance in the x direction from the position of scattered light at the external surface of at optical window to the rainbow signal position corresponding to each $\theta_{1,j}$ - mm
x_b	Distance in the x direction from the point of incidence of 0.532 μm laser at the external surface of the optical window to the position of incident light at the internal surface of the optical window - mm
x_c	Distance in the x direction from the position of incident light at the internal surface of the optical window to droplets - mm
x_{exp}	Distance in the x direction from the point of incidence of 0.532 μm laser at the external surface of the optical window to rainbow signal position - mm
$x_{exp,m^{th}}$	Distance in the x direction from the point of incidence of 0.532 μm laser at the external surface of the optical window to the middle of each bright pattern, where m is the order of bright pattern (i.e. 1^{st}, 2^{nd}, 3^{rd}, 4^{th}, etc.) - mm

x_h	Distance in the x direction from the rainbow signal position to a desktop - mm
x_j	Computed distance in the x direction from the point of incidence of 0.532 μm laser at the external surface of the optical window to rainbow signal position corresponding to each $\theta_{1,j}$ - mm
x_{n1}	Distance in the x direction from the point of incidence of 0.532 μm laser at the external surface of the optical window to the point of incidence of 0.6328 μm He-Ne laser at the external surface of the optical window - mm
x_{n2}	Distance in the x direction from He-Ne laser beam to rainbow signal position - mm
y	Distance in the y direction from the droplets to the screen - mm
y_1	Distance in the y direction from droplets to the internal surface of the optical window - mm
$y_{1'}$	Distance in the y direction from droplets to the incident point of scattered light at the internal surface of the inclined optical window - mm
$y_{1',j}$	Computed distance in the y direction from droplets to the incident point of scattered light at the internal surface of the inclined optical window corresponding to each $\theta_{1,j}$ - mm
y_2	Thickness of the optical window - mm
$y_{2'}$	Distance in the y direction from the incident point of scattered light at the internal surface of the inclined optical window to the point of scattered light entering to air outside the test chamber - mm
$y_{2',j}$	Computed distance in the y direction from the incident point of scattered light at the internal surface of the inclined optical window to the point of scattered light entering to air outside the test chamber corresponding to each $\theta_{1,j}$ - mm
y_3	Distance in the y direction from the external surface of the optical window to the screen - mm

$y_{3'}$	Distance in the y direction from the point of scattered light entering to air outside the test chamber to a screen plane - mm
$y_{3',j}$	Computed distance in the y direction from the point of scattered light entering to air outside the test chamber to a screen plane corresponding to each $\theta_{1,j}$ - mm
Δy	Distance of window displacement in the y direction from center of window's external surface when it was at atmospheric pressure to point o_1 - mm
Δz	Distance in the y direction from the point of incident light of 0.532 μm laser at an window's external surface to a point o_1 - mm
Δz_k	Computed distance in the y direction from the point of incident light of 0.532 μm laser at an window's external surface to a point o_1 corresponding to each i_k - mm

CHAPTER 1

Introduction

During the last decades, the internal combustion engines of cars were developed in order to improve the efficiency of combustion as well as to reduce the emission of pollutants. In particular, the efficiency of combustion depends mainly on the evaporation of fuel droplet and the mixing between fuel in gaseous phase and oxidizer. One approach to improve the efficiency of combustion is to increase the fuel injection pressure in order to have a better atomization of liquid fuel and so a better evaporation and fuel/air mixing. When the pressure increases, the liquid fuel atomization can occur more efficiently which will reduce droplet size and then will improve the evaporation rate.

An alternative way to increase mixing between fuel vapor and oxidizer is to inject the fuel at a pressure and temperature exceeding the critical state. In this state, supercritical fluids has smaller intermolecular force than the kinetic forces, leading to a high diffusion coefficient, fast heat, and mass transport [11]. Accordingly, it can provide a better mixing process.

Nevertheless, the transition between sub-critical to supercritical conditions has not been well understood yet, especially for multicomponent liquids such as the classical gasoline and diesel fuels. Therefore, it will be necessary to get quantitative measurements to study the physical properties of droplets. Thus measurements in transcritical condition must be performed on the injected droplets at sub-critical conditions with the transition to supercritical conditions. To characterize fuel droplet under transcritical condition, the refractive index is one of the significant properties possible to be measured. Therefore, the development of an optical technique to measure the refractive index under the transcritical condition is required.

All previous refractive index measurements of liquids under high pressure have been performed on liquids in a container in high pressure cell. Unfortunately, none of previous refractive index measurements were performed on free-falling droplets in high pressure condition. For that, the rainbow refractometry method is selected as it is able to measure refractive index on moving small droplets.

In the current thesis, a focus on the possibility of refractive index measurements on moving droplets under high pressure conditions, still being in sub-critical condition, was investigated. It has been decided to adapt global rainbow refractometry for measurements under high pressure conditions to improve the evident potential of this optical measurement technique. Until now, the rainbow refractometry has never been used for measurements under high-pressure before. This work is original because it is the first time that measurements in very extreme pressure will be performed with such method.

This thesis is structured as follow: Chapter 2 provides basic background on the characteristics of fluid in sub-critical and critical states as well as a description of the physics of the global rainbow refractometry diagnostic. Chapter 3 introduces the validation of refractive index measurements on free-falling water and ethanol droplets under high pressure. Chapter 4 presents optical measurements on free-falling liquid ethane under high pressure up to 50 bar. The conclusions of this work is given in Chapter 5. Finally, suggestions for the future work are stated in Chapter 6.

CHAPTER 2

Background

2.1 An introduction to sub-, critical and super-critical states

The critical state is one of the thermodynamic state of substance. This state is the end point of the liquid-gas equilibrium curve where liquid and gas cannot be distinguished [12]. The temperature and pressure in this state were defined as critical temperature (T_{cr}) and critical pressure (P_{cr}), respectively. To describe this state, we begin with the physical states of substance. Pure substances can exist in three phases which can be a gas, liquid or solid. These physical states can be presented in a pressure-temperature phase diagram (PT phase diagram) as shown in Figure 2.1. From the PT phase diagram, the red line is the sublimation line representing the transition between vapor and solid states. This line divides solid and vapor phases. The point representing the end of this line is the triple point in which all three phases coexist. The green line is the fusion line representing the transition between solid and liquid phases and also separates these two phases. The blue line is the vaporization line. It represents the transition between vapor and liquid phases as well as divides liquid and vapor phases. This line ends at the critical point where the phase separation between liquid and gas vanishes. If the pressure and temperature exceed this critical point, the substance will become a super-critical fluid. The liquid phase and gaseous phase become similar to each other and eventually become indistinguishable.

The aim of this work is to study liquid droplets in thermodynamic conditions extending from sub-critical to supercritical conditions. Therefore, ethane is selected in this study because this molecule offers promising conditions to reach easily the critical state. Indeed, the critical state of ethane is at a pressure of 48.72 bar and a temperature of 32.17°C. It is not elevated compared to those of water, a critical pressure of 221 bar and critical temperature of 374°C. Since we selected ethane for this study, the values of pressure and temperature for the thermodynamic states are indicated in the PT phase diagram in Figure 2.1.

To illustrate the behavior of fluid approaching the supercritical conditions, Figure 2.2 shows the phase of the three states from sub- to super-critical conditions. Figure 2.2(a) shows ethane under sub-critical conditions. In this figure, the liquid and gaseous phases can be distinguished. Figure 2.2(b) shows the ethane at critical state. At this point, the liquid becomes opalescence. After passing this state, ethane will be in the supercritical state and it will be transparent as can be seen in Figure 2.2(c). In this state, the distinction between liquid and gaseous ethane disappears.

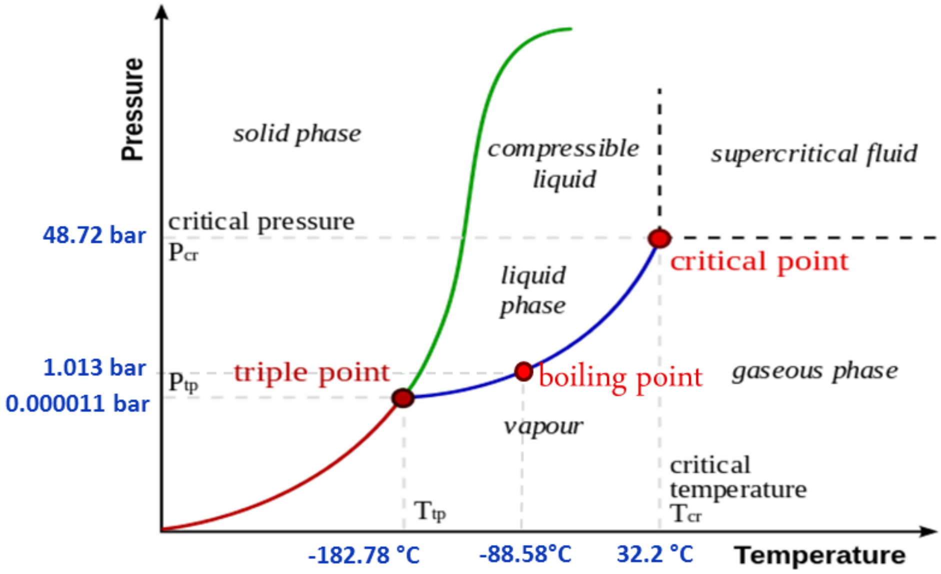

Figure 2.1: Pressure-temperature phase diagram of pure substance indicated the values of pressure and temperature for ethane [1]

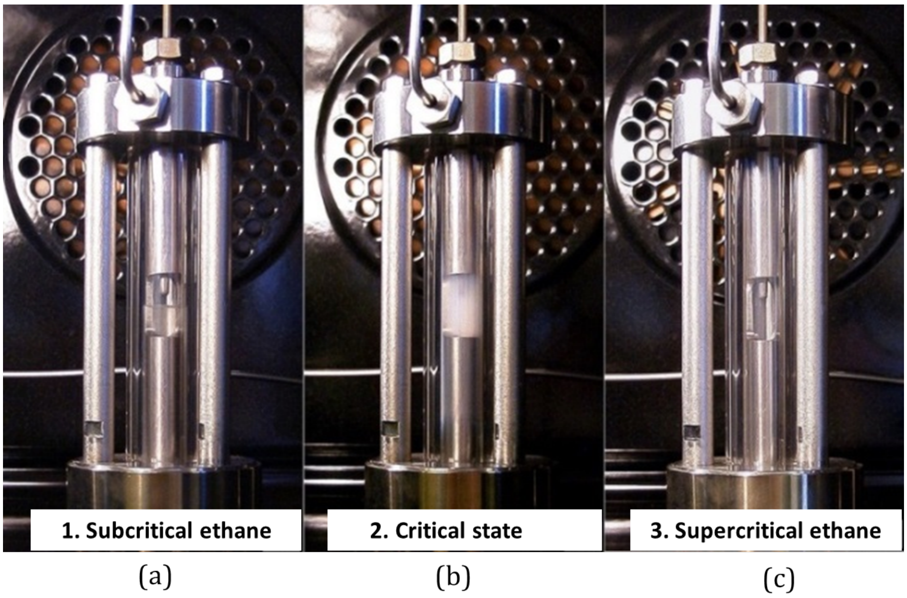

(a) (b) (c)

Figure 2.2: Image of ethane at three different thermodynamic states (a) Subcritical state (b) Critical state (c) Supercritical state [2]

2.2 Previous studies of refractive index measurements on liquid under high pressure

The study of the refractive index dependence with pressure started at the early 20th century [7]. Many optical techniques have been used to carry out the refractive index measurements under high pressure (a description of each technique follows in the Note). In the early studies, the prism minimum deviation method has been used [7, 13]. For this technique, the liquid is confined between optical windows in quartz, constituting a prism, this one being installed in a pressure vessel. The optical instruments for measurements such as collimator and telescope were placed outside in an environment at atmospheric pressure. Poulter et al., 1932 [13] used the prism minimum deviation method in which the windows constituted a 30° prism. They studied the refractive index of paraffin oil and glycerine up to 13765 bar and up to 7308 bar, respectively. After that, Rosen, 1947 [7] studied the refractive indices of ethyl alcohol, water and mixtures of water and alcohol at 25°C and pressure up to 1765 bar, by using a similar method with the windows forming a 51° prism.

Later, another studies on refractive index measurements at elevated pressure applying various types of interferometers were performed. Waxler and Weir, 1963 [14] and Waxler et al., 1964 [15], applied the interferometric method based on the Fabry-Perot principle to study the effect of pressure and temperature on the refractive indices of benzene, carbon tetrachloride and water. In these measurements, the interferometer was enclosed in the pressure vessel so that the distortion of the optical window at elevated pressure can be neglected. They have been carried out measurements at pressure up to 1100 bar and temperature up to 55°C with an accuracy on the refractive index of ± 0.0001. Stanley, 1971 [16] also applied the Fabry-Perot interferometer to study the refractive index of distilled water for temperature in range of 1-60°C and pressure up to 1373 bar to supplement the water results of Rosen [7], Waxler and Weir [14] and Waxler et al. [15]. The accuracy of his refractive index measurement is ±0.00006, typically one decade better. Later, Takagi and Teranishi, 1982 [3] used a Michelson-type interferometer to measure refractive indices of benzene, toluene, chlorobenzene and nitrobenzene. They performed measurements at temperature of 20, 30 and 40°C and pressure up to 500 bar. They determined refractive indices at lower pressure than other authors, from 1 to 500 bar with a step of 50 bar. The estimated accuracy of this work is ± 0.00008.

After that, various studies of refractive index dependence with pressure of liquid under very high pressure from 3000-40000 bar were investigated. Recently, Wang et al., 2016 [17] demonstrated that the refractive index of polydimethylsiloxane liquid increased dramatically with pressure up to 40000 bar by using optical coherence tomography.

For all these studies:

1. The liquid is confined in a container in a test chamber under high pressure.
2. The shape of liquid is perfectly defined by the container (prism, cylinder, etc.).

These techniques were performed not on individual droplets but on a configuration of liquid contained in a cell with a very well definition of the shape.

Note:

1. The prism minimum deviation method provides the potential to measure refractive index. This technique was applied to measure liquid refractive index under high pressure in the works of Poulter et al., Lyons and Poindexter, and Rosen. The basic concept of this technique is to measure the minimum deviation angle (δ) of the light entering through a prism containing liquid under high pressure. The minimum deviation angle occurs when $\theta' = \theta''$. The schematic diagram of the prism minimum deviation method is shown in Figure 2.3. Knowing minimum deviation, the refractive index can be determined as the minimum deviation that depends on the refractive index of liquid inside the prism.

2. Interferometric methods:

2.1 The Fabry-Perot interferometer, is made of two partially reflective surfaces separated by a small gap that creates the interference fringes. The concept of this method is that the light is propagating with partially reflecting mirrors, firstly refracted at the first mirror and then transmitted through the space between the two mirrors. When the light travels to the second mirror, the majority of the light is reflected and the residual fraction of the light is transmitted. These mirrors allows subsequent reflections and transmissions as can be seen in Figure 2.4. After that, many waves interfere together. In the work of Stanley [16], the interferometer was installed in a high-pressure vessel. The gap between two surfaces was filled with liquid sample. The light source and lens were placed outside the high-pressure vessel. The change of the refractive index of liquid in this space induces the interference fringes. Hence, the refractive index can be determined from the analysis of the interference fringes.

2.2 The Michelson-type interferometer is also a method producing the interference fringes. In this technique, a monochromatic beam travels to a beam splitter separating the beam into two beams at 90°C from each other. The beams travel to mirrors. After that, they are reflected and brought back together creating interferences. Takagi and Teranishi [3] applied this technique to measure refractive index of liquid under high pressure. The schematic of Michelson-type interferometer in their study is shown in Figure 2.5. The laser beam was separated by half-mirror (M2); one of the beams was passed through a reference cell (RC), and another one was passed through a high-pressure sample cell (SC). The beam passing through the reference cell was reflected by a mirror M1. The beam passing through a high-pressure sample cell was reflected by a mirror M3. After reflected by mirrors, these two beams passed again through these cells and then they were brought back together. Lastly, interference pattern results. The change of the refractive index of liquid in the sample cell modifies the interference pattern. Therefore, the observation of this interference pattern can be used to determine refractive index of liquid under high pressure

3. Optical coherence tomography (OCT) is a non invasive, high-resolution, and a cross-section imaging technique. This technique uses the interference signals generated by the backscattered light from a sample and a reference mirror to obtain the structural information of the sample at various depths [17]. This technique provides

the possibility to measure optical path length which is $n_{liquid} \times d'$ where n_{liquid} is refractive index and d' is a sample thickness.

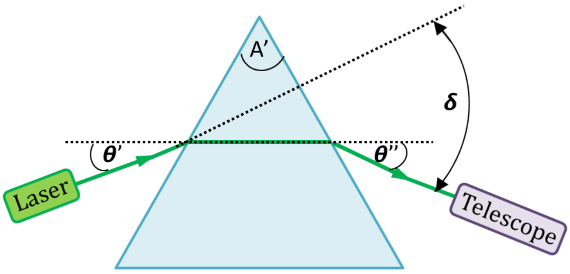

Figure 2.3: Schematic diagram of the prism minimum deviation method

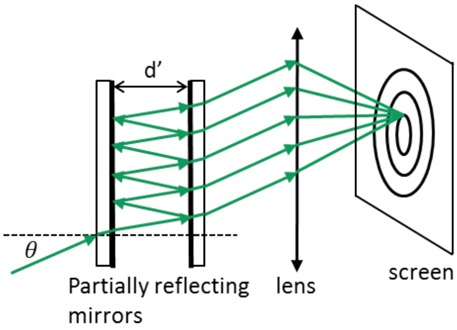

Figure 2.4: Schematic diagram of the Fabry-Perot interferometer

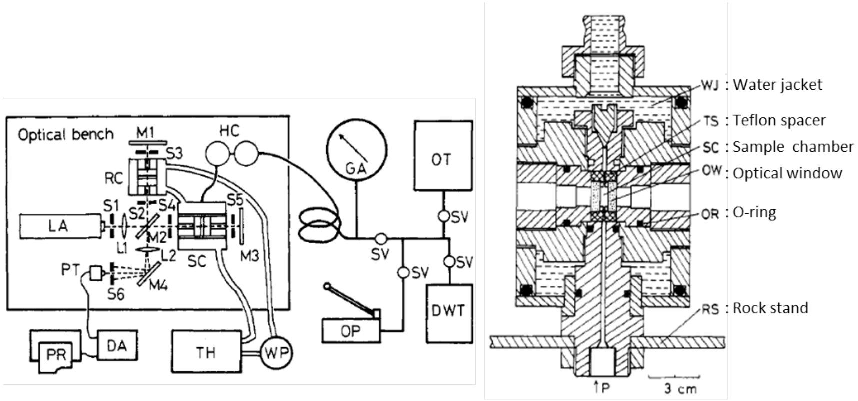

(a) (b)

Figure 2.5: (a) Diagram of the refractive index measurement apparatus: (LA) He-Ne laser, 632 nm, 1.5 mW; (RC) reference cell; (SC) sample cell; (M1,M4) mirrors; (L1,L2) lenses; (S1,S6) slits; (HC) H_g cylinder; (PT) phototransistor; (PR) pen recorder; (DA) dc amplifier; (TH) thermostat; (WP) water pump; (GA) gauge; (OT) oil tank; (SV) stop valve; (OP) oil pump; (DWT) deadweight tester. (b) High-pressure sample cell [3]

2.3 Optical characterization of moving droplets

A variety of optical diagnostics measurement can be used for characterizing moving droplets such as laser-induced fluorescence (LIF), phase doppler anemometry (PDA), morphology-dependent resonances (MDRs), etc. Each technique has advantages and limitations depending on its own basic principle.

Laser-induced fluorescence (LIF): The use of LIF in liquid droplets is based on the excitation of a fluorescent tracer that delivers a fluorescence signal depending of various physical parameters such as temperature and species concentration. Fluorescence denotes the radiation emitted by an atom or a molecule when it relaxes by spontaneous emission of a photon from higher to a lower energy level. In the laser-induced fluorescence process, the upper energy level is populated using laser excitation with a wavelength tuned to a resonance between the excited state and a discrete lower state [18]. For the fluorescence spectra observation of liquid fuel, an organic fluorescent dye such as rhodamine B that is usually used as a fluorescent temperature sensor is dissolved in the liquid fuel. Accordingly, this technique can be applied for temperature measurements on liquid droplets. However, adding a molecular tracer can change the critical properties of the liquid fuel. In this case, it is then required to study the significance of this effect. In addition, the fluorescence depends on many parameters (temperature, pressure and chemical composition), accordingly, calibrations will be very difficult near critical conditions.

Phase doppler anemometry (PDA): PDA is a non intrusive technique that can be used to simultaneously measure droplet velocity and size assuming the particle is spherical. PDA measurement is performed at the intersection of two laser beams, forming an interference fringe pattern. The injected droplet passes through the fringe pattern. For measurements, the detectors are placed off-axis location focusing scattered light onto multiple detectors (at least two detectors). Finally, the Doppler burst is derived. The frequency of the signal is used to determine the droplet's velocity and the phase shift between the Doppler signals from two detectors is related to the droplet's diameter as well as refractive index. Nevertheless, the refractive index accuracy measured by PDA is limited to the second digit of the refractive index.

Morphology dependent resonances (MDRs): MDRs is based on a phenomenon of total internal reflection of light inside a spherical droplet. The MDRs occurs under three conditions which are: first, the incident angle on the droplet-air interface (φ) is greater than the critical angle $\varphi_{cr} = sin^{-1}(1/n_{liquid})$ where n_{liquid} is the refractive index of droplet; second, path of light in droplet is closed; third, transversed pathlength (L) is an integral multiple of the wavelength ($L = \Sigma L_j = k\lambda$) where j and k are integer numbers and λ is the wavelength. Figure 2.6 shows the schematic diagram of the resonance in the sphere which is the basis of this technique. Based on the MDRs, it provides the resonance peaks which can be observed in both the elastic and inelastic spectra such as fluorescence and stimulated Raman scattering from microdroplets. The resonance peak in the scattering spectra gives the possibility to determine droplet size and evaporation rate (size change). MDRs can be used to measure the change of radius of droplet as small as $10^{-5}a$ where a is the particle radius [19]. This technique has a limitation because the measurement droplet must be perfectly spherical.

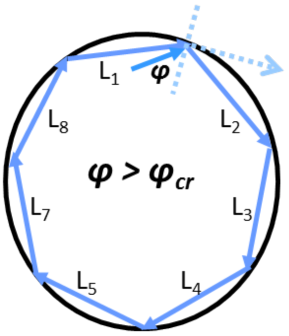

Figure 2.6: The path of light occurs a resonance in a sphere droplet

Rainbow refractometry: The rainbow refractometry is a non intrusive technique. The basic concept of this technique is to measure the scattering light by a droplet around rainbow region, called rainbow signal. The rainbow signal depends on the refractive index and the size of droplet. The rainbow location is sensitive to the refractive index. This technique can be applied for the measurement of single droplet, monodispersed droplets as well as spray droplets. In the last situation, the measurement on a spray using the global rainbow refractometry (GRT) technique can eliminate non-sphericity effects [20].

For the current study, the measurement of moving droplets under high pressure from sub- to critical condition will be performed. The rainbow refractometry has been selected because this is a promising non intrusive technique which is able to measure refractive index with accuracy as well as the size of droplet. By this way, the access to the refractive index will be a mean to deduce also the temperature during the evaporation process. Moreover, it is also possible to adapt this technique to follow the large change of refractive index due to the change of the physical properties near critical condition. The description and background physics of this technique is presented in the next sections.

2.4 The rainbow refractometry for the measurement on liquid moving droplets

2.4.1 Background physics of rainbow

Rainbow refractometry is one of the rare optical measurement techniques that provides an ability to characterize droplets. The background physics of this technique is the same as a rainbow phenomena in the sky as shown in Figure 2.7. In 1637, Ren Descartes was the first to introduce a physical explanation of the rainbow phenomena considering the light passing through a single droplet [21]. For a basic explanation, the parallel rays of light impinge on a homogeneous spherical droplet, some of them are reflected at droplet surface but some of them enter into the droplet. The light

entering into the droplet is firstly refracted due to the change of refractive index and then, reflection/reflections inside the droplet occur. After reflection/reflections, the light is refracted once more when exiting from the droplet. The rainbow is an extremum deviation of these light rays. The primary and secondary rainbows are defined as the extremum deviation of rays having one time internal reflection and two times internal reflections, respectively. Figure 2.7 shows the path of light having one time internal reflection and the light reflected at the external water droplet surface. They are defined as the internally reflected ray and the externally reflected ray, respectively. To study the geometrical optics, it might be best to define the rays leaving the particle with the Van de Hulst's notation,1957 [22]:
p=0 for the externally reflected ray,
p=1 for the ray refracted twice,
p=2 for the ray experimenting one internal reflection and two refractions (the internally reflected ray),
p=3 for the ray experimenting two internal reflections and two refractions,
p=k for the ray experimenting k -1 internal reflections and two refractions.

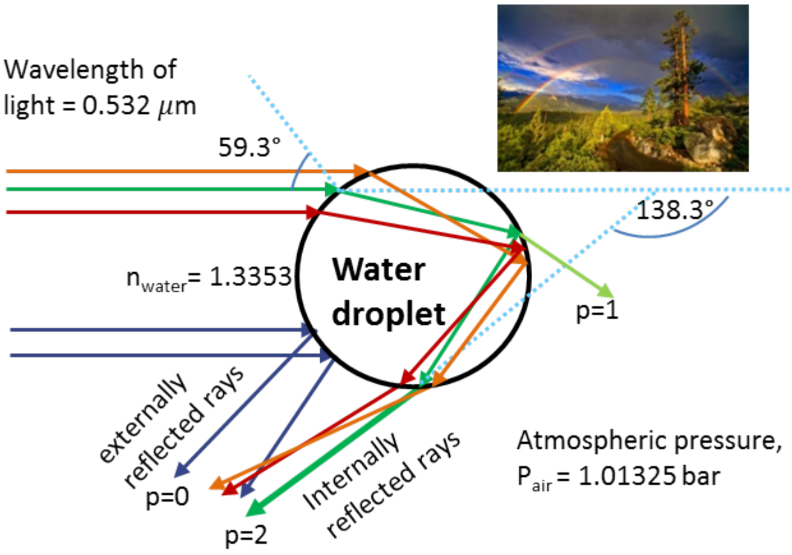

Figure 2.7: The path of light rays passing through water droplet

A lot of studies have been realized on the rainbow, especially for water. In the sky, the primary and the secondary rainbows due to chromatic dispersion in water droplets can be observed. The area between the primary and the secondary rainbows is called Alexander's dark band where the intensity is very small in comparison with primary and secondary rainbows and mainly dominated by external reflection [23]. The rainbow angle is determined from the extremum of the angular deviation between the incident and emergent rays after internal reflections as the rainbow angle is the supplementary angle; 180° − extremum scattering angle [4]. For rainbow in nature, it is the angle of the elevation relative to the sun-observer line. The rainbow angle for the primary rainbow and secondary rainbows are about 42° and 51° , respectively. Figure 2.8 shows the internally reflected rays (p=2) on water droplet which have been deviated. The extremum scattering angle is the minimum scattering angle for the one internal reflection (p=2). The ray of the minimum deviation for p=2 is called the rainbow ray or Descartes ray and its angular position is defined as the geometrical rainbow angle (θ_{rg}). The geometric rainbow angle for water is about 138°. After the exit of the internally reflected rays (p=2) from a droplet, interference between these rays occurs. Thus, destructive and constructive interferences occur due to the phase difference forming supernumerary bows inside the primary rainbow.

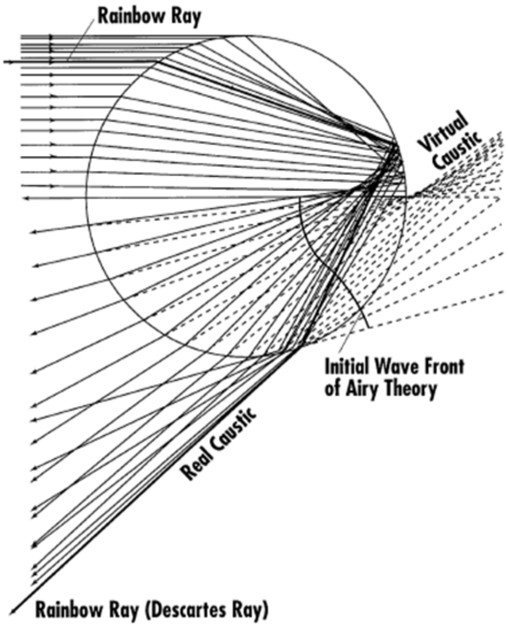

Figure 2.8: The envelope of a ray system (from Adam [4])

In 1838, George B. Airy developed the extension of the geometrical optics. On the basic of wave theory, Airy takes into account the diffraction by using Huygens' principle on the propagation of a wave front. After that, Airy's theory is able to predict the rainbow shape and for the first time, to provide the gradual fading of rainbow within Alexander's dark band, taking into account the finite droplet size. However, Airy's theory is a scalar theory, all the effects due to the vector aspect were not taken into account. The predicted rainbow pattern from Airy's theory is accurate only for the position which is close to Descartes minimum scattering angle or rainbow angle (the more distance from rainbow angle, the less accurate of rainbow position). Later, Lorenz-Mie theory is able to provide the exact position for all the rainbow orders. In 1890, Lorenz introduced the result of light scattering by a transparent sphere in the frame work of Ether theory. Later, Mie (1908) rediscovered the same result in the framework of Maxwell's electromagnetic theory. Mie derived a solution for the scattering of an incident electromagnetic plane wave by a homogeneous spherical particle by solving Maxwell equations. This solution consists of infinite series of terms where all kinds of interaction are mixed together. As Lorenz and Mie obtained the same result, it can be called Lorenz-Mie theory. After that, Debye (1909) also introduced a solution consisting of an infinite series of terms but each kind of interaction can be independently quantified. The determination of the scattering of light by a spherical particle around rainbow angle from Lorenz-Mie's and Debye's theory is very accurate but time consuming [23]. Later, Nussenzvieg, 1969 developed the complex angular momentum method and applied it to the Debye expansion. Following this, he introduced the approximation depending on the angular region under study and on the kind of ray of interest.

Considering Figure 2.7 again, there is not only the interference between internally reflected rays (p=2) but also the interference between externally reflected rays and the other orders of internally reflected rays creating high frequency oscillations superimposed on the Airy fringes. It is called the ripple structure. Lorenz-Mie and Debye theory can provide a determination of the rainbow pattern including all the aspects of ripple structure. Nevertheless, Nussenzvieg theory is limited to the p=0 contribution. An example of rainbow pattern according to the Lorenz-Mie theory is shown in Figure 2.9.

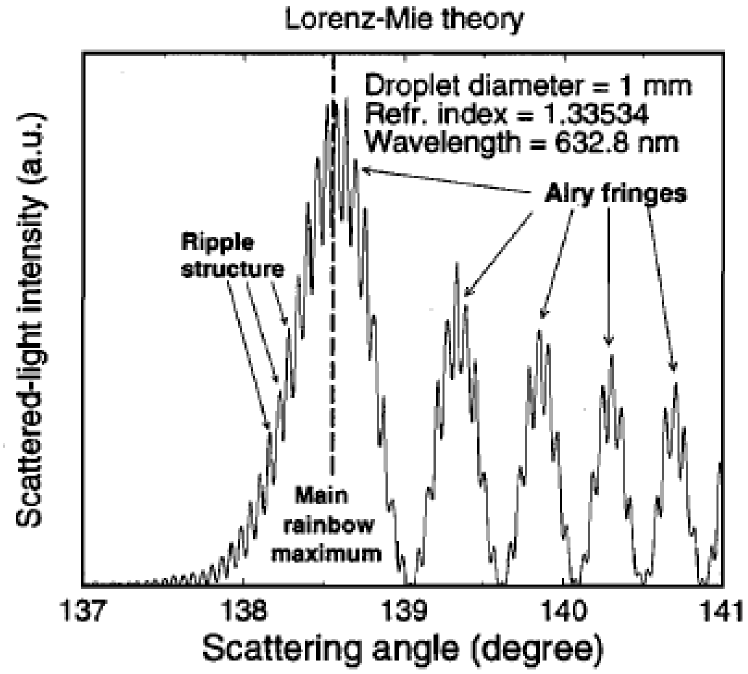

Figure 2.9: The monochromatic rainbow according to the Lorenz-Mie theory (from van Beeck [5]).

2.4.2 Rainbow refractometry

The rainbow refractometry enables the measurement of size and refractive index (hence temperature and species composition) of a transparent spherical particle. For the measurement on single particle or identical particles with the same trajectory, the standard rainbow technique (SRT) is the optical technique able to measure simultaneously size and refractive index of a droplet. Figure 2.10(a) shows an example image of standard rainbow pattern with ripple structure scattered by monodisperse water droplets at atmospheric pressure. The pioneer work employed standard rainbow technique for the measurement of refractive index and size of fuel droplets is presented by Roth et al. [24, 25]. In 2009, Saengkaew et al. [26] introduced a new standard rainbow signal processing strategy taking into account ripple structure. The new processing strategy provides a very high accuracy for the diameter measurement of 0.01 μm and the refractive index measurement of 0.0001. In addition, this technique can be applied to study the evaporation of monodispersed droplets presented by Promvongsa et al. in an international symposium by combustion institute in 2016 [27]. They followed droplets along the trajectory and obtained a diameter change as small as 10 nm for 80 μm droplet at 20°C. For the extension of SRT to the measurement of sprays, van Beeck et al., 1999 [20] introduced global rainbow technique (GRT). The global rainbow is the result of the superimposition of the rainbow patterns of an ensemble of droplets without assumption on droplets trajectories. Accordingly, the ripple structure disappears as seen in Figure 2.10(b). This technique provides the capability to measure the size distribution and the average refractive index. In the original work of van Beeck, the processing was carried out on some particular points limiting the accuracy on the refractive index and the size distribution measurements. Later, Saengkeaw, 2006 [23] introduced a new inversion strategy fitting all the integrality of the rainbow signal enabling an increase of the accuracy of the size distribution and refractive index to be 0.0001 in index.

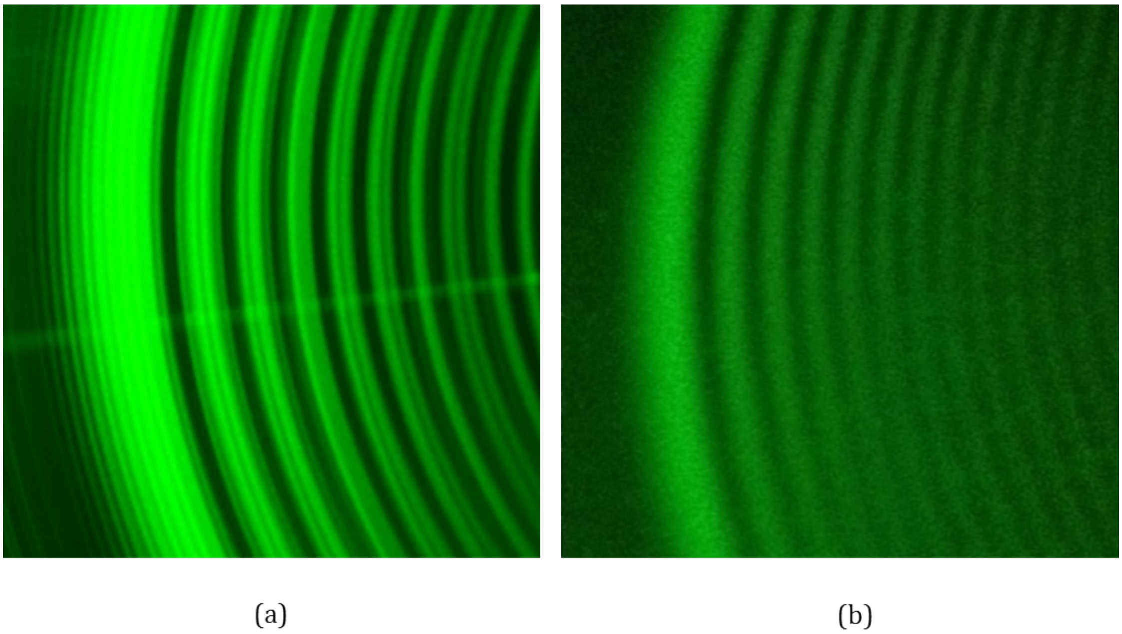

(a) (b)

Figure 2.10: Rainbow patterns observed in this study: (a) Standard rainbow pattern scattered by a line of monodisperse water droplets generated from 50 μm pinhole, (b) Global rainbow pattern scattered by nearly monodisperse droplets of water generated from 100 μm pinhole

2.4.3 Adaptation of the global rainbow technique for measurements under high-pressure

In the classical use of the rainbow technique, standard or global rainbow technique, the variation of the value of the refractive index is limited. The lens and the CCD camera are able to be used because the measurement is at a fix angle. In our case, measurement for ethane must be performed close to the critical state, P_{cr}=48.72 bar and T_{cr}=32.17°C. The refractive index of ethane at critical state is expected to be 1.069. To follow the rainbow location of ethane droplet from atmospheric pressure to near critical state, the rainbow location of ethane droplet is expected to move with a large angular variation greater than 70° . Therefore, in the first step, it has been decided not to use a camera for the detection of the rainbow pattern. The experiment will be more flexible to follow a large change of the rainbow location and only a screen will be used.

For measurements, we attempted to work on the line of monodisperse droplets. For that, there are two challenges to solve: first, to obtain as much as possible a line of droplets; second, to be able to produce and observe rainbow pattern. As the exploration of rainbow pattern is in the large range of refractive index according to the variation of pressure from atmospheric to near critical pressures, we firstly need to prove that the rainbow pattern is possible to be visualized.

In the experimental work, we firstly attempt to produce a line of monodisperse droplets with sizes ranging from 100 to 250 μm in high-pressure environments. However, a difficulty to produce a line of monodisperse droplets under high-pressure is encountered since the line of monodisperse droplets in these conditions becomes to be perturbed and the distribution of droplets is like a spray expanding with a low cone angle. Accordingly, it has been decided to apply the adapted global rainbow refractometry for the measurement of cloud droplets under high-pressure. To validate the technique, we firstly performed measurements on water droplets under high pressure up to 45 bar. Water was selected because there is reference data from literature to verify our measurement. In this work, the global rainbow measurement was simplified because it is the first time that rainbow technique for the measurement of free-falling droplets under high-pressure will be applied. So that, we observed only the positions of the bright patterns of the rainbow pattern from outside the high-pressure chamber. An example of global rainbow pattern observed in this work is presented in Figure 2.10(b). This global rainbow pattern occurs from the average rainbow position of nearly monodisperse spray of water. According to this measurement, the peak positions of supernumerary bows were estimated from the middle of the bright pattern. The peak positions can be used to determine the mean droplet size and refractive index. To do this, the peak positions of supernumerary bows were compared to those obtained from the simulations based on Debye's theory (p=2). Consequently, the mean size and the refractive index of nearly monodisperse droplets are extracted from the best-fit peak positions obtained from the rainbow signal computed from the simulation. To show an example of the fitting of our measurement, Figure 2.11 presents the peak positions of supernumerary bows obtained from the measurement on water droplets under pressure of 15.26 bar and its best-fit peak positions obtained from rainbow pattern simulations based on Debye's theory (p=2).

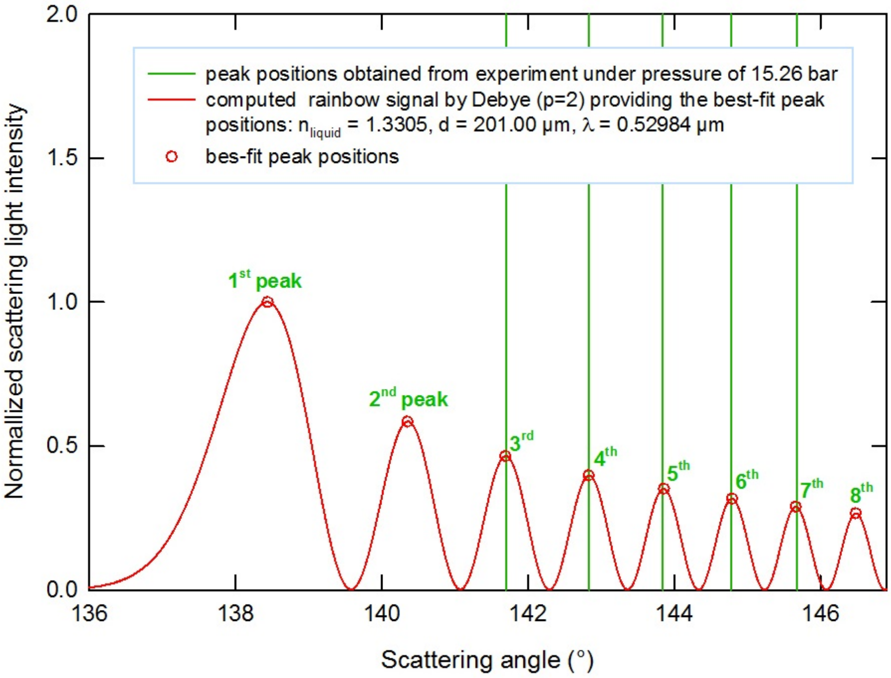

Figure 2.11: The peak positions of supernumerary bows obtained from the measurement under pressure of 15.26 bar and its best-fit peak positions obtained from rainbow pattern simulations based on Debye's theory (p=2)

2.4.4 Simulations of the rainbow pattern

2.4.4.1 Simulations of the global rainbow pattern

To have a good understanding of the global rainbow pattern, the dependences of the global rainbow pattern on the refractive index and droplet size were studied [28]. In this work, the rainbow simulation program developed by Mees and Meunier-Guttin-Cluzel at CORIA laboratory was used to simulate rainbow pattern. This simulation code is able to simulate rainbow pattern computed by Lorenz-Mie's theory as well as Debye's theory. Since we emphasized on the supernumerary bows according to the global rainbow measurement, the simulation from Debye's theory has been selected. To simulate the rainbow pattern without taken into account a ripple structure, the computation based on Debye's theory allowed us to select only the interference of the internally reflected ray (p=2). Figure 2.12 shows the comparison of the global rainbow pattern predicted by Debye (p=2) and the standard rainbow pattern predicted by Lorenz-Mie for water droplet. These rainbow patterns were computed in the same conditions with refractive index of 1.3353, droplet diameter of 160 μm and wavelength of 0.532 μm.

To show the sensitivity of the rainbow location relative to the value of the refractive index, the simulated rainbow patterns of spherical particles with three refractive indices of 1.335, 1.336 and 1.337 were compared, respectively. These three rainbow patterns were computed using the same diameter of 160 μm and a wavelength of 0.532 μm. Figure 2.13 reveals that the global rainbow patterns of water droplet have similar scattering patterns. However, the rainbow positions shift toward positions with larger angles when the refractive index is higher. For the dependence of particle size on the rainbow pattern, the global rainbow patterns were simulated for three difference sizes of 120, 160 and 200 μm with the same refractive index of 1.3353 and wavelength of 0.532 μm as shown in Figure 2.14. This figure depicts that the angular position of the first peak is closer to the geometrical rainbow location when the particle size increases. The first peak position is inversely proportional to the particle size, and the distance between supernumerary peak is larger as the diameter is smaller. An understanding of the structure of the rainbow pattern due to the refractive index and particle size provides us the capability to well interpret the rainbow pattern observed from experiments.

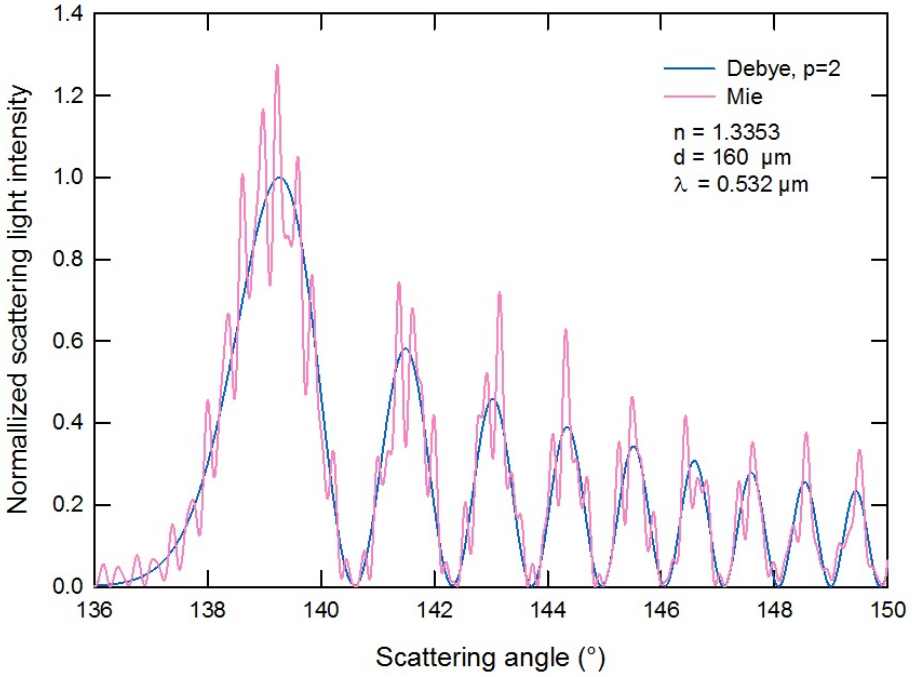

Figure 2.12: Comparison of the rainbow pattern of water droplet predicted by Debye (p=2) and the standard rainbow pattern predicted by Lorenz-Mie

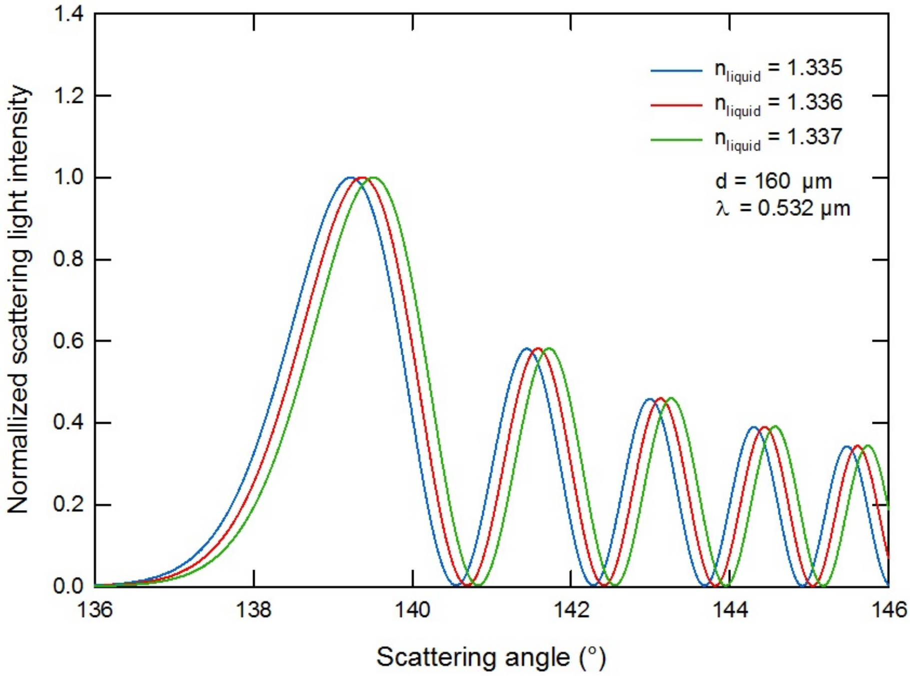

Figure 2.13: Effect of refractive index on the rainbow pattern predicted by Debye (p=2)

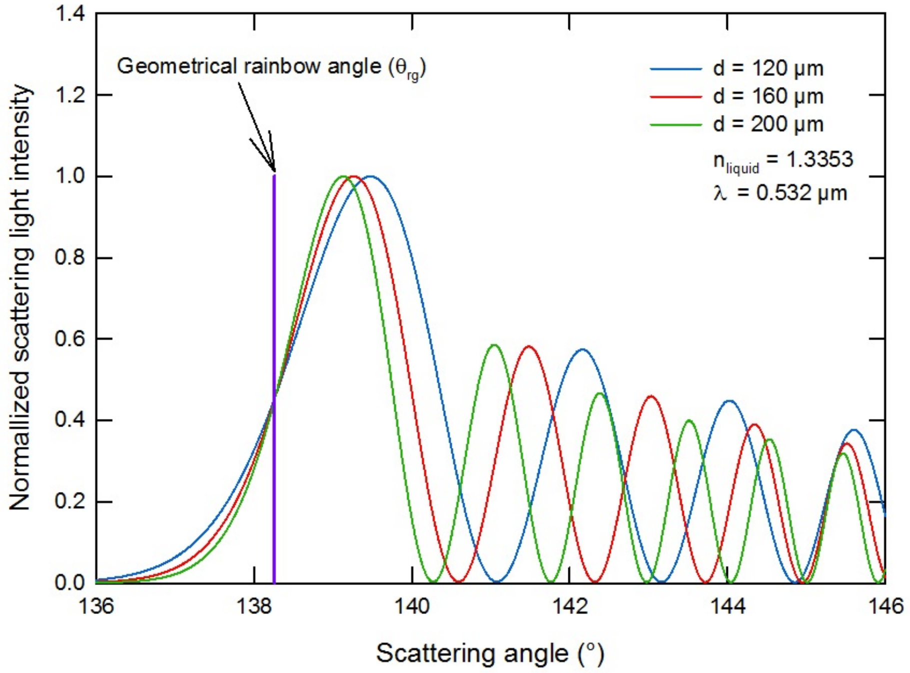

Figure 2.14: Effect of droplet size on the rainbow pattern predicted by Debye (p=2)

2.4.4.2 Rainbow signal's first peak dependence on refractive index

In this section, the rainbow pattern's first peak dependence on the refractive index was studied. Firstly, the relationship between refractive index and maximum position of rainbow pattern's first peak computed from Debye theory (p=2) for droplet of 100 μm and wavelength of 532 μm was plotted as shown in Figure 2.15. When the refractive index is closer to 1.00, the decrease of the maximum intensity position of rainbow pattern's first peak is more pronounced. It can be concluded that the change of maximum position of rainbow pattern's first peak corresponding to rainbow angle is more sensitive when the refractive index is smaller. Secondly, the relationship between refractive index and maximum intensity of rainbow pattern's first peak computed from Debye theory (p=2) for droplet of 100 μm and wavelength of 532 μm was plotted as well. An evident relationship is found as in Figure 2.16. It shows that the increase of maximum intensity of rainbow pattern's first peak is higher when the refractive index is higher. The data of maximum position and maximum intensity of rainbow pattern's first peak corresponding to refractive index is finally presented in table 2.1

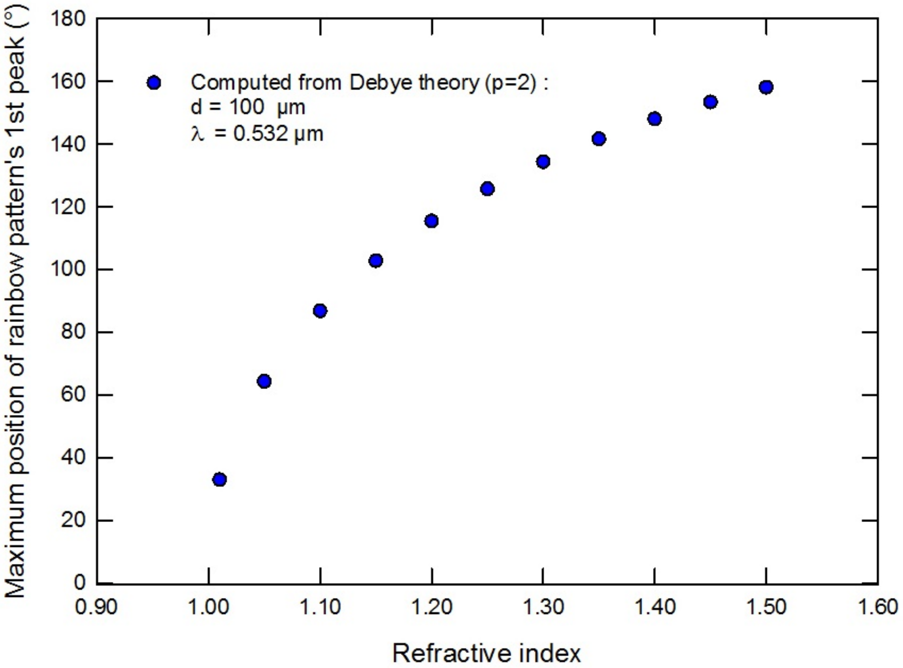

Figure 2.15: Relationship between refractive index and maximum position of rainbow pattern's first peak predicted by Debye (p=2) for droplet of 100 μm and wavelength of 532 μm

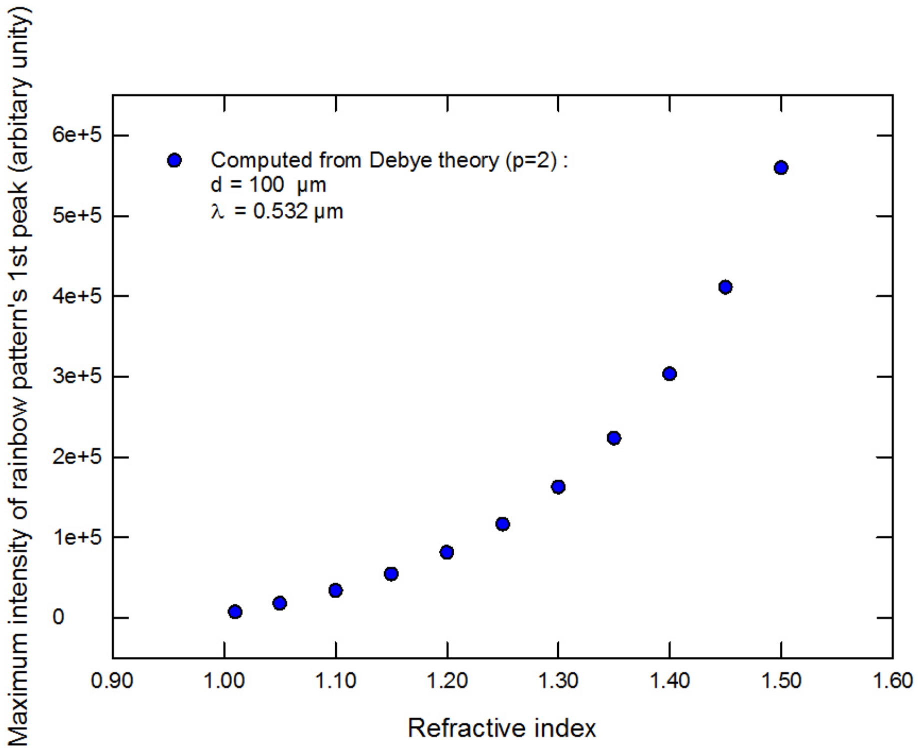

Figure 2.16: Relationship between refractive index and relation of maximum intensity of rainbow pattern's first peak predicted by Debye (p=2) for droplet of 100 μm and wavelength of 532 μm

Table 2.1: Maximum positions and maximum intensities of rainbow pattern's first peak for different refractive indices predicted by Debye (p=2, d=100 μm, λ=532 μm)

Refractive index	Maximum positions of 1^{st} peak (°)	Maximum intensities of 1^{st} peak (arbitrary unit)
1.01	32.88	7408
1.05	64.22	17973
1.10	86.78	33839
1.15	102.81	54407
1.20	115.44	81302
1.25	125.74	116477
1.30	134.33	162642
1.35	141.67	223308
1.40	148.02	303286
1.45	153.41	411207
1.50	158.11	559616

2.4.5 Pressure dependence of refractive index of water and ethanol from literature

Before performing experiments, the relationship between pressure, temperature and refractive index of water from the literature, Schiebener et al [6], was studied. The refractive index of water at different pressures and temperaturs was computed using the correlation provided by Schiebener et al. [6]. The plot of refractive index of water at different pressures and temperatures is shown in Figure 2.17 and data are presented in Table 2.2. Figure 2.17 shows that the refractive index of water is sensitive to the temperature. The decrease of refractive index is larger when the temperature is higher. With pressure, the refractive index is proportional to the pressure. The trend for larger refractive index with pressure is also observed for various temperatures. The relationship obtained from Schiebener et al. [6] will be used to verify our experiment results as a referent data.

For ethanol, the reference data of relationship between refractive index of liquid ethanol and pressure and temperature are rare. Therefore, they will be presented separately. Figure 2.18 represents the relationship between refractive index of ethanol and pressure in range of 1-14000 bar at temperature of 20 and 25 °C. This plot shows an increasing trend of refractive index due to the pressure. We obtained reference data of refractive index only for high pressure. The reference data for this plot is represented in Table 2.3. Figure 2.19 represents the relationship between refractive index of ethanol and temperature from 0 to 28 °C at atmospheric pressure. It shows that refractive index has a linearly decreasing trend due to the increase of temperature. The reference data for this plot are shown in Table 2.4

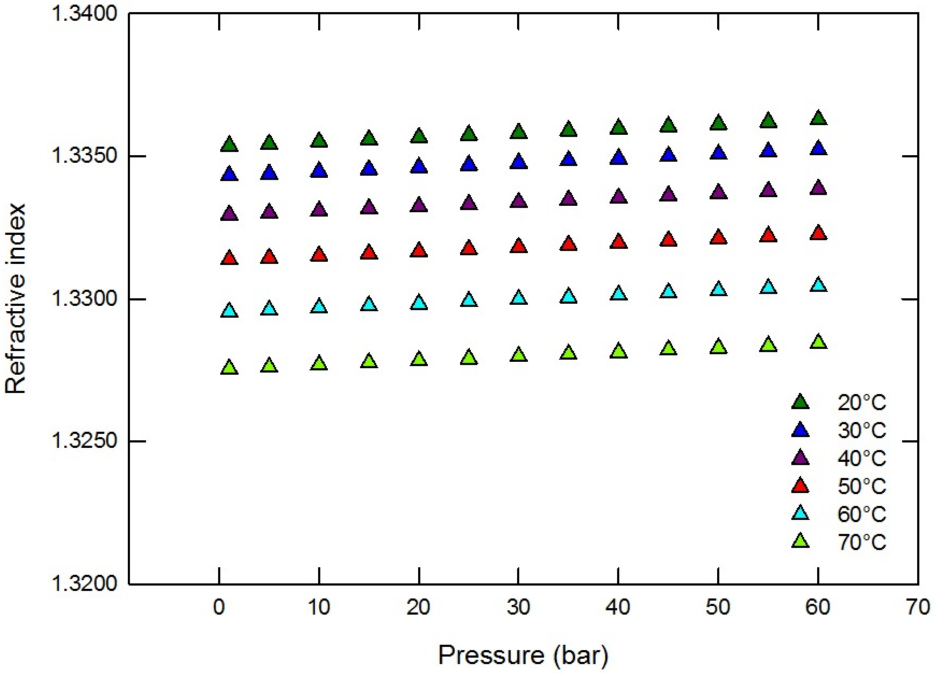

Figure 2.17: Refractive index of water at different pressures and temperatures computed from the correlation provided by Schiebener et al. [6]

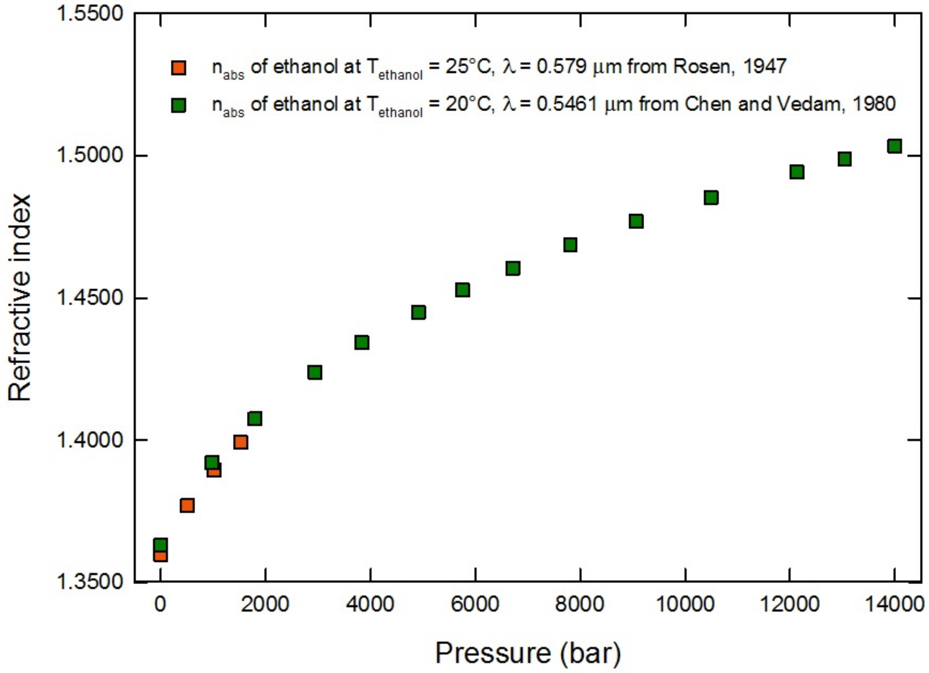

Figure 2.18: Effect of pressure on refractive index of liquid ethanol provided by Rosen [7] and Chen and Vedam [8]

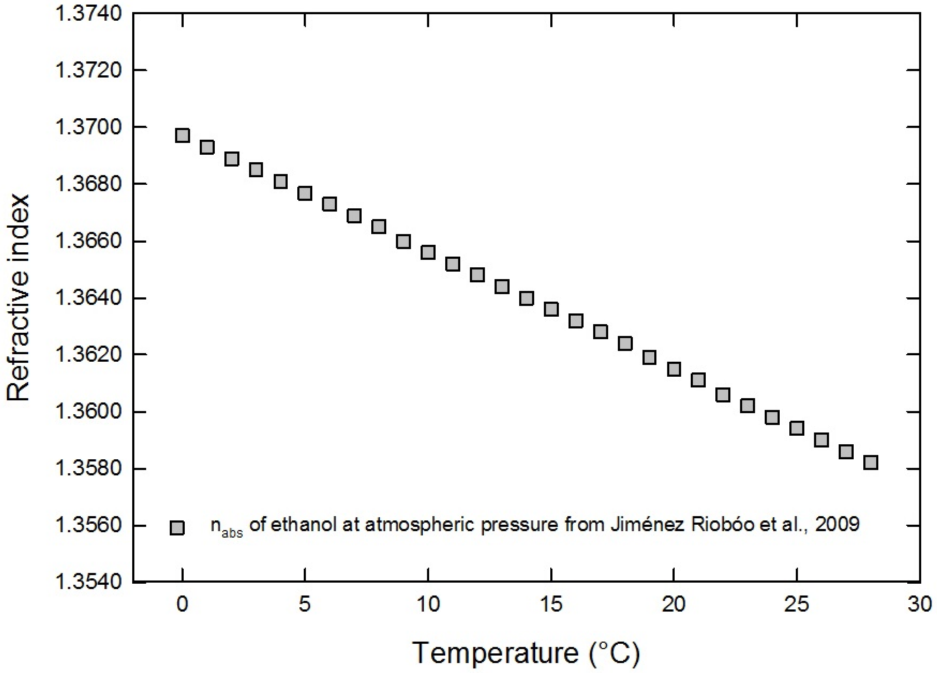

Figure 2.19: Effect of temperature on refractive index of liquid ethanol provided by Jiménez Ricobóo [9]

Table 2.2: Percentage of the estimated concentration of gaseous mixture from experiments

Pressure (bar)	Refractive index at different temperatures					
	20°C	30°C	40°C	50°C	60°C	70°C
1.0133	1.3354	1.3343	1.3329	1.3314	1.3295	1.3275
5	1.3354	1.3344	1.3330	1.3314	1.3296	1.3276
10	1.3355	1.3345	1.3331	1.3315	1.3297	1.3277
15	1.3356	1.3345	1.3332	1.3316	1.3298	1.3278
20	1.3357	1.3346	1.3332	1.3317	1.3298	1.3278
25	1.3357	1.3347	1.3333	1.3317	1.3299	1.3279
30	1.3358	1.3348	1.3334	1.3318	1.3300	1.3280
35	1.3359	1.3348	1.3335	1.3319	1.3301	1.3281
40	1.3360	1.3349	1.3335	1.3320	1.3301	1.3281
45	1.3360	1.3350	1.3336	1.3320	1.3302	1.3282
50	1.3361	1.3351	1.3337	1.3321	1.3303	1.3283
55	1.3362	1.3351	1.3338	1.3322	1.3304	1.3284
60	1.3363	1.3352	1.3338	1.3323	1.3304	1.3284

Table 2.3: Effect of pressure on refractive index of liquid ethanol

Chen and Vedam, 1980 [8]		Rosen, 1947 [7]	
Pressure (bar)	Refractive index	Pressure (bar)	Refractive index
1	1.3632	1.0133	1.3609
980	1.3919	506.6250	1.3784
1800	1.4074	1013.2500	1.3909
2940	1.4238	1519.8750	1.4005
3830	1.4342		
4910	1.4451		
5750	1.4527		
6710	1.4605		
7810	1.4685		
9060	1.4768		
10490	1.4853		
12130	1.4942		
13040	1.4987		
14000	1.5033		

Table 2.4: Data of refractive index of liquid ethanol at different temperatures from Jiménez Ricobóo, 2009 [9]

Temperature (°C)	Refractive index	Temperature (°C)	Refractive index
0	1.3697	15	1.3636
1	1.3693	16	1.3632
2	1.3689	17	1.3628
3	1.3685	18	1.3624
4	1.3681	19	1.3619
5	1.3677	20	1.3615
6	1.3673	21	1.3611
7	1.3669	22	1.3606
8	1.3665	23	1.3602
9	1.3660	24	1.3598
10	1.3656	25	1.3594
11	1.3652	26	1.3590
12	1.3648	27	1.3586
13	1.3644	28	1.3582
14	1.3640		

2.4.6 Prediction of the global rainbow of ethane droplets near critical point

To study the physical properties of ethane droplets close to the critical condition (pressure of 48.72 bar and temperature of 32.17°C), we firstly predicted the behavior of rainbow pattern in this condition. To do this, the refractive index of ethane reaching the critical condition was estimated from the reference data from George et al., 1973 [10]. The methodology used to estimate the refractive index is presented in Appendix 2. Figure 2.20 shows the predicted rainbow rays for ethane droplet near critical condition at pressure of 48.26 bar and temperatures of 28, 29, 30 and 31°C. The rainbow angle decreases due to the increase of temperature (reduction of the refractive index). This change is significant when it is approaching to critical condition compared to those of water droplet at the same thermodynamic conditions. The rainbow rays for water droplet is shown in Figure 2.21. For pressure of 48 bar and temperature in the range of 30-31°C, the variation of the rainbow angle of water droplet due to the increasing temperature by 1°C is 0.01° while it is 0.80° for ethane. The ratio of the rainbow angle change for ethane droplet is then 80 times greater than those for water droplet.

Moreover, at the atmospheric pressure and temperature of 30°C, the refractive index of water is equal to 1.3343 giving a rainbow angle of 138.11° which is very close to the rainbow angle of water at pressure of 48 bar and temperature of 30-31°C as can be seen in 2.21. The ray of light passing through water droplet at atmospheric pressure is represented as the red dotted ray. The difference of rainbow angle between the red dotted ray for water droplet at atmospheric pressure and the pink ray for water droplet at pressure of 48 bar and temperature of 30°C is 0.10°. For liquid ethane at atmospheric pressure, ethane is in liquid phase when the temperature is less than its boiling point of -88.5°C. However, the refractive index of liquid ethane in literature is very rare. Bodoz et al., 1992 [29], provided the refractive index of liquid ethane of 1.3887 at pressure of 1.5 bar, temperature of -182.15°C (94K) and wavelength of 0.670 μm. The refractive index of ethane from Bodoz et al. was used to estimate the rainbow angle of liquid ethane near the atmospheric pressure. In Figure 2.20, the red dotted ray represents the ray of light passing through ethane droplet at pressure of 1.5 bar and temperature of -182.15°C with the rainbow angle of 145.4°. Accordingly, it is possible to estimate the moving of rainbow location of ethane droplet at atmospheric pressure to the critical conditions. It is expected that the rainbow location will move around 70°. This estimation shows that the difference between the experiment for water and ethane under pressure of 1-48 bar will be significant. As the rainbow location almost does not change for the case of water therefore it would be possible to use a camera for measurements. However, in the first step we did not fix a camera. If the camera was initially fixed, it would be necessary to calibrate the camera many times as we aimed to study in the large range of angle.

Furthermore, the global rainbow patterns approaching to the critical condition were also predicted by the simulations based on Debye (p=2) and they are presented in Figure 2.22. The rainbow position moves to the direction that decreases angular position when it is closer to critical condition. Finally, we are able to predict the behavior of rainbow pattern observed near the critical condition. The optical setup for the measurement in this condition was then designed.

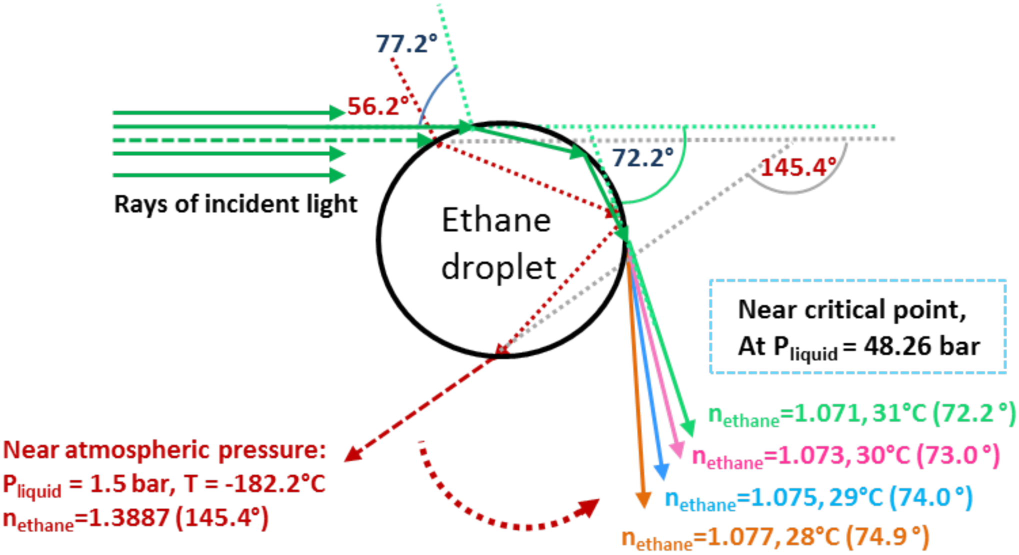

Figure 2.20: Predicted rainbow rays of ethane droplet under thermodynamic conditions approaching to the critical point at pressure of 48.26 bar and temperatures of 28, 29, 30 and 31°C, respectively.

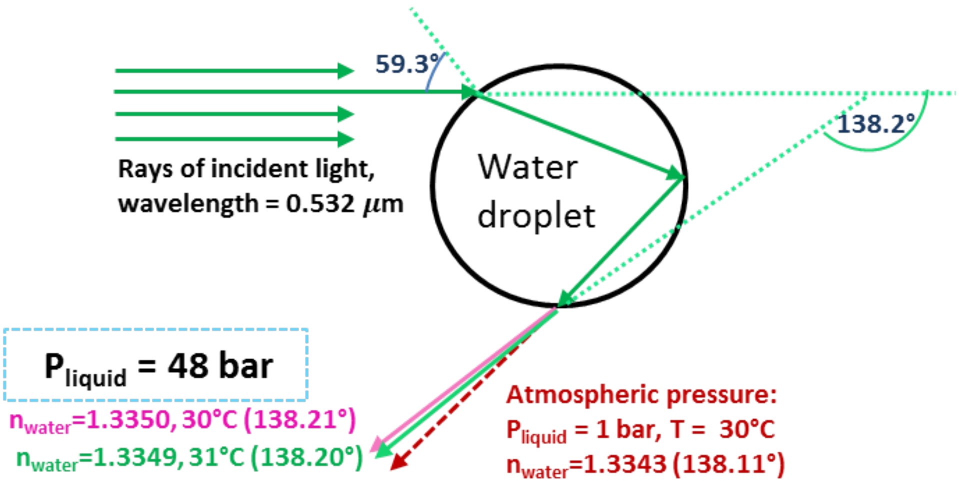

Figure 2.21: Predicted rainbow rays of water droplet at pressure of 48 bar and temperatures of 30 and 31°C, respectively.

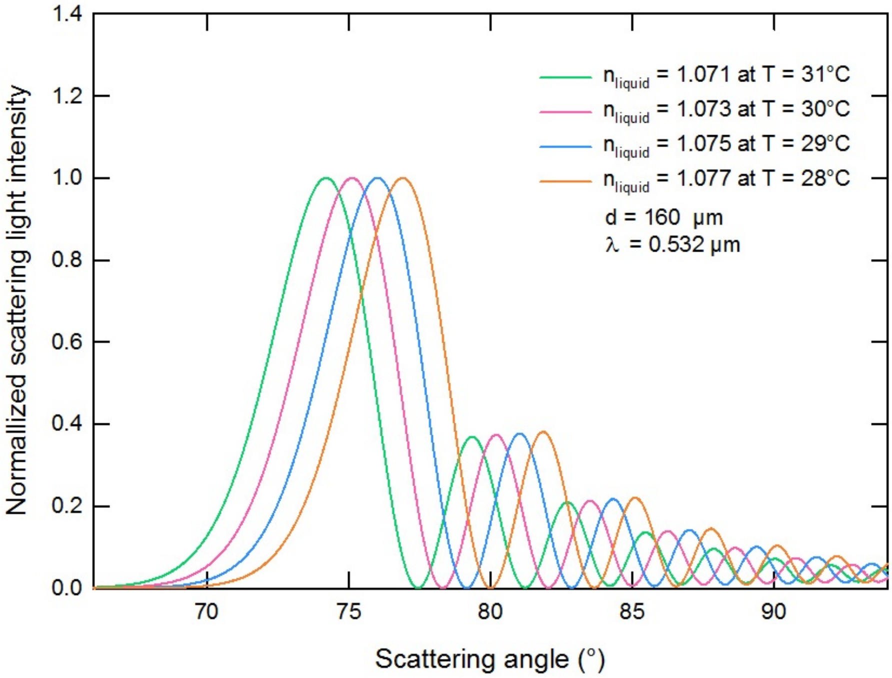

Figure 2.22: Predicted rainbow pattern of ethane droplet by Debye (p=2) when the thermodynamic condition is approaching to the critical state

CHAPTER 3

Validation of refractive index measurements on free-falling water and ethanol droplets under high pressure conditions

3.1 Introduction

The aim of this work is to characterize the physical properties of free-falling droplets close to the critical point. For that, global rainbow refractometry technique was selected to measure droplet-size and refractive index of moving droplets. This is the first time that global rainbow refractometry technique is developed and adapted for refractive index measurements of moving droplets in high pressure conditions up to 45 bar. Therefore, the validation of this technique will be carried out firstly. Water and ethanol were selected for this experiment as the reference data from literature for refractive index measurements in cells filled with liquid under high pressure environments are available. This chapter provides a validation of the refractive index measurements on free-falling water and ethanol droplets by using an adapted global rainbow refractometry technique.

3.2 Experimental setup and methodology

This section describes the experimental equipment, experimental setup, the procedure to control the setup during experiment and the optical measurement method.

3.2.1 High-pressure optical test chamber and measurement connections

An optical high-pressure test chamber was designed to produce the conditions of evaporation of fuel droplets in extreme thermodynamic conditions. For that, a monodisperse droplet injector was inserted inside an optical high-pressure chamber in which the pressure of air can be monitored up to 50 bar. The passage from sub- to supercritical conditions can be controlled by changing the temperature of the gas from room temperature up to 35°C. The main housing chamber is made of a single block of highly resistant steel and has UV-transparent quartz windows (fused silica glass) for optical accessibility. There are two 40-mm-wide and 150-mm-high glass windows with a thickness of 20 mm installed opposite to each other. The others sides are two 20-mm-wide and 150-mm-high glass windows with a thickness of 20 mm. At the bottom part of the test chamber, a pyramid space is used to store fuel liquid during the experiment. This one is connected to the draining component used to drain liquid after the experiment. A picture and the schematic diagram of the high-pressure chamber are shown in Figure 3.1. For the control and the tuning of temperature inside the chamber, eight vertical heat cartridges were mounted at each corner of the main housing. One of K-type thermocouples was installed into the test chamber wall to monitor the steel temperature (T_{wall}) for the temperature control of the chamber walls. To measure air temperature inside chamber ($T_{air,inside}$) at different positions, three thermocouples were installed inside the test chamber as shown in Figure 3.2. For the control of pressure, the air pressure (P_{air}) and liquid pressure (P_{liquid}) were measured by pressure transducer. The difference between air pressure and liquid pressure (ΔP) was then computed. The pressure transducer was installed on the liquid supply system for the measurement of liquid pressure and connected to the test chamber by an air pipeline for the measurement of pressure of air inside the chamber as seen in Figure 3.3. Both temperature and pressure were monitored continuously during experiments. All electronics connections between the PC computer, pressure controller and temperature controller were designed for a remote control. Therefore, the heating system, temperature measurement, pressure measurement, syringe pump, flowmeters can be remote controlled by a PC computer.

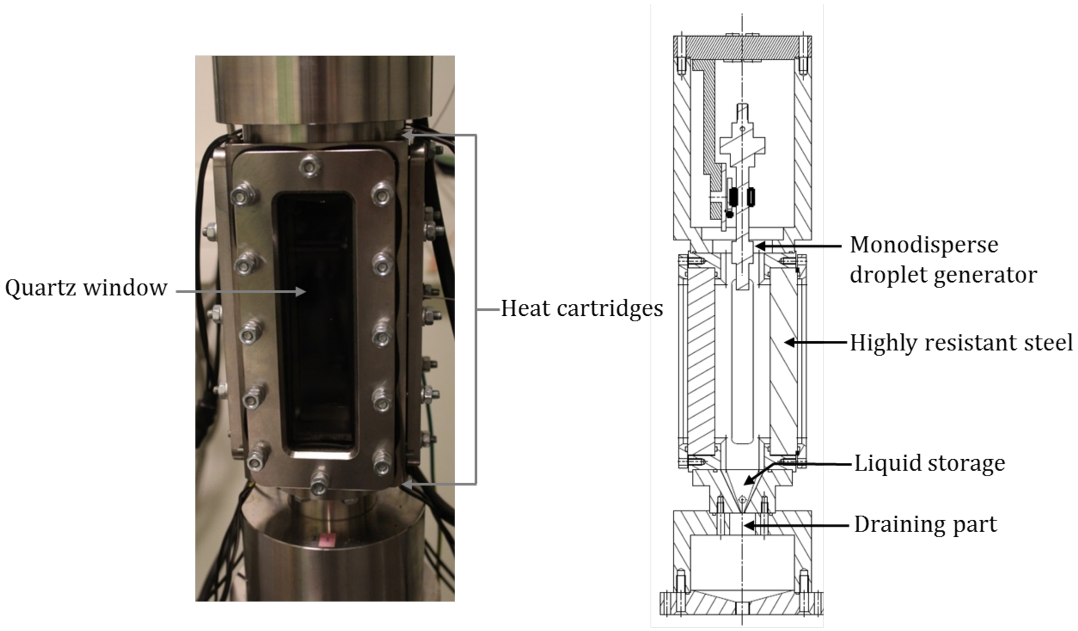

(a) (b)

Figure 3.1: High-pressure chamber: (a) front view image of the main housing and (b) design of the high-pressure test chamber

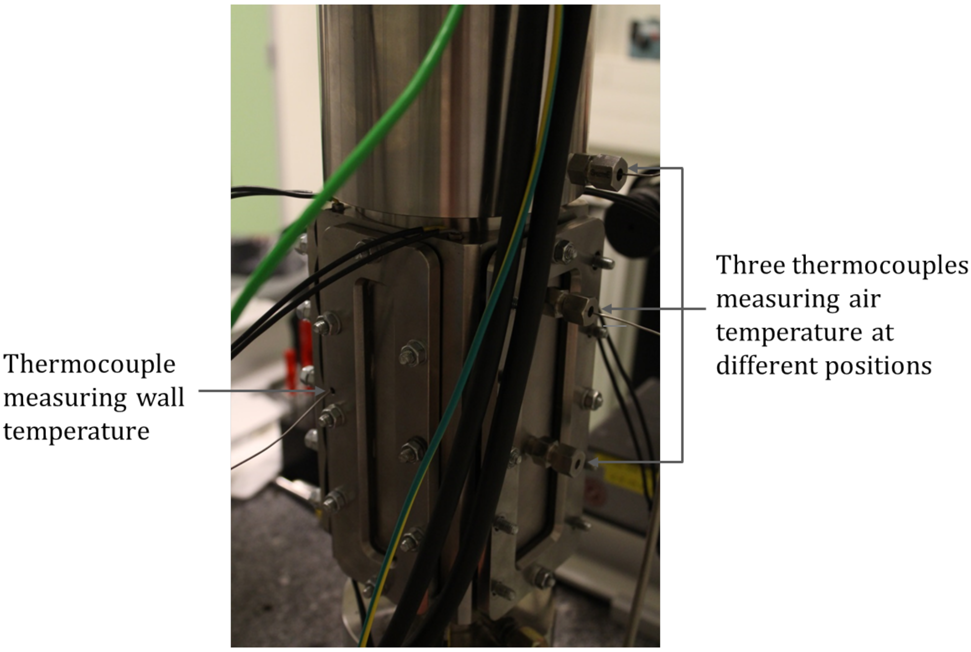

Figure 3.2: K-type thermocouples inserted into the chamber wall and inside the chamber

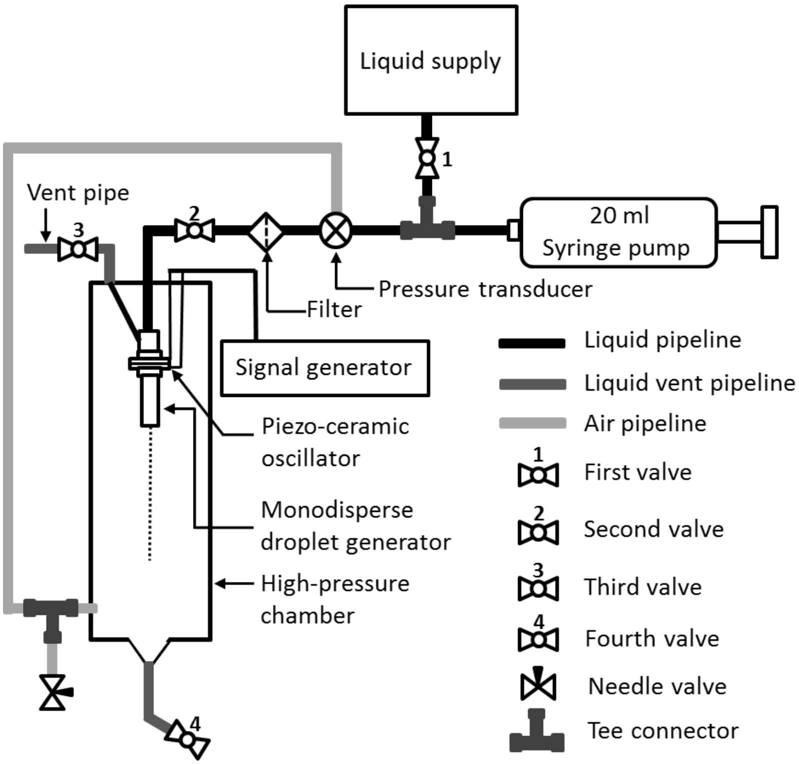

Figure 3.3: Schematic diagram of the liquid injection supply

3.2.2 Liquid supply system

The liquid supply system is an essential component for liquid droplet injection. The schematic diagram of this system is shown in Figure 3.3. For the connection, liquid supply pipelines (6-mm diameter) were used to connect together the syringe pump, liquid supply and monodisperse droplet generator. The syringe pump was used to pump liquid from the liquid supply and then feed the injector with liquid with a good control. The 20 ml stainless steel syringe (19-mm diameter) was specifically selected to perform experiments under high-pressure conditions (pressure up to 50 bar). For the control of the liquid system, four ball valves were mounted to the system. The control of liquid in liquid supply system is described as follows:

Filling the liquid supply system: the first valve mounted between the liquid supply and the syringe pump was used to provide liquid inside all the liquid supply. In this process, only the first valve was opened and the liquid was filled into the syringe pump.

Filling the liquid injection system: the second valve was used to inject liquid contained in the syringe pump into the high-pressure test chamber. During the feeding of liquid into the injection system, the first valve was closed. After draining the tank of the syringe pump, the second valve was closed and then the first valve was opened to refill the tank of the syringe again. These steps were repeated several times to fully fill the liquid supply of the injector. However, air bubbles still left inside the circuit.

Suppression of air bubble: To eliminate air bubbles inside the liquid supply, a third valve was used. This valve was installed in vent pipe outside the test chamber (6-mm diameter) and connected to vent pipe inside the test chamber (4-mm diameter) and injector. To drain air bubbles from liquid supply system, the second and third valves were opened and the first valve was closed while the liquid was injected from the syringe pump. In this step, liquid and air bubbles escape through vent pipeline to outside. Once the emerging liquid was free of air bubbles, the third valve is closed. According to this process, it is assumed that liquid will be injected from the micro-hole as a fine jet with a constant direction.

Draining of the used liquid: the used liquid was stored with the pyramid shape located at the bottom part of the chamber. The liquid storage was connected to a fourth valve used to evacuate liquid from the test chamber. Therefore, used liquid from the preparing steps (Step 1-3) was drained before starting the experiments in high pressure conditions.

Control of liquid during experiment: to perform experiments in high-pressure conditions, only the second valve was opened to inject liquid droplets into the high-pressure test chamber. Once liquid in syringe pump was done during experiments, it was able to refill the system with liquid under high-pressure conditions.

Refilling of liquid during experiment: to refill liquid under high pressure condition, the second valve is firstly closed to prevent air under high-pressure flow out from the chamber and then the first valve was opened for refilling the liquid supply with liquid. After that, the first valve was closed and the second valve was opened again to perform experiment. Due to the limitation of the volume of the pump syringe (20 ml), the liquid reservoir was refilled several times during the experiments. Although the process was complex, this one works without any problem during experiments in high-pressure conditions.

Draining liquid from the test chamber: after the experiment was finished, the liquid was drained by using the fourth valve located outside the test chamber.

3.2.3 Generation of monodisperse droplets

Liquid injection is an essential process to generate line of monodisperse droplets that have spherical shapes and stable falling rates. For generating monodisperse droplets, the generator frequency (f_G) and the volume flow rate ($\dot{V}$) are the main parameters. These parameters were controlled by the voltage signal produced by a pulse generator and a syringe pump, respectively. In order to excite the piezo-ceramic oscillation module, the generator supplied a voltage amplitude of 15 volts. Figure 3.4 shows image of the signal generator and control buttons. A voltage generator was connected to the piezo-ceramic vibrating element of the injector as seen in Figure 3.3. The syringe pump (Nexus 6000 high-pressure precision syringe pump) was connected to the droplet generator by using the liquid pipeline supply. The liquid supply system associated with the syringe pump is shown in Figure 3.5. The syringe pump is able to control the liquid supply with a large dynamic range of flow rates under high-pressure. The characteristic of syringe are a diameter of 55 and 19 mm at about 9.5 bar and 76 bar, respectively [30]. Therefore, we selected the syringe with a diameter of 19 mm (20 ml syringe) to be able to perform experiments at 46 bar with a good accuracy. In this work, the volume flow rate ranges between 0.5 and 5 ml/min. Inside the injector, the nozzle plate with 100 μm of pinhole diameter (D) was inserted to produce monodisperse droplets.

In the monodisperse droplets generating part, the conditions to produce monodisperse droplets at atmospheric pressure were determined based on the Rayleigh breakup of laminar fluid jets: a jet decays into droplet as stable criteria when the wavelength of deformation on the jet surface is larger than the circumference of the jet [31]. Based on theoretical basic calculations in Appendix A, the excitation frequency (f_G) corresponding to different volume flow rates ($\dot{V}$) to produce monodisperse droplets for pinhole diameter (D) of 100 μm are presented in Table 3.1. For experiments at atmospheric pressure, the volume flow rate was firstly set by using syringe pump and then the vibration frequency was adjusted by the signal generator. The adjustment can be done by observing the rainbow signal as a signal of spherical monodisperse droplets producing stable ripple structures. These criteria will not be happen when size of droplets are not monodisperse or the shape is not spherical or both. Therefore, the frequency will be adjusted until the rainbow signal respects the criteria. Figure 3.6 shows an example of an image of stable rainbow signal with a detailed ripple structure. From an experiment point of view, the excitation frequency and the volume flow rate required to produce stable rainbow optical signals and ripple structures corresponds with the values from theoretical calculations. Accordingly, the volume flow rate and the range of corresponding frequencies from Table 3.1 will be used to generate reproducible monodispersed droplets during experiments. For example, for a pinhole size of 100 μm and a volume flow rate of 2.2 ml/min, the excitation frequency within the range of 4.460-13.379 kHz is required to generate monodispersed droplets. Accordingly, the expected droplet diameter (d) produced from a 100 μm pinhole will be between 173.65 and 250.44 μm.

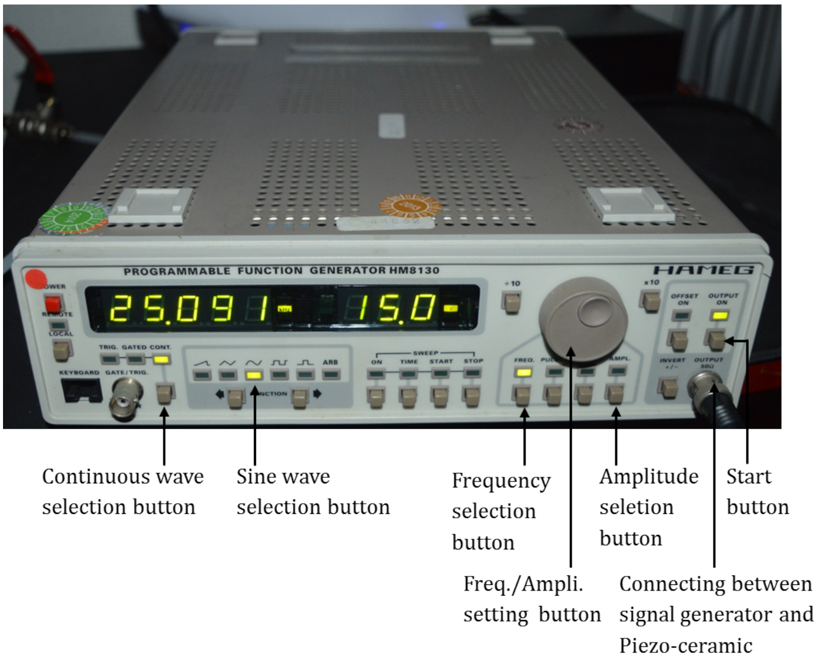

Figure 3.4: Image of signal generator and control buttons

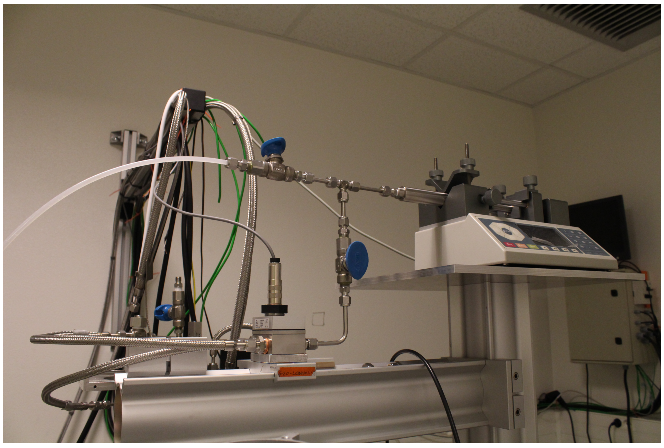

Figure 3.5: Image of syringe pump and liquid supply system

Table 3.1: Range of excited frequency relating to the volume flow rates for producing monodisperse droplets with a 100 μm pinhole at the atmospheric pressure.

D (μm)	A (cm^2)	$\dot{V}$ (ml/min)	$u_D = \dot{V}/A$ (cm/min)	Range of f_G (kHz)	Range of d (μm)
100	0.0000785	1.2	15279	$2.432 \leq f_G \leq 7.295$	$250.44 \geq d \geq 173.65$
100	0.0000785	1.4	17825	$2.837 \leq f_G \leq 8.511$	$250.44 \geq d \geq 173.65$
100	0.0000785	1.6	20372	$3.242 \leq f_G \leq 9.727$	$250.44 \geq d \geq 173.65$
100	0.0000785	1.8	22918	$3.648 \leq f_G \leq 10.943$	$250.44 \geq d \geq 173.65$
100	0.0000785	2.0	25465	$4.053 \leq f_G \leq 12.159$	$250.44 \geq d \geq 173.65$
100	0.0000785	2.2	28011	$4.458 \leq f_G \leq 13.374$	$250.44 \geq d \geq 173.65$

*Note: A = the cross section area of pinhole and u_D = jet velocity

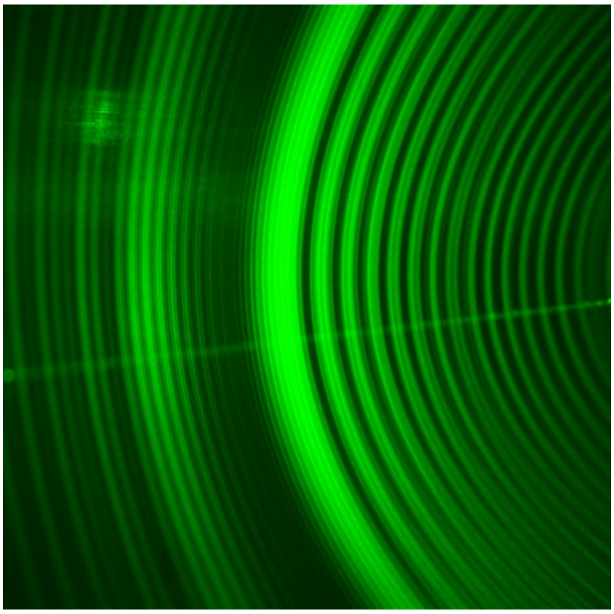

Figure 3.6: Rainbow signal generated from a 50 μm pinhole by setting a frequency of 25.091 kHz frequency and 0.6 ml/min of volume flow rate at the atmospheric pressure

3.2.4 Pressure control

This section shows the procedure of the control of pressure inside the test chamber. In this study, synthetic air was utilized to pressurize the test chamber. The connection of the pressurization system and liquid supply system is shown in Figure 3.7. For the first step of the pressurization procedure, pressure regulator was used to set the maximum input pressure. Then, the valve of the compressed air bottle was opened. This step allowed the air with the set pressure flow into a pipe between the pressure regulator and flowmeter. After that, the input air flow rate used to pressurize air inside the test chamber was controlled by a flowmeter regulated from a PC computer. The minimum and maximum flow rates which are possible to pressurize air in chamber are 0.005 and 0.500 g/s, respectively. For an experiment under high pressure, the pressure increased with flow rate in the range of 0.025-0.100 g/s. After ending experiments under high pressure, air inside the test chamber was vented to decrease pressure by using a needle valve. Moreover, it was able to use the needle valve for gradually decreasing pressure during the experiments for a fine adjustment of pressure as well.

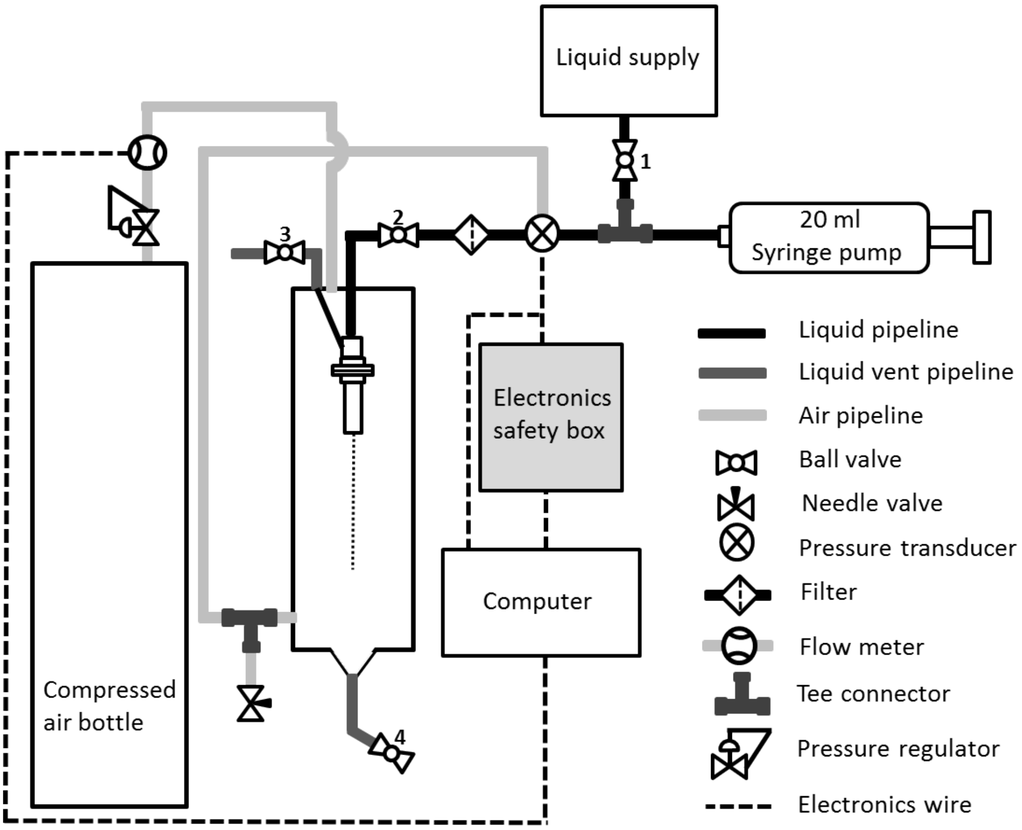

Figure 3.7: Schematic diagram of the air pressurization system with the associated connection to the liquid injection system

3.2.5 Temperature control

The test chamber is heated with eight vertical heat cartridges inserted into the walls. A PID temperature control is applied. The temperature of chamber wall (T_{wall}) is controlled by means of a K thermocouple placed inside the wall. The chamber was firstly heated with the maximum power and the wall temperature increased rapidly. Later, heating gradually controlled around 1-5 percent of the power to reach the selected temperature setpoint. However, the objective of the experiments is to control air temperature inside the chamber ($T_{air,inside}$). Therefore, the wall temperature setpoint is the value able to heat air to the expected air temperature. For example, the chamber wall temperature was heated at approximately 60-70°C in order to obtain air temperature around 50°C. Figure 3.8 shows the thermocouple locations to measure air temperatures inside chamber, air temperature outside chamber and the chamber wall temperature. The temperature of air at the position close to the exit of the injector ($T_{air2,inside}$) was used to obtain the initial air temperature in which droplets are injected. Complementary measurement of temperature of air was performed close to the rainbow measurement location via third K thermocouple ($T_{air3,inside}$). The temperature of air outside chamber ($T_{air,outside}$) completes the series of temperature used to well control the experiment. Temperature values are read out via a INT data acquisition board to a Labview routine.

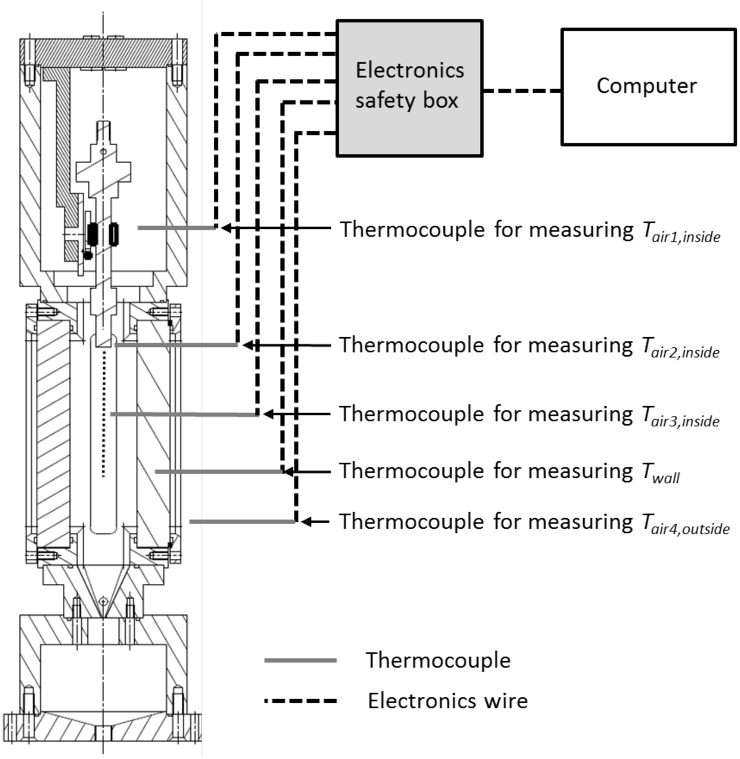

Figure 3.8: The schematic diagram of temperature measurement

3.2.6 The optical measurement of rainbow signal

This section provides the procedure of the rainbow optical measurements. The first step to obtain accurate optical measurements was to define the rainbow angle of liquid droplets. From this information, the position of the laser source as well as the screen for the rainbow observation could be defined. Accordingly, the refractive indices of liquids from literature were used to estimate values of rainbow angles. In this study, liquid water and ethanol were firstly selected in order to validate the rainbow technique. After knowing the estimated rainbow angles of these liquids, the experimental setup was designed. The rainbow angles of water and ethanol droplets are around 138° and 142°, respectively. Figure 3.9 shows the top-view schematic diagram of the light paths during experiments. The light is emitted from a 0.532 μm 200 mW green laser source. It passes through an optical window to enter into the test chamber and then it is oriented through the liquid droplet. The scattered light comes back outside the test chamber and is visualized on a screen. However, interferences with another reflection of light can disturb the analysis of the rainbow signal (see the green dotted lines as illustrated in Figure 3.9.)

The first reflection is formed when light travels to the external surface of window and then it is reflected back to the screen. The second reflection is caused by the internal surface of the optical window. The 0.6328 μm 5 mW helium-neon laser generates perpendicular lines of light on a surface of an the optical window. This He-Ne laser and its incident point were used to give reference points for the measurement of the distance between the external surface of the optical window and the screen (y_3).

In addition, Figure 3.9 presents important variables used to calculate the scattering angle and refractive index of liquid droplets. The description of the variables are as follows:

y_1, distance in the y direction from droplets to the internal surface of the optical window

y_2, thickness of the optical window

y_3, distance in the y direction from the external surface of the optical window to the screen

y, distance in the y direction from the droplets to the screen

x_b, distance in the x direction from the point of incidence of 0.532 μm laser at the external surface of the optical window to the position of incident light at the internal surface of the optical window

x_c, distance in the x direction from the position of incident light at the internal surface of the optical window to droplets

x_1, distance in the x direction from droplets to the position of scattered light at the internal surface of the optical window

x_2, distance in the x direction from the position of scattered light a the internal surface of the optical window to the position of scattered light at the external surface of the optical window

x_3, distance in the x direction from the position of scattered light at the external surface of at optical window to the rainbow signal position

x_{n1}, distance in the x direction from the point of incidence of 0.532 μm laser

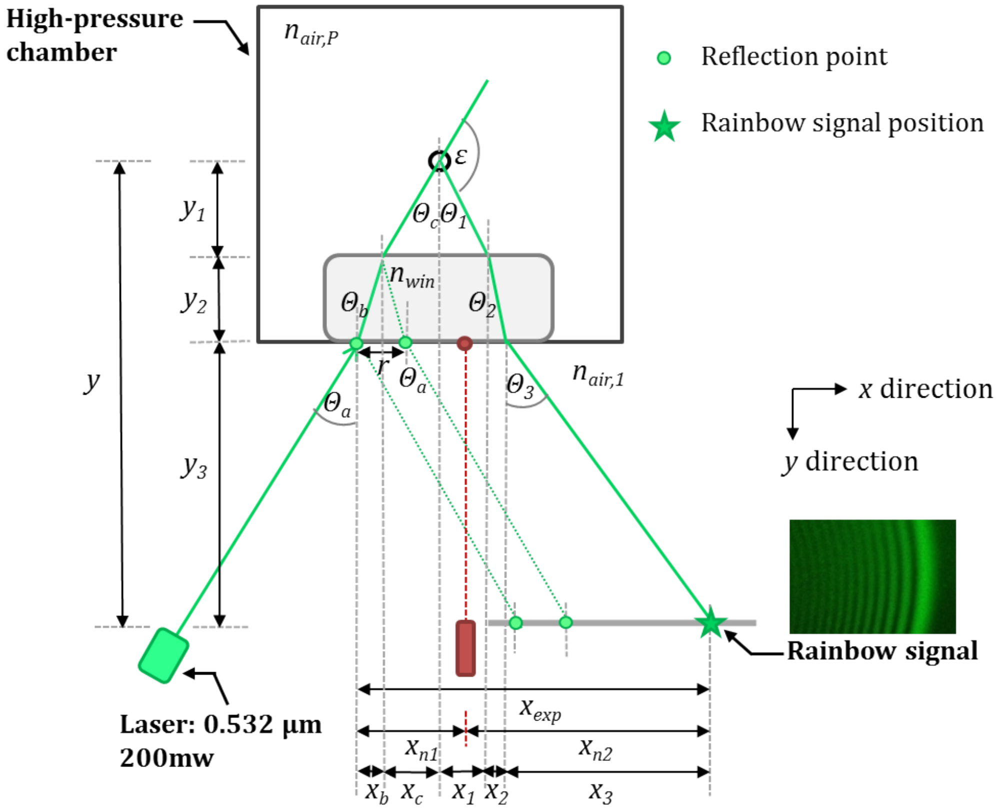

Figure 3.9: Top-view of the schematic diagram of different paths of light when the laser beam is introduced into the test chamber

at the external surface of the optical window to the point of incidence of 0.6328 μm He-Ne laser at the external surface of the optical window

x_{n2}, distance in the x direction from He-Ne laser beam to rainbow signal position

x_{exp}, distance in the x direction from the point of incidence of 0.532 μm laser at the external surface of the optical window to rainbow signal position

r, distance between the point of incidence of 0.532 μm laser at the external surface of the optical window and the first reflection point at the external surface of the optical window

$n_{air,P}$, refractive index of air in the test chamber related to the pressure in the chamber

n_{win}, refractive index of the optical window

$n_{air,1}$, refractive index of air at atmospheric pressure

θ_a, incident angle of incident light to the external surface normal of the optical window

θ_b, refraction angle of the propagating light in optical window

θ_c, refraction angle of the propagating light in high-pressure test chamber

θ_1, incident angle of scattered light to the internal surface normal of the optical window

θ_2, refraction angle of the propagating light in optical window

θ_3, refraction angle of the propagating light outside chamber
ε, scattered angle of droplet around rainbow angle.

After designing the experimental setup, experiments were carried out under various pressure from 1 to 45 bar according to the following step:
1. Start measurements at atmospheric pressure of 1.01325 bar.
2. Generate line of droplets by using a volume flow rate ($\dot{V}$) which was calculated based on the theory presented in Appendix A for a pinhole size of 100 μm. Figure 3.10 shows line of droplets produced in the experiment at atmospheric pressure.
3. Adjust the volume flow rate and the excitation frequency to produce stable spherical monodisperse droplets; selected values are those that produce stable and reproducible rainbow signal with ripple structure. For this adjustment, the volume flow rate and the excitation frequency were based on values defined in Table A.2
4. Record the rainbow signal
5. Record the selected excitation frequency and volume flow rate that produce rainbow signal in step 4.
6. Record reflection points and positions of the incidence light from He-Ne laser
7. Record the temperatures of air inside the test chamber at three different positions; $T_{air1,inside}$, $T_{air2,inside}$ and $\mathrm{T}_{air3,inside}$
8. Record the temperature of air outside the test chamber ($T_{air,outside}$)
9. Record pressure of air inside the test chamber (P_{air}), pressure of liquid (P_{liquid}) and pressure difference between liquid and air (ΔP).
10. For experiments in high pressure, the air inside chamber was pressurized to the expected value. In this work, pressure of 10-45 bar were selected.
11. Generate line of droplets by using volume flow rate and corresponding frequency based on values from Table A.2.
12. Both volume flow rate and excitation frequency were adjusted to produce the better stable rainbow signal.
13. Repeat step 4 to 8.
14. Measure y_1, y_2, y_3, x_{n1} and r.

To data process measurements, the determination of the bright pattern positions of the rainbow signal is firstly done. Figure 3.11(a) shows the rainbow signal recorded from experiments and the fixed-number. The fixed-number represents the order of peak and the edge position. The unit number represents the order of bright pattern. The decimal value indicates the edge position of bright pattern; i.e., .1 = right edge and .2 = left edge. For example, number 1.1 means the right edge of the first bright pattern and 2.2 means the left edge of the second bright pattern. After that, distances from the He-Ne laser beam to the fixed-numbers (x_{n2}) were measured; therefore, the distance between the point of incidence of 0.532 μm green laser at the external surface of the optical window and the fixed-numbers were calculated from $x_{exp}=x_{n1}+x_{n2}$. After knowing the distance x_{exp} for each fixed-numbers, the middle position between the position m.1 and m.2, where m is the order of bright pattern (i.e. 1^{st}, 2^{nd}, 3^{rd}, 4^{th}, etc.) was assumed to be the maximum intensity position of bright pattern ($\mathrm{x}_{exp,m^{th}}$). The maximum intensity positions of bright patterns are represented in Figure 3.11(b). Knowing distance $x_{exp,m^{th}}$, y_2, y_3, r, refractive index of air in the test chamber ($n_{air,P}$), refractive index of the optical window (n_{win}) and refractive index of air at atmospheric pressure ($n_{air,1}$), the scattering angle of each maximum intensity position of bright pattern ($\varepsilon_{exp,m^{th}}$) can be then calculated. The calculation of refractive index and the scattering angle of each maximum intensity position of bright pattern are provided in Section 3.3. Note that the uncertainties of the measurements of distance $x_{exp,m^{th}}$, y and r are ±0.5 mm, ±0.5 mm and ±0.2 mm, respectively. These values provide the uncertainties of refractive index measurements of ±0.0002 and ±0.0001 and ±0.002 respectively.

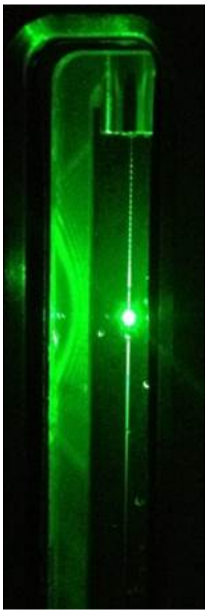

Figure 3.10: Image of a line of monodisperse droplets generated at atmospheric pressure

3.3 Calculation of scattering angle

This section describes the geometrical calculation of scattering angles of the maximum intensity positions obtained from Section 3.2.6 as well as the calculation of other important parameters which are the refractive index of air and the refractive index of the optical window. Knowing the scattering angle of rainbow signal leads to the determination of the absolute refractive index of droplet and its size which will be presented in Section 3.4.

3.3.1 Refractive index of air ($n_{air,1}$, $n_{air,P}$)

Refractive index of air is one of the key parameters used to calculate scattering angle. Furthermore, it depends on wavelength, temperature and pressure. During the experiment, scattered light was observed under different thermodynamic conditions. Therefore, refractive index of air was computed from the experimental conditions.

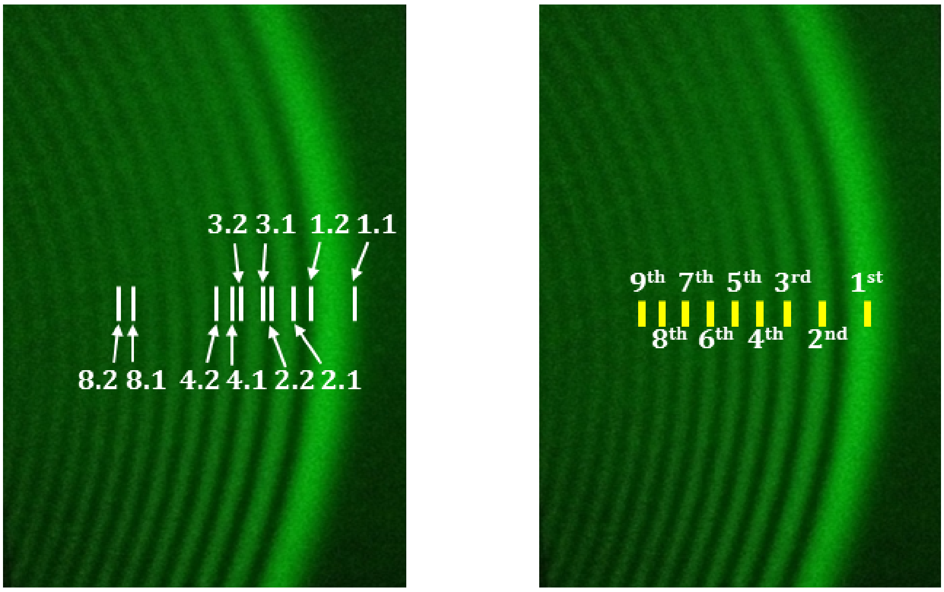

(a)

(b)

Figure 3.11: Measurement of bright pattern positions

In this study, refractive index of air is calculated by using Edlén correlation (Edlén, 1966 [32]):

$$(n_{air,P} - 1)_{tp} = \frac{P_{AIR}(n_{air,1} - 1)_s}{96095.4} \times \frac{[1 + P_{AIR}(61.3 - T_{air,inside}) \times 10^{-10}]}{(1 + 0.003661 T_{air,inside})}. \tag{3.1}$$

where $n_{air,P}$ is the refractive index of air in test chamber at $T_{air,inside}$ (°C) and pressure P_{AIR} in Pa and $(n_{air,1} - 1)_s$ is given by:

$$(n_{air,1} - 1)_s \times 10^{-8} = 8342.13 + \frac{2406030}{(130 - \sigma^2)} + \frac{15997}{(38.9 - \sigma^2)}. \tag{3.2}$$

$\sigma = 1/\lambda_{vac}$ where λ_{vac} is the wavelength of the radiation in vacuum in μm. Equations 3.1 and 3.2 were used to calculate refractive index of air inside the test chamber depending on pressure in experiment $(n_{air,P})$ and refractive index of air outside the test chamber at atmospheric pressure $(n_{air,1})$, respectively. Table 3.2 shows refractive index of air at various pressures calculated from Equation 3.1. The relationship between refractive index of air and pressure is presented in Figure 3.12. From Table 3.2, refractive index of air outside the test chamber $(n_{air,1})$ at temperature of 20°C is 1.00027. Refractive index of air inside the test chamber $n_{air,P}$ was calculated by using the pressure recorded during the experiment.

Table 3.2: Refractive index of air with pressure

Pressure (P_{AIR}) (Pa)	Pressure (P_{air}) (bar)	T_{air} (°C)	refractive index of air ($n_{air,P}$)
100000	1	20	1.00027
101325	1.01325	20	1.00027
500000	5	20	1.00135
1000000	10	20	1.00271
1500000	15	20	1.00407
2000000	20	20	1.00544
2500000	25	20	1.00681
3000000	30	20	1.00819
3500000	35	20	1.00958
4000000	40	20	1.01097
4500000	45	20	1.01236
5000000	50	20	1.01377

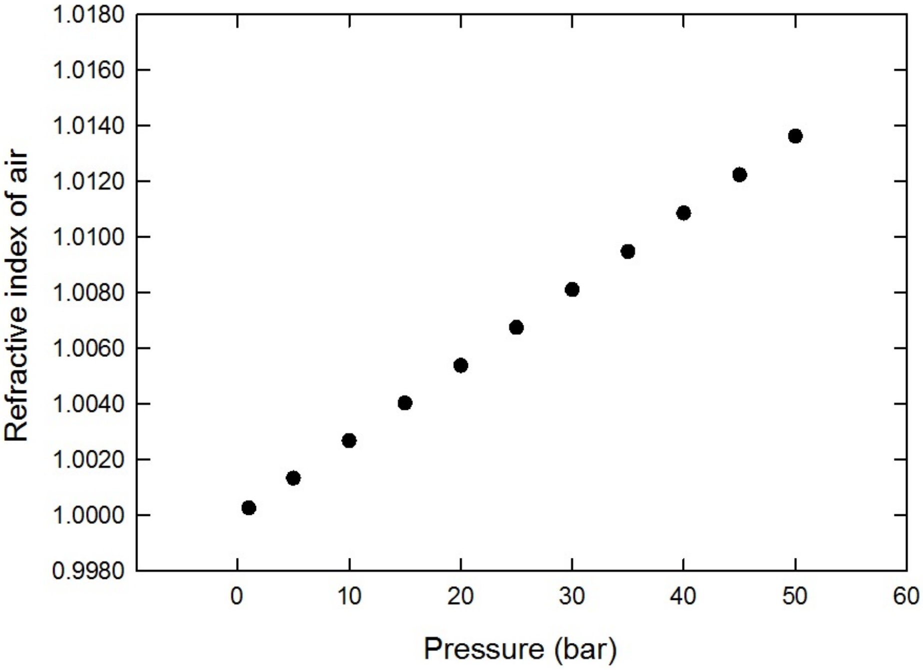

Figure 3.12: Relationship between refractive index of air and pressure

3.3.2 Refractive index of the optical window (n_{win})

The refractive index of the optical window is another important parameter used to calculate the scattering angle. In this study, the optical windows made of fused silica glass is used. Laser of 0.532 μm was used to illuminate light through the optical window and then through liquid droplets. The refractive index of fused silica glass (HPFS 7980 by Corning Inc.) was computed from the following polynomial dispersion equation [33]:

$$ {n_{win}}^2 = A_0 + A_1\lambda^4 + A_2\lambda^2 + A_3\lambda^{-2} + A_4\lambda^{-4} + A_5\lambda^{-6} + A_6\lambda^{-8} + A_7\lambda^{-10} \tag{3.3} $$

The polynomial dispersion constants A_N (N = 0 - 7) are:
$A_0 = 2.104025406$
$A_1 = -1.456000330 \times 10^{-4}$
$A_2 = -9.049135390 \times 10^{-3}$
$A_3 = 8.801830992 \times 10^{-3}$
$A_4 = 8.435237228 \times 10^{-5}$
$A_5 = 1.681656789 \times 10^{-6}$
$A_6 = -1.675425449 \times 10^{-8}$
$A_7 = 8.326602461 \times 10^{-10}$.
Equation 3.3 is applied for the thermodynamic condition: 22°C, 1.01325 bar. λ is the wavelength in μm. The resultant refractive index of the optical window (n_{win}) for wavelength of 0.532 μm is then 1.4607111.

3.3.3 Geometrical calculations

The schematic diagram of the experiment displayed in Figure 3.9 shows light paths of the 0.532 μm green laser through liquid droplets and after scattering at the rainbow angle. All parameters for the calculation of the scattering angle are shown in Figure 3.9. The first step of the calculation is to measure parameters y_1, y_2, y_3, $x_{exp,m^{th}}$ and r from experiments. Knowing r and y_2, the refracted angle in the optical window θ_b is calculated from a trigonometric function given by:

$$ \theta_b = \arctan(r/2y_2), \tag{3.4} $$

then incident angle θ_a and refracted angle in the test chamber θ_c are computed from Snell's law written as, respectively,

$$ \theta_a = \arcsin(\frac{n_{win}}{n_{air,1}} \sin\theta_b) \tag{3.5} $$

and

$$ \theta_c = \arcsin(\frac{n_{win}}{n_{air,P}} \sin\theta_b). \tag{3.6} $$

After that, angles $\theta_{1,j}$ where $j = 1$ to 25000 were generated from 1.000° to 25.000°. The generated values were increased by 0.001°. Thus, scattering angles ε_j corresponding to each $\theta_{1,j}$ were computed from Equation 3.7:

$$ \varepsilon_j = \pi - \theta_c - \theta_{1,j}. \tag{3.7} $$

Consequently, $\theta_{2,j}$ and $\theta_{3,j}$ are obtained from Snell's law and written as

$$\theta_{2,j} = \arcsin(\frac{n_{air,P}}{n_{win}} \sin(\theta_{1,j})) \tag{3.8}$$

and

$$\theta_{3,j} = \arcsin(\frac{n_{win}}{n_{air,1}} \sin(\theta_{2,j})). \tag{3.9}$$

Knowing of y_1, y_2, y_3, $\theta_{1,j}$, $\theta_{2,j}$ and $\theta_{3,j}$, signal positions x_j corresponding to each different scattering angle ε_j are computed from:

$$x_j = x_b + x_c + x_{1,j} + x_{2,j} + x_{3,j} \tag{3.10}$$

where

$$x_b = y_2 \tan(\theta_b), \tag{3.11}$$

$$x_c = y_1 \tan(\theta_c), \tag{3.12}$$

$$x_{1,j} = y_1 \tan(\theta_{1,j}), \tag{3.13}$$

$$x_{2,j} = y_2 \tan(\theta_{2,j}) \tag{3.14}$$

and

$$x_{3,j} = y_3 \tan(\theta_{3,j}). \tag{3.15}$$

Finally, signal positions x_j corresponding to each signal angle ε_j calculated from $\theta_{1,j}$ of 1.000° to 25.000°are obtained. These computed values are then used to determine the angular position of maximum intensity position of bright pattern ($\varepsilon_{exp,m^{th}}$). In the experiment, the maximum intensity positions of bright pattern ($x_{exp,m^{th}}$) were measured. The measured peak positions ($x_{exp,m^{th}}$) were compared with those x_j obtained from the computation in order to find matched positions. The matched position was a computational position which corresponded to the closest value to $x_{exp,m^{th}}$. After the matched x_j was found, the scattering angle ε_j corresponding to matched x_j was obtained and it was assumed to be the estimated angular position of the peak of bright pattern ($\varepsilon_{exp,m^{th}}$). Finally, the estimated angular position of each peak ($\varepsilon_{exp,m^{th}}$) of rainbow pattern was derived.

3.4 Determination of absolute refractive index of liquid droplets

In this work, the absolute refractive index of liquid droplets ($n_{liquid,P}$) was determined from the relative refractive index ($n'_{liquid,P}$). Since liquid inside the test chamber is surrounded by high-pressure gas, we were not able to measure directly absolute refractive index but relative refractive index. Therefore, the angular positions of rainbow signal's peaks ($\varepsilon_{exp,m^{th}}$) from Section 3.3 were firstly used to determine relative refractive index. For the analysis, the rainbow peak's angular positions were compared to those obtained from the simulations based on Debye (p=2). The process for the determination is divided into 3 steps. The first step consists in the definition of initial parameters for the simulation of rainbow signals. The second step is devoted to fit peak angular positions of simulated rainbow signals to the experimental results. In this step, the relative refractive index and size of liquid droplets can be determined. The last step concerns the calculation of the absolute refractive index. These three steps are presented in Section 3.4.1, 3.4.2 and 3.4.3, respectively.

3.4.1 Initial parameters set up for the simulation

To do the simulation, there are three important parameters used in the computation: the wavelength of incident light on liquid droplet (λ_c), droplet diameter (d) and refractive index. These three parameters were classified into two types which are fixed parameter and fitting parameter. The fixed parameter is the wavelength of incident light on liquid droplet and the fitting parameters are droplet diameter and refractive index of droplet. The beginning step of the simulation is to set initial input parameters. Firstly, the fixed parameter, the wavelength of incident light on liquid droplet, was considered. In the experiment, the wave traveled from atmosphere and then passed the optical window. Finally, it got into chamber under high pressure and came into droplets as seen in Figure 3.13. The travel of wave passing different media causes the change in wavelength and wave speed thus the wavelength of incident light on liquid droplets under different pressures can be calculated from this equation:

$$\lambda_c = \frac{0.532\mu m}{n_{air,P}}$$

where $n_{air,P}$ is the refractive index of air according to pressure in high-pressure chamber. As the incident light on droplet depends on refractive index of air inside the test chamber thus $n_{air,P}$ computed in Section 3.3.1 will be used to determine wavelength of incident light on droplets. For the fitting parameters, the approximate droplet size calculated from Equation A.7 in Appendix A was used as an initial value of droplet diameter, and the initial value of refractive index of liquid droplet was set as the absolute refractive index of liquid at atmospheric pressure. For the case of water, the initial value of refractive index was set to 1.3354 for temperature of 20°C and wavelength of 0.532 μm. After set up all these initial parameters, the simulation and the fitting of simulated data to the experiment data will be carried out.

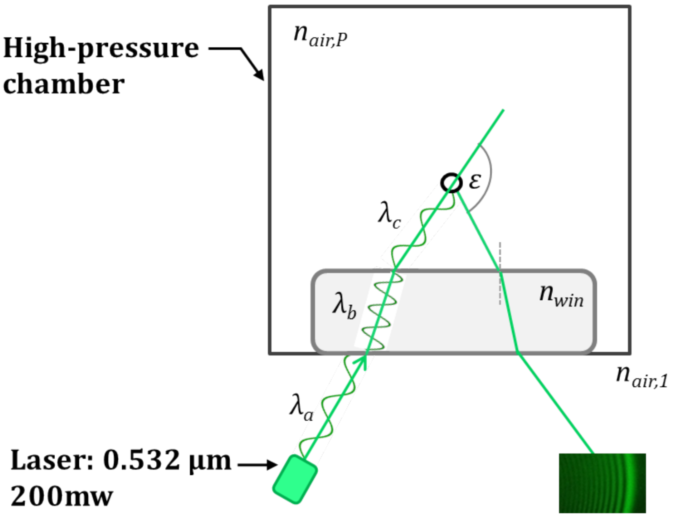

Figure 3.13: Wave propagation during the experiment under pressure

3.4.2 The simulation of rainbow signals and the fitting of simulated rainbow signals to the experimental results

This section describes the fitting method to determine relative refractive index of liquid droplet and droplet size. In the first step of the fitting, an initial value for each parameter from Section 3.4.1 was utilized in the computation of the rainbow signal. The signals were generated by varying size and refractive index while the wavelength of incident light was fixed. After that, the peak positions of simulated rainbow signals were compared to the maximum intensity positions of bright patterns from the experiment to find the best-fit positions. The diameter and refractive index producing the best-fit peak positions to the experimental data were assumed to be the average diameter and average relative refractive index of droplets. Finally, the average diameter and average relative refractive index of droplets from optical measurements were derived from the fitting method.

For example, Figure 3.14 shows the fitting of the peak positions of simulated rainbow signals to the maximum intensities positions of bright patterns of water droplets from the experiment under pressure of 15.26 bar. The green lines represent the maximum intensities positions of bright patterns of global rainbow signal of water droplets. The blue signal represents the simulated signal computed from the initial values and the red signal represents the best-fit peak positions to the experimental data. For information, the incident wavelength on liquid droplet under pressure of 15.26 bar used in this fitting is 0.52984 μm. For the generating of blue line, the initial values of relative refractive index and droplet diameter are 1.3354 and 203.14 μm, respectively. The best-fit signal, red line, is computed by using refractive index of 1.3305 and droplet diameter of 201 μm. These values were finally defined as the relative refractive index and droplet size of water droplet produced under the pressure of 15.26 bar. In this work, the fitting method is used to determine relative refractive index of water and ethanol droplets under high-pressure as well as relative refractive index of water droplets under high-pressure and at different temperatures.

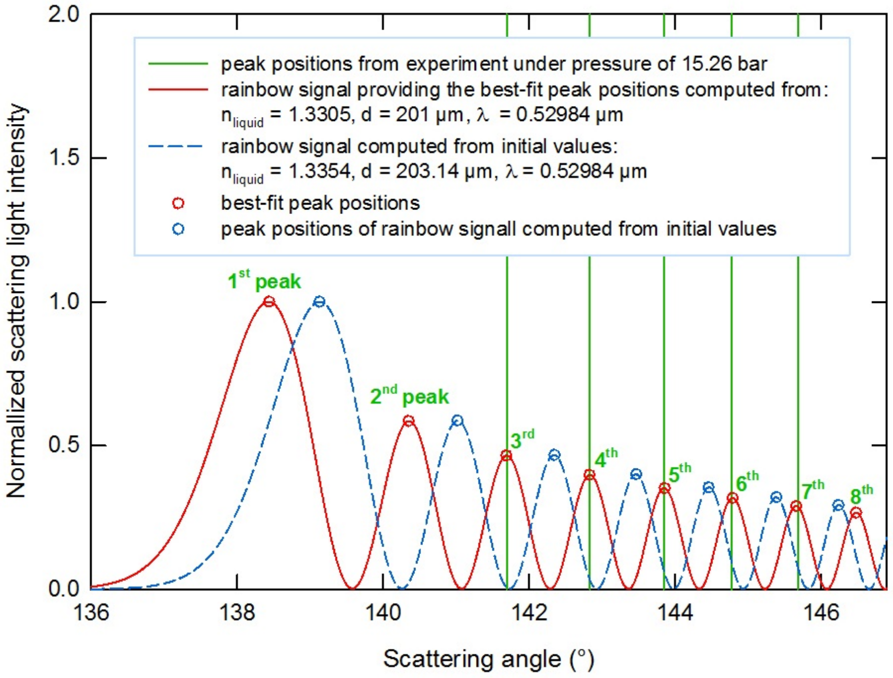

Figure 3.14: Fitting of peak positions of simulated rainbow signals to the maximum intensity positions of bright patterns of water droplets from the experiment under pressure of 15.26 bar

3.4.3 Absolute refractive index calculation

Absolute refractive index is a ratio of the velocity of light in a vacuum to the velocity of light in a medium.

$$n_{liquid} = \frac{c}{v_{liquid}} \tag{3.16}$$

Similarly, when the ray of light travels from medium 1 into medium 2, the relative refractive index is determined as the ratio of the velocity of light in medium 1 to the velocity of light in medium 2. In this work, the light travels from high-pressure air to droplet. Therefore, relative refractive index of liquid can be determined as a ratio of speed of light in high-pressure air to speed of light in liquid droplet.

$$n'_{liquid,P} = \frac{v_1}{v_2} = \frac{v_{air,P}}{v_{liquid,P}} = \frac{n_{liquid,P}}{n_{air,P}} \tag{3.17}$$

Knowing $n'_{liquid,P}$ obtained from Section 3.4.2 and $n_{air,P}$, the absolute refractive index was finally calculated from Equation 3.18:

$$n_{liquid,P} = n'_{liquid,P} \times n_{air,P}. \tag{3.18}$$

3.5 Study of window displacement effect

For an experiment under high-pressure, we had a hypothesis that the optical window of the test chamber moved out due to the increase of pressure. Therefore, we would like to study whether the window displacement modifies our optical measurement. For this reason, five simple orientations of window displacement under high pressure as shown in Figure 3.15 were considered. For the first case, the window gets pushed outward by air inside the test chamber without inclination of the window as seen in Figure 3.15(a). This case brings about the change of reflection position in +x direction. For the second and third cases, the effects also include the change of the reflection position in the x direction: +x and -x direction for the second and third case, respectively. These two cases occur for two conditions. The first condition is that the window is pushed from air inside the test chamber. The second condition is that window has an inclination from the rotating in a counterclockwise and clockwise considered in top view as seen in 3.15(b) and 3.15(c), respectively. For the fourth and fifth cases, the displacement of the window causes a change of the reflection position in the y direction: +y and -y direction, respectively. Figure 3.15(d) and 3.15(e) show the orientations of window from a pushing from pressure inside the test chamber and rotation in a counterclockwise and clockwise considered in the side view for the fourth and fifth cases, respectively. The direction of the change of the reflection position was used to classify the possible cases occurred in the experiment.

This section shows an example of a calculation of signal angular position that takes into account the window displacement for the third case. In this case, the optical window is pushed outward and it rotates in a clockwise which brings about the new reflection point moves in the -x direction. From this reason, the change of the reflection position (Δk_1) and the distance of the window displacement from the center of the window surface at atmospheric pressure in the y direction (Δy) are measured. Figure 3.16 shows a geometrical diagram of the window displacement for the third case and all variables for the calculation of rainbow peak's angular positions. Description of the variables are as follows:

y_1, distance in the y direction from droplets to the internal surface of the optical window measured at the atmospheric pressure

y_2, thickness of the optical window

y_3, distance in the y direction from the external surface of the optical window to a screen plane measured at the atmospheric pressure

y, distance in the y direction from droplets to a screen plane

$y_{1'}$, distance in the y direction from droplets to the incident point of scattered light at the internal surface of the optical window

$y_{2'}$, distance in the y direction from the incident point of scattered light at the internal surface of the optical window to the point of scattered light entering to air outside the teset chamber

$y_{3'}$, distance in the y direction from the point of scattered light entering to air outside the test chamber to a screen plane

x_1, distance in the x direction from droplets to the position of scattered light at the internal surface of the optical window

x_2, distance in the x direction from the position of scattered light at the internal surface of the optical window to the position of scattered light at the external surface of the optical window

x_3, distance in the x direction from the position of scattered light at the external surface of the optical window to the rainbow signal position

x_{123}, distance in the x direction from droplets to the rainbow signal

k_1, distance in the x direction from the point of incidence of 0.532 μm laser at the external surface of window to the first reflection point measured at the atmospheric pressure

k_{11}, distance in the x direction from the position of 0.532 μm laser at a screen plane to the incident point at the external surface of the optical window measured under high pressure

k_{12}, distance in the x direction from the incident point at the external surface of the optical window to the new reflection point measured under high pressure

Δk_1, distance between reflection point measured at atmospheric pressure to the new reflection point measured under high pressure

Δy, distance of window displacement in the y direction from center of window's external surface when it is at atmospheric pressure to point o_1

Δz, distance in the y direction from the point of incident light of 0.532 μm laser at an window's external surface to a point o_1

l_1, distance between point o_2 and point o_1

l_2, distance between droplets and point o_2

l_3, perpendicular distance from droplet to window's internal surface after moving

l_4, distance from droplets to the incident point of scattered light at window's internal surface after moving

l_5, distance from the incident point of scattered light at window's internal surface to the point of scattered light entering to air outside the test chamber

$n_{air,P}$, refractive index of air in test chamber related to air pressure in chamber

n_{win}, refractive index of the optical window

$n_{air,1}$, refractive index of air in atmospheric pressure

$\theta_{a'}$, incident angle of incident light ,illuminated by 0.532 μm laser, to the external surface normal of the optical window

$\theta_{b'}$, refraction angle of the propagating light in optical window

$\theta_{c'}$, refraction angle of the propagating light in high-pressure test chamber

$\theta_{1'}$, incident angle of scattered light to the internal surface normal of the optical window

$\theta_{2'}$, refraction angle of the propagating light in optical window

$\theta_{3'}$, refraction angle of the propagating light outside chamber

ε, scattered angle of liquid droplet around rainbow angle.

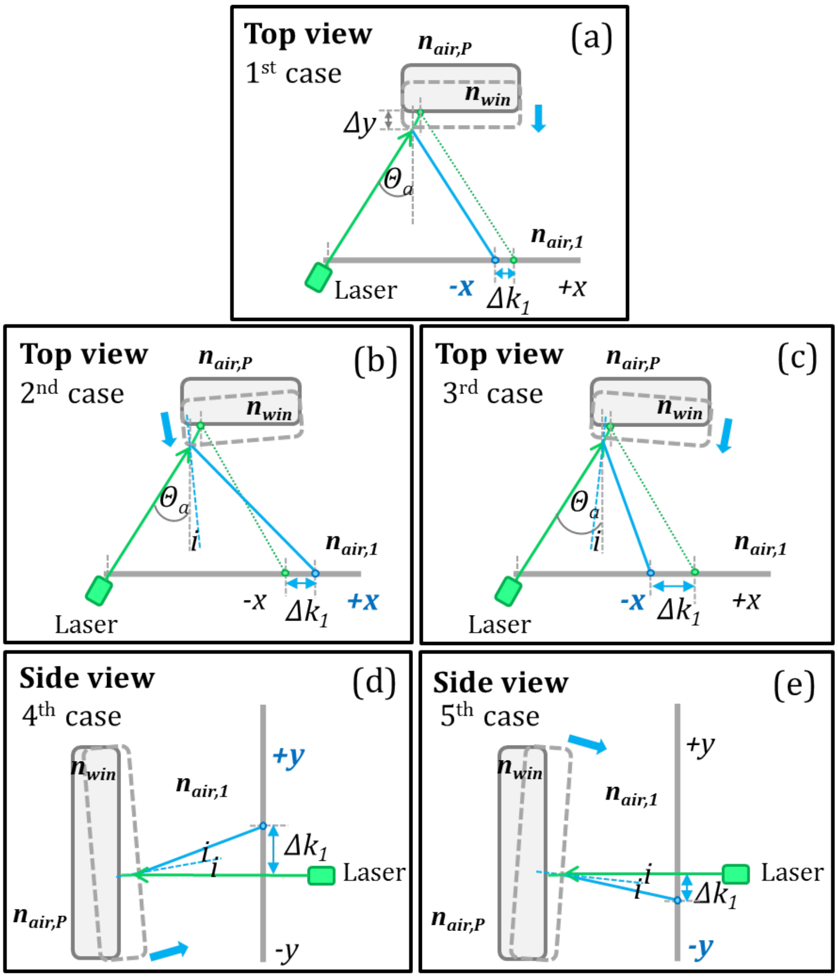

Figure 3.15: Five simple orientations of window displacement due to pressure (a) window is pushed outward (b) window is pushed outward and rotates in a counterclockwise (top view) resulting in an inclination angle of i° and a changing of a reflection position in +x direction (c) window is pushed outward and rotates in a clockwise (top view) resulting in an inclination angle of i° and a changing of a reflection position in -x direction (d) window is pushed outward and rotates in a counterclockwise (side view) resulting in an inclination angle of i° and a changing of a reflection position in +y direction (e) window is pushed outward and rotates in a clockwise (side view) resulting in an inclination angle of i° and a changing of a reflection position in -y direction

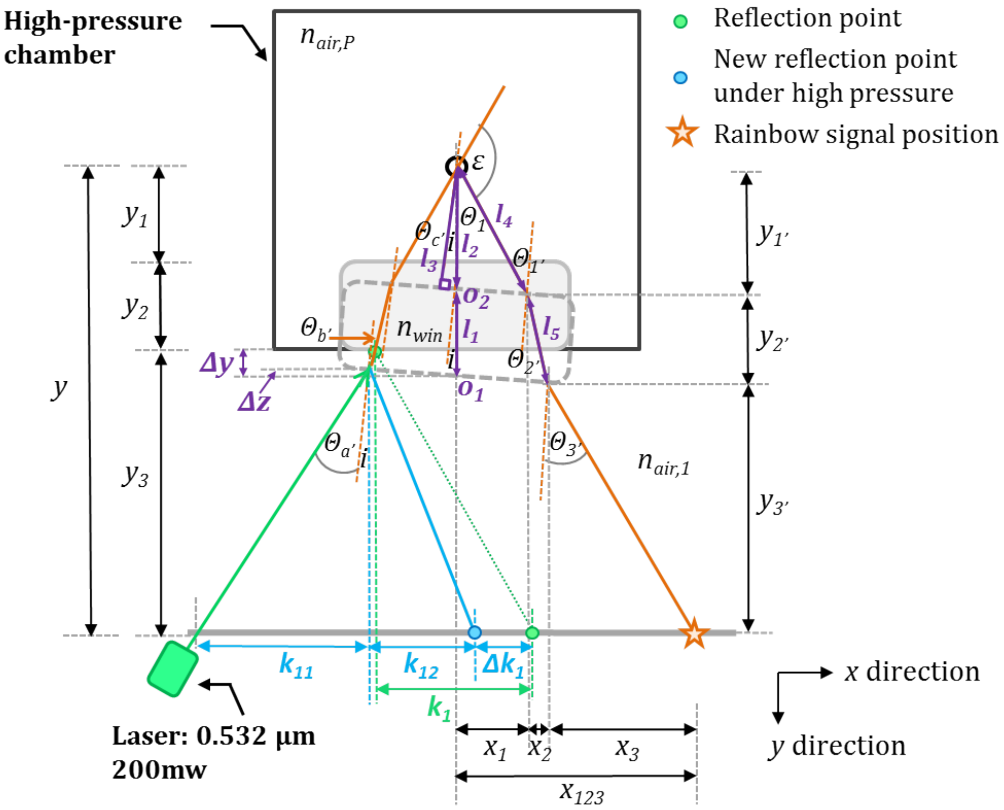

Figure 3.16: Orientation of the move of the optical window and the light path from the laser source through the screen for the third case (top view)

In an experiment under high pressure, the change of reflection position (Δk_1) and the window displacement in the y direction from the center of window surface at atmospheric pressure (Δy) were measured. The distance y_3 and angle θ_a were derived from the measurement at the atmospheric pressure. These values were used to determine the angular position of scattered light around rainbow angle. The first important step for the determination is to obtain the inclination (i) of window corresponding to the change of reflection position (Δk_1) and distance Δy measured from experiment. For that, we generated i_k from 0.001° to 5° where $k = 1$ to 5000. The generated values were increased by 0.001°. The generated inclinations i_k were used to compute $\Delta k_{1,k}$ from Equation 3.19-3.24:

$$\theta_{a',k} = \theta_a - i_k, \tag{3.19}$$

$$\Delta z_k = 15 \arctan i_k, \tag{3.20}$$

$$k_{11,k} = (y_3 - \Delta y - \Delta z_k) \arctan(\theta_{a',k} + i_k), \tag{3.21}$$

$$k_{12,k} = (y_3 - \Delta y - \Delta z_k) \arctan(\theta_{a',k} - i_k), \tag{3.22}$$

$$k_1 = y_3 \arctan \theta_a, \tag{3.23}$$

and

$$\Delta k_{1,k} = 2k_1 - k_{11,k} - k_{12,k}. \tag{3.24}$$

.

For Equation 3.20, we assumed that the distance in the x direction from o_1 to the point of incidence at the external surface of window is equal to 15 mm. After computations, $\Delta k_{1,k}$ were compared to Δk_1 measured from experiment in order to determine i from the closest value. Finally, we obtained the inclination angle (i) and the laser incident angle ($\theta_{a'}$). These values were then used to calculate the refraction angles $\theta_{b'}$ and $\theta_{c'}$ from Snell's law as the following equations:

$$\theta_{b'} = \arcsin(\frac{n_{air,1}}{n_{win}} \sin(\theta_{a'})) \tag{3.25}$$

and

$$\theta_{c'} = \arcsin(\frac{n_{win}}{n_{air,P}} \sin(\theta_{b'})). \tag{3.26}$$

In the next step, the scattered light angular position of the rainbow signal (ε_{exp}) will be determined. The angles $\theta_{1',j}$ were firstly computed following Equation 3.27 by knowing i and $\theta_{1,j}$. $\theta_{1,j}$ were generated from 1.000° to 25.000° step by 0.001°where j = 1 to 25000. Thus, scattering angle ε_j corresponding to each $\theta_{1',j}$ can be computed from Equation 3.28:

$$\theta_{1',j} = \theta_{1,j} + i \tag{3.27}$$

and

$$\varepsilon_j = \pi - \theta_{c'} - \theta_{1',j}. \tag{3.28}$$

Consequently, $\theta_{2',j}$ and $\theta_{3',j}$ were obtained from Snell's law and written as

$$\theta_{2',j} = \arcsin(\frac{n_{air,P}}{n_{win}} \sin(\theta_{1',j})) \tag{3.29}$$

and

$$\theta_{3',j} = \arcsin(\frac{n_{win}}{n_{air,1}} \sin(\theta_{2',j})). \tag{3.30}$$

.

We aimed to derive $x_{123,j}$ corresponding to each $\theta_{1',j}$ in order to compare them with $x_{123,exp}$. The closest value to $x_{123,exp}$ will be used to determine angular position of the rainbow signal (ε_{exp}). $x_{123,j}$ is derived from these equations:

$$y = y_1 + y_2 + y_3, \tag{3.31}$$

$$l_1 = \frac{y_2}{cos(i)}, \tag{3.32}$$

$$l_2 = y_1 + y_2 - l_1 + \Delta y, \tag{3.33}$$

$$l_3 = l_2 \cos(i), \tag{3.34}$$

$$l_{4,j} = \frac{l_3}{\cos(i + \theta_{1,j})}, \tag{3.35}$$

$$l_{5,j} = \frac{y_2}{\cos(\theta_{2',j})}, \tag{3.36}$$

$$y_{1',j} = l_{4,j} \cos(\theta_{1,j}), \tag{3.37}$$

$$x_{1,j} = l_{4,j} \sin(\theta_{1,j}), \tag{3.38}$$

$$y_{2',j} = l_{5,j} \cos(\theta_{2',j} - i), \tag{3.39}$$

$$x_{2,j} = l_{5,j} \sin(\theta_{2',j} - i), \tag{3.40}$$

$$y_{3',j} = y - y_{1',j} - y_{2',j}, \tag{3.41}$$

$$x_{3,j} = y_{3',j} \tan(\theta_{3',j} - i), \tag{3.42}$$

and

$$x_{123,j} = x_{1,j} + x_{2,j} + x_{3,j}. \tag{3.43}$$

The distance $x_{123,exp}$ of each peak obtained from experiment was compared to $x_{123,j}$ corresponding to each ε_j. Finally, the closest value provided $\varepsilon_{exp,m^{th}}$ corresponding to $x_{123,exp}$ of each peak position. After knowing angular position of maximum intensities positions of rainbow signal's bright patterns, we used these values to determine the refractive index of free-falling water droplets under high pressure with taking into account the displacement of window. For the determination of the refractive index, the method from Section 3.4 was used. The results of the refractive index will be compared to those determined without taken into account the window displacement.

3.6 Experimental results

3.6.1 Behavior of water droplets under pressure up to 40 bar

From an experimental point of view, the line of mono-disperse droplets at atmospheric pressure can be produced by setting and adjusting the excited frequency and volume flow rate following the procedure from Section 3.2.3. The image of water droplets produced is presented in Figure 3.17(a). In case of water droplets produced under high pressure (up to 45 bar), the behavior was not the same as those produced at room pressure. A transformation of the line of droplets into nearly monodisperse spray (spray at its bottom part) appears as shown in Figure 3.17(b). In addition, the spray pattern at the bottom part becomes longer and wider when the pressure in the test chamber increases. Figure 3.18(a) shows the diagram of behavior of droplets under pressure of 1, 7.5 and 30 bar, respectively. To reduce spray effect under high-pressure, the volume flow rate was decreased when the pressure was increased. Figure 3.17(b) presents the spray pattern of droplets under pressure of 30 bar after decreasing the volume flowrate. It shows that the spray at the bottom part of line of droplets was reduced when the volume flow rate was decreased. Lastly, this adjustment procedure was applied for experiments under high pressure.

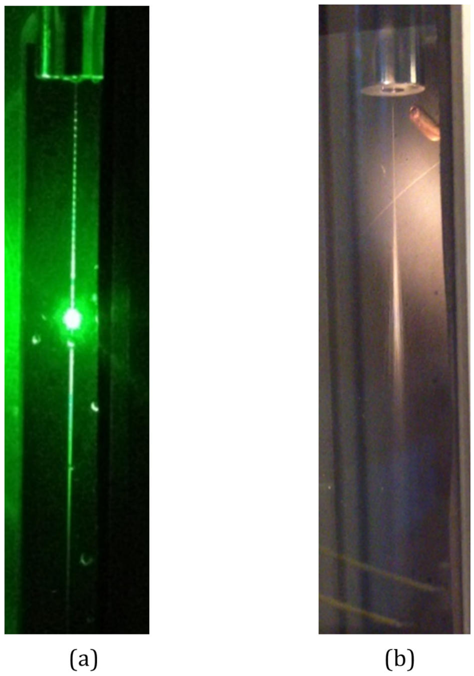

Figure 3.17: Image of behavior of droplets from experiments (a) line of water droplets injected at an atmospheric pressure (b) water droplets injected at $\dot{V}$ of 1.8 ml/min under pressure of 40.4 bar

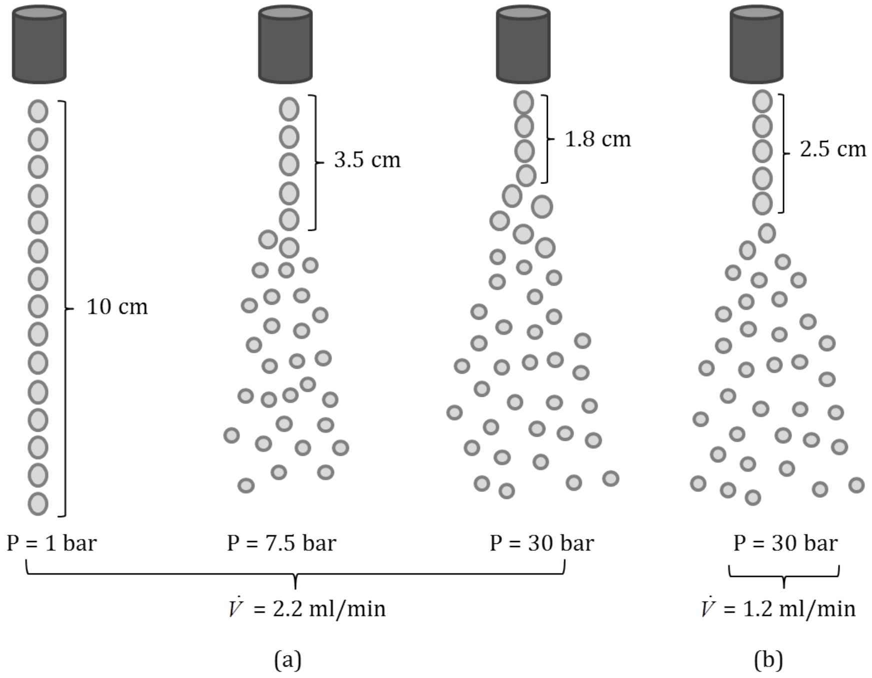

Figure 3.18: Diagram of behavior of droplets (a) droplets infused at $\dot{V}$ of 2.2 ml/min under pressure of 1, 7.5 and 30 bar (b) droplets infused at $\dot{V}$ of 1.2 ml/min under pressure of 30 bar

3.6.2 Observation of rainbow signal of water droplets under pressure up to 45 bar

This section shows the optical measurement of the results. At atmospheric pressure, we are able to produce a line of monodisperse droplets as a stable rainbow signal and its ripple structure can be observed. However, the rainbow signal from experiments under high pressure was not stable and the ripple structure disappeared. As described in Section 3.6.1, line of droplets is transformed into a nearly monodisperse spray when the pressure was higher than 1 bar. Examples of rainbow signals observed under pressure of 20 bar are shown in Figure 3.19. Figure 3.19(a) presents the rainbow signal observed from nearly monodisperse spray produced at $\dot{V}$ of 2.2 ml/min whereas Figure 3.19(b) shows the rainbow signal observed from nearly monodisperse spray produced at $\dot{V}$ of 1.6 ml/min. The rainbow signal in Figure 3.19(a) is more blurry than in Figure 3.19(b) due to the existence of jet instabilities during experiments. The better signal produced at $\dot{V}$ of 1.6 ml/min was obtained after adjusting $\dot{V}$. Accordingly, the measurements of refractive index under high pressure (up to 45 bar) have been carried out by using an adapted global rainbow optical technique to observe scattering light of nearly monodisperse spray instead of monodisperse droplets.

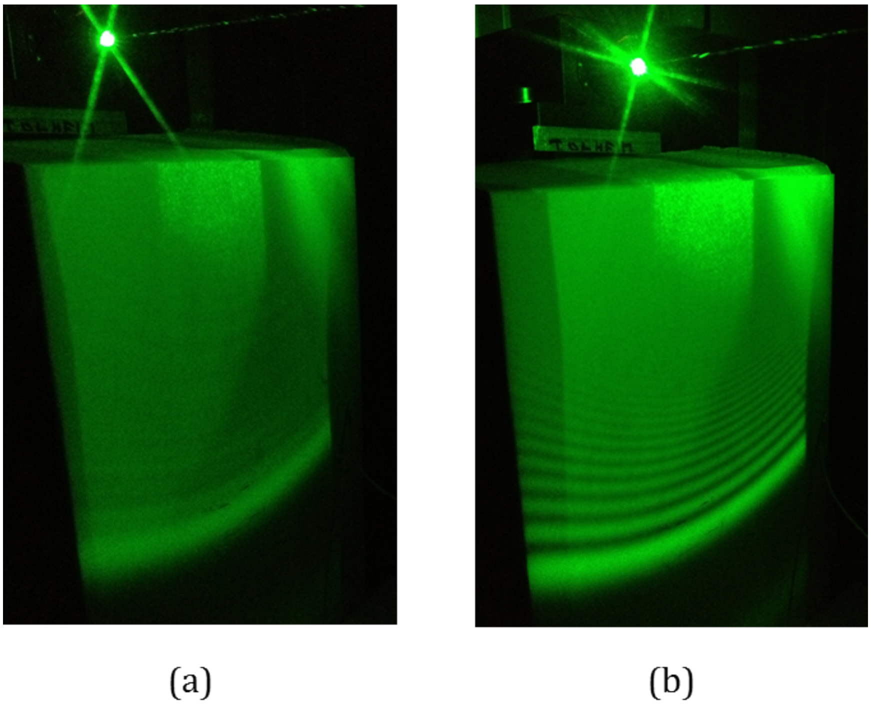

Figure 3.19: Rainbow signal observed under pressure of 20 bar (a) rainbow signal produced at $\dot{V}$ of 2.2 ml/min (b) rainbow signal after adjusting $\dot{V}$ to 1.6 ml/min

3.7 Validation of refractive index measurements on free-falling water and ethanol droplets

3.7.1 Pressure dependence of refractive index of water

We firstly validated the global rainbow technique by performing measurements on water. From the results of measurements, we found that the scattering light around the rainbow angle of water droplets changes its position with pressure. The observed rainbow signal location moved to the direction which had smaller angle when pressure is increased. Table 3.3 shows angular positions of rainbow signal's peaks observed at various pressures. Considering the fourth peak from Table 3.3, the angular positions of this peak was smaller when the pressure was higher. Figure 3.20 shows the direction of the move of rainbow signal position when the pressure increased.

After knowing the angular position corresponding to each peak, we fitted our results with simulated data to determine the relative refractive index ($n'_{water,P}$) and average size of droplets. Relations of relative refractive index of water and pressure from three distinct experiments compared to the absolute refractive index of water from Schiebener et al., 1990 [6] are shown in Figure 3.21. The relative refractive index of water droplets is linearly decreasing due to the increase of pressure while the absolute refractive index from literature displays a very small increase compared to the decrease of relative index as presented in Figure 3.21. For experiments under high pressure, the density of air inside the test chamber changes due to the pressure as well as its refractive index ($n_{air,P}$). From this reason, the refractive index of air ($n_{air,P}$) was taken into account for the calculation of absolute refractive index of droplets. For water, thermodynamic conditions in which droplets are injected are far from its critical point (critical pressure of 221 bar and critical temperature of 374°C). Therefore, water droplets have a low evaporation rate and only pure air surrounding water droplets can be considered. Absolute refractive index were then determined from relative refractive index and absolute refractive index of air inside the test chamber. Results are shown in Table 3.4. This table shows the pressure of air inside the test chamber (P_{inside}), the temperature of air inside the test chamber ($T_{air,inside}$), the temperature of air outside the test chamber ($T_{air,outside}$), the wavelength of incident light on liquid droplets inside the test chamber (λ_c), the droplet size calculated from volume flow rate and excitation frequency (d_{cal}), the droplet size determined from data processing ($d_{fitting}$), the refractive index of air due to pressure ($n_{air,P}$), the relative refractive index ($n'_{liquid,P}$) and the absolute refractive index determined from measurement ($n_{liquid,P}$) for a series of measurements performed in the same day. We found that the average diameter of droplets obtained from the fitting analysis has a small difference to those calculated from volume flow rate and excitation frequency in the range of ± 10 μm. Figure 3.22 shows the relative and absolute refractive indices of water at different pressures determined from the fitting with an uncertainty of 0.002, and absolute refractive indices from Schiebener et al, 1990 [6]. To validate our optical measurement technique, the absolute refractive index from the experiments were compared to reference data from literature where measurements were performed in cells filled with liquid under high-pressure conditions. The experimental results with the given uncertainty are in good agreement with data issued from Schiebener et al., 1990 [6]. This confirms the validity of our measurement method.

Table 3.3: Angular position of each peak

P_{inside}	Peak position						
(bar)	2nd	3rd	4th	5th	6th	7th	8th
1.01	141.3179	142.8319	144.1344	145.3039	146.3334	147.3089	
15.26		141.6977	142.8342	143.8457	144.7752	145.6797	
30.24			142.4828	143.6183	144.5763	145.5048	146.4423
39.90			141.7691	142.9006			

Table 3.4: Measurement data, calculated data and results of rainbow signal fitting process (experiment on August 31st, 2016).

P_{inside} (bar)	$T_{air,inside}$ (°C)	$T_{air,outside}$ (°C)	λ_c (μm)	d_{cal} (μm)	$d_{fitting}$ (μm)	$n_{air,P}$	n_{rela}	n_{abs}
1.01	23.90	24.40	0.53186	167.40	165	1.0002698	1.3346	1.3350
15.26	24.10	24.80	0.52984	203.14	201	1.0040826	1.3305	1.3359
30.24	24.20	24.90	0.52771	183.24	179	1.0081322	1.3249	1.3357
39.90	24.40	25.10	0.52634	181.89	179	1.0107599	1.3200	1.3342

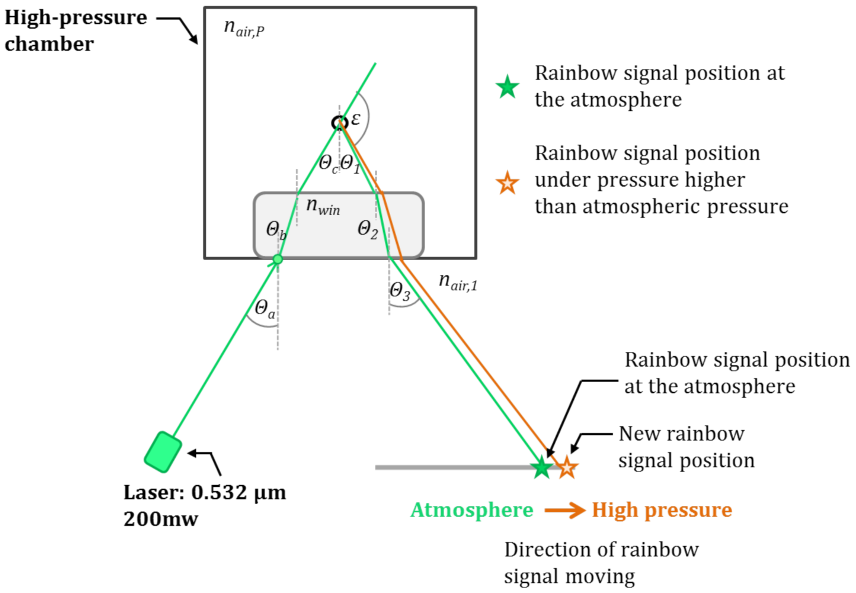

Figure 3.20: Diagram of light paths that travels to liquid droplets at atmospheric pressure and under high pressure and their scattering positions around rainbow angles

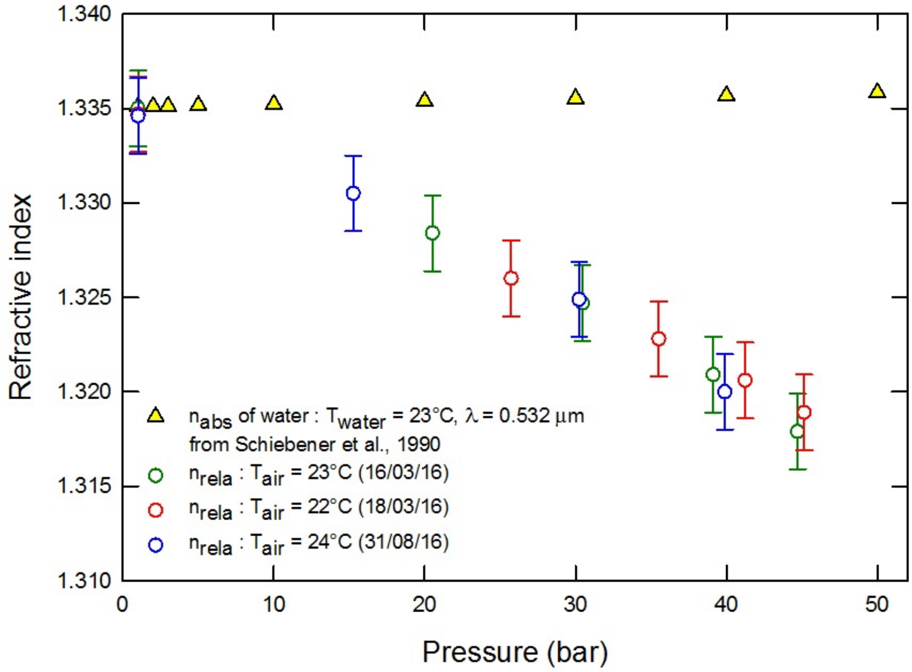

Figure 3.21: Pressure dependence of relative refractive index of water droplets

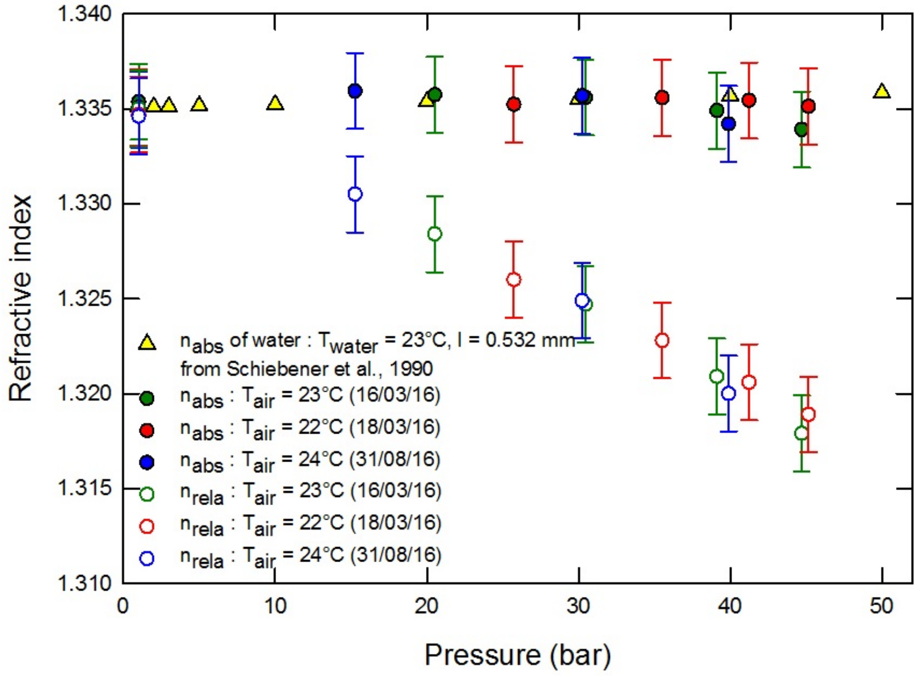

Figure 3.22: Pressure dependence of the relative and absolute refractive index of water droplets

3.7.2 Result of the study of window displacement effect

In the experiments under pressure up to 45 bar, we found a slightly change in the x direction of the reflection points (Δk_1) (i.e. up to ± 1.0 mm). This is due to the move of the optical window's position. In this case, we would like to test our hypothesis: "Does a window displacement due to a difference gas pressure between inside and outside the test chamber change the optical measurement?". For that, we calculated refractive index of liquid water under high-pressure by taking into account the window displacement and then compared them to those obtained without taking into account this displacement. We assumed that the window did not have an inclination when performing experiments at atmospheric pressure. For the series of measurements recorded on March 16th, 2016, when the pressure inside the test chamber increased, the reflection position at the screen moved in -x direction. We considered the possible cases of window displacements from Figure 3.15. There are two possible cases for this experiment: the first and the third cases. The distance between the new reflection position and the one measured at atmospheric pressure (Δk_1) is 0.8 mm and Δy is 0.01 mm. Considering the first case, when Δy is 0.01 mm, Δk_1 is only 0.006 mm, which is largely different to the experiment. Considering the third case which takes into account the inclination of window, the new angular positions of the rainbow signal show that the maximum difference between the rainbow signal angular position calculated with and without taking into account the window displacement is only 0.0006°. After calculating the angular position of each peak, the relative and absolute refractive index were then determined. Table 3.5 shows the inclinations of window and absolute refractive indices of free-falling water droplets from the data processing. The results of the relative and absolute refractive indices of liquid water derived by taking into account window effect were compared to the results obtained without taking into account the window displacement. As seen in Figure 3.23, the window displacement does not affect the optical measurement. In conclusions, the window displacement has no influence for the data process of optical measurements.

Table 3.5: Measurement data: inclination of window under high pressure and absolute refractive index from the experiment on March 16th, 2016 with and without taken into window displacement effect

P_{inside} (bar)	i (°)	Δy (mm)	$\Delta k_{1,k_{match}}$ (mm)	$\Delta k_{1,exp}$ (mm)	n_{abs} (with displacement)	n_{abs} (without displacement)
1.01					1.3354	1.3354
20.52	0.020	0.01	0.84	0.8	1.3357	1.3357
30.46	0.024	0.02	1.00	1.0	1.3356	1.3356
39.12	0.024	0.03	1.00	1.0	1.3349	1.3349
44.71	0.020	0.03	0.84	0.8	1.3339	1.3339

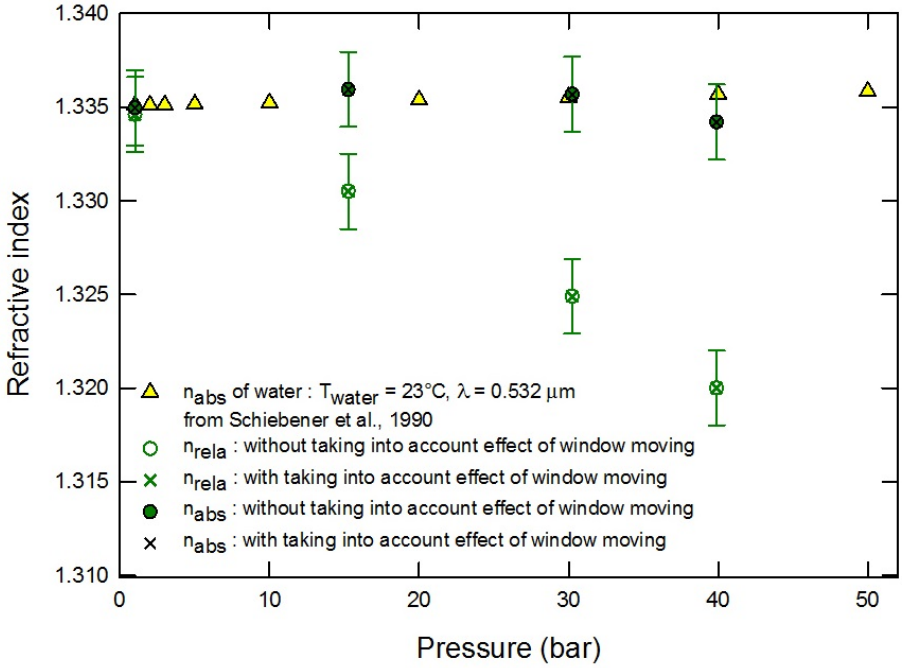

Figure 3.23: The relative and absolute refractive index of water droplets determined with and without taking into account window displacement effect

3.7.3 Pressure dependence of refractive index of ethanol

In order to confirm the reliability of the experimental methodology, the optical measurement of refractive index of free-falling ethanol droplets under high pressure up to 30 bar has been carried out. The relations between relative refractive index and pressure of ethanol droplets compared with the water results is shown in Figure 3.24. The relative refractive index of both liquid water and ethanol decreased when the pressure is higher. As seen in Figure 3.24, the decrease of the relative refractive indices of liquid ethanol and water are similar. After that, we took into account the refractive index of air under high pressure to determine the absolute refractive index, we found that the absolute refractive index of ethanol droplets has a small decrease as shown in Figure 3.25. Table 3.6 shows the measurement data, calculated data and results of rainbow signal fitting process from the measurement on ethanol droplets (measurements during September 12th, 2016). We found that the average diameter from the fitting analysis was smaller than those calculated from volume flow rate and excitation frequency in the range of 14 μm . For measurements with ethanol, reference data of refractive index for pressure in the range of our measurements (1-30 bar) are not available. However, we had reference data on the relationship between absolute refractive index and pressure at very high pressure for liquid ethanol and water (Figure 3.26). This graph shows that the absolute refractive index of liquid ethanol and water increase with pressure. While the relative refractive index measured under pressure of 1-40 bar on liquid water and ethanol had a similar trend as seen in Figure 3.24, the trend of the variation of the absolute refractive index of ethanol and water are not the same: water has increasing trend while ethanol has decreasing trend. It may well be that the only consideration of air inside the test chamber as a gas surrounding droplets is not enough. In this case, the gas surrounding droplets is not only pure air but a mixing of air with evaporated ethanol.

Table 3.6: Measurement data, calculated data and results of rainbow signal fitting process from a series of experiment recorded on September 12th, 2016

P_{inside} (bar)	$T_{air,inside}$ (°C)	$T_{air,outside}$ (°C)	λ_c (μm)	d_{cal} (μm)	$d_{fitting}$ (μm)	$n_{air,P}$	n_{rela}	n_{abs}
1.01	23.5	23.6	0.53186	186.08	186	1.0002702	1.3627	1.3631
10.19	24.0	24.1	0.53056	187.40	177	1.0027220	1.3584	1.3621
21.27	24.3	24.4	0.52899	235.66	212	1.0056991	1.3535	1.3612
31.87	24.6	24.6	0.52748	216.56	203	1.0085630	1.3491	1.3607

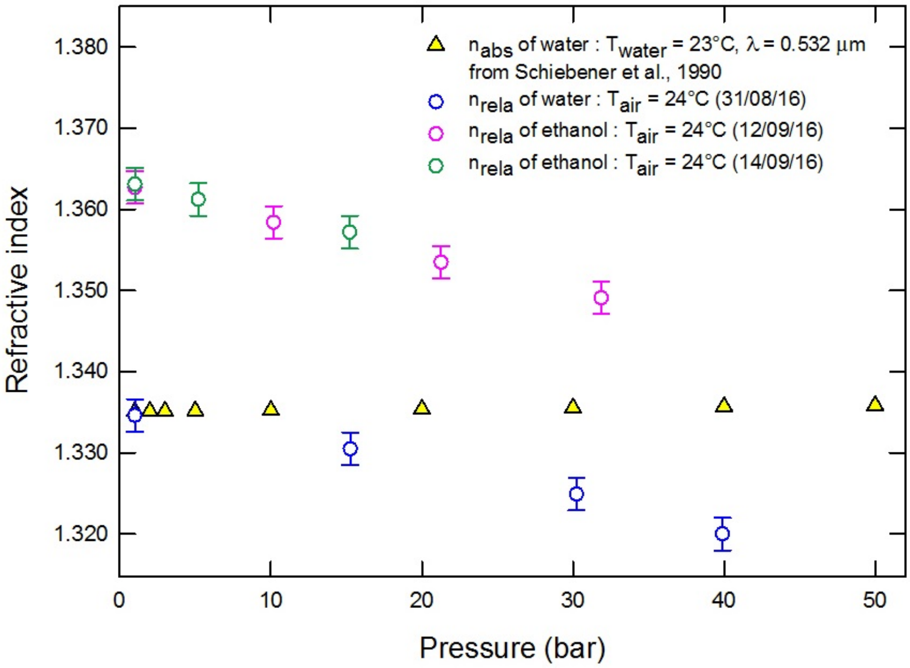

Figure 3.24: Pressure dependence of relative refractive index of ethanol and water droplets

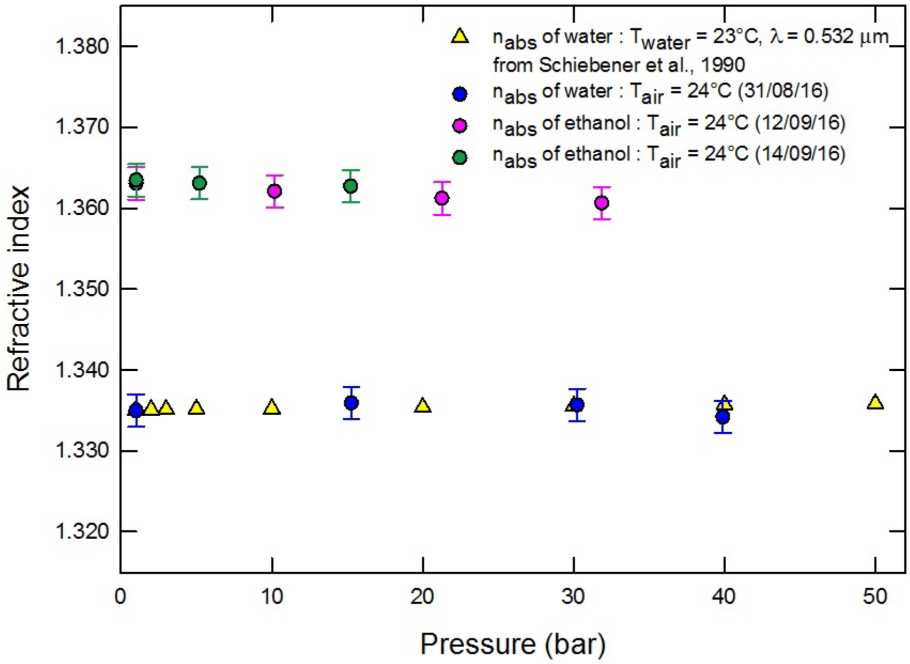

Figure 3.25: Pressure dependence of absolute refractive index of ethanol and water droplets

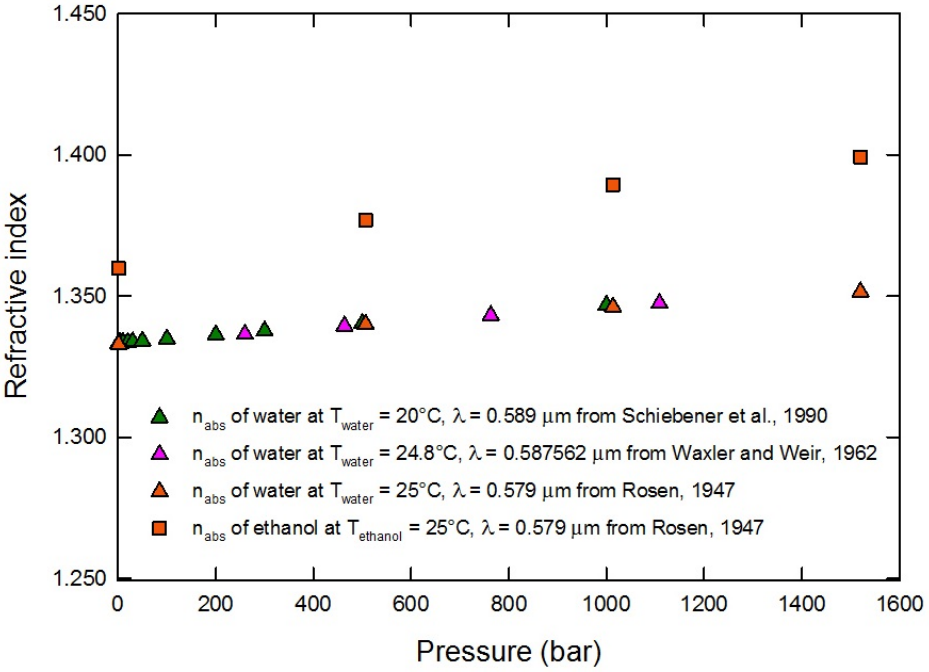

Figure 3.26: Pressure dependence of absolute refractive index of liquid ethanol and water from the literature

3.7.4 Pressure and temperature dependence of refractive index of water

Temperature is also one of the scalar parameter that affects the refractive index of liquid. Therefore, we would like to control the temperature as well as pressure. In this work, the measurement has been carried out at temperature of 50°C under pressure of 1 and 10 bar, respectively. Temperature of air inside the test chamber was controlled by the heat brought by the heat cartridges as described in Section 3.2.5. Air inside test chamber is then heated until the temperature reach to 50°C. The experiment was performed when the system was in thermal equilibrium. After that, the absolute refractive index was measured under pressure of 1 and 10 bar, respectively. Figure 3.27 shows the absolute refractive index of free-falling water droplets at temperature of 23°C and 50°C at different pressures in comparison with the reference data of Schiebener et al., 1990 (measurement in cells filled with liquid). We found that our results are in good agreement with the results obtained from Schiebener et al., 1990 (Figure 3.27). The refractive index of water droplets measured in these conditions confirms the reliability of the experimental methodology developed in the current study.

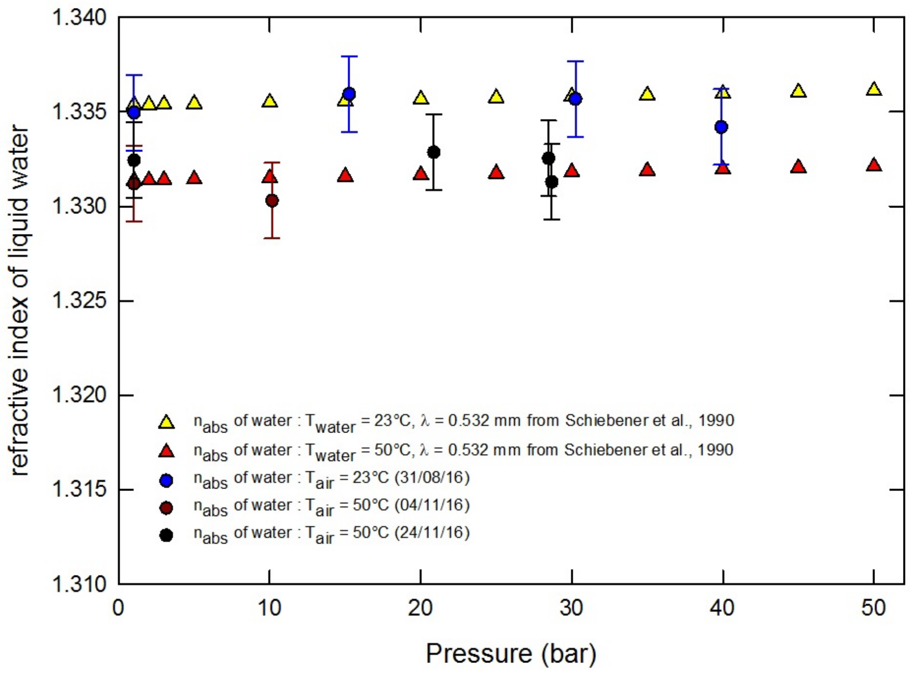

Figure 3.27: Pressure and temperature dependence of absolute refractive index of water droplets

3.8 Conclusions

In this study, the behavior of droplets under high pressure up to 45 bar has been investigated. The line of spherical monodisperse droplets can be produced at atmospheric pressure. When the pressure is increased, the line of monodisperse droplets is transformed into line of nearly monodisperse spray. In this case, the volume flow rate was adjusted to reduce spray behavior at the bottom part of the line and produce more stable rainbow signal. After that, the injection method has been improved. An adapted global rainbow optical technique was developed and used to measure the average refractive index and the average sizes of free-falling water droplets.

The average size and relative refractive index were derived from the data processing of rainbow measurements. The average size from experimental measurements were slightly different to the size computed assuming monodisperse droplets [31]. The difference between them were in range of $\pm 10\mu$m. Relative refractive index of water droplets displays a decrease with pressure. In this data processing, the window displacement effect can be neglected because this one is not significant compared to systematic error induced from measurements. The absolute refractive index of water droplet measured in this study was determined by taking into account the refractive index of air under high pressure in test chamber. The absolute refractive index measured on free-falling water droplets under high-pressure conditions of 1 to 45 bar and at temperatures around 20°C to 25°C were determined. The experimental results are in good agreement with those obtained from measurements in cell filled with liquid water under high pressure (Schiebener et al., 1990).

Moreover, we also performed measurements on free-falling ethanol droplets. The measurements were carried out under pressure of 1 to 30 bar and temperature of 23-24°C. The relative refractive index measured on ethanol droplets shows similar behavior to the one deduced from water droplets. However, the absolute refractive index calculated by taking into account only air refractive index shows a decrease with pressure.

In addition, measurements of absolute refractive index were also performed by controlling both temperature and pressure. We measured absolute refractive index at temperature of 50°C and pressure of 1 and 10 bar on water droplets. The absolute refractive index from these measurements are in good agreement with reference data from literature.

Results of measurements on water and ethanol droplets highlighted our developed refractive index measurement methodology on free-falling droplets under large thermodynamic conditions. Therefore, we are now able to measure absolute refractive index of free-falling droplets as a function of temperature and pressure using an adapted global rainbow optical technique.

CHAPTER 4

Optical measurement on free-falling ethane droplets under high pressure

4.1 Introduction

Due to the deficiency of measurements of fuel droplets when approaching the critical point, the study is focused on optical measurements of free-falling ethane droplets in elevated pressure near the critical point. In this study, an adapted rainbow refractometry is used for measurements of the average refractive index and the average size of moving ethane droplets. The experimental setup, the methodology of optical measurements and the analysis of results are presented in this chapter.

4.2 Experimental setup and methodology

In this section, the method to produce liquid ethane and the associated optical measurement for rainbow measurements on liquid ethane are reported. For that, the experimental system used initially for water and ethanol was modified to be able to inject liquid ethane droplets inside the test chamber. The experimental setup for this process and the procedure to generate ethane droplets are presented in Section 4.2.1. Moreover, the setup for the adapted global rainbow refractometry and the methodology of measurements are presented in Section 4.2.2.

4.2.1 Production and injection of liquid ethane

The production of ethane droplets is the first step to be focused in this study, since originally ethane is stored in a vapor phase in a storage tank. The pressure of ethane in the storage tank ranges between 36 and 41 bar depending of the temperature of storage. The physical state of ethane in the storage tank on the pressure-temperature phase diagram of ethane is presented in Figure 4.1. This diagram shows that ethane in the tank at ambient temperature of 22°C is in vapor. As the optical measurement in this work will be carried out on liquid ethane droplets, ethane vapor contained in the tank needs to be pressurized to be converted into liquid. In this case, ethane vapor needs to be pressurized larger than 40 bar to become liquid as shown in Figure 4.1.

To start the liquid generating process, a fluid supply system was specifically designed. This system was modified from the liquid supply system used for experiments with water and ethanol. Figure 4.2 shows the schematic diagram of the air pressurization system and the associated fluid supply system designed for measurements on ethane droplets under high-pressure up to 50 bar. As the syringe pump was used to push liquid to produce monodisperse droplets, this one was also used to pressurize ethane vapor. To improve the conversion of ethane vapor in liquid, the volume of a fluid supply system need to be minimized to reach the highest pressure as possible. For that, liquid pipeline was cut off and the connection of the system was modified. The filter was removed as well as a vent pipe connected to a droplet generator. The modification of the fluid supply system is presented in a red circle in Figure 4.2 and the image of fluid supply system after modification is shown in a red circle in Figure 4.3. The experimental setup in this work is also shown in Figure 4.4.

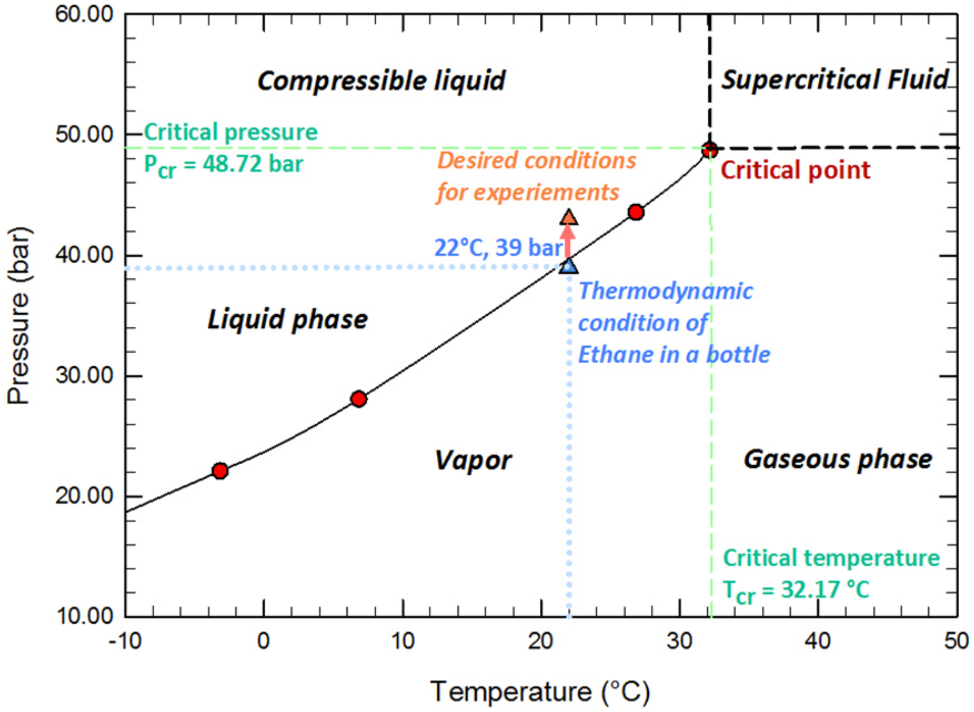

Figure 4.1: Physical state ethane in the storage tank on the pressure-temperature phase diagram of ethane

After the fluid supply system was modified, the method to generate liquid ethane was then defined and optimized. Finally, ethane droplets are produced. The procedure for preparing liquid ethane follows these steps:

1. At the beginning, the syringe's plunger was pressed all the way.

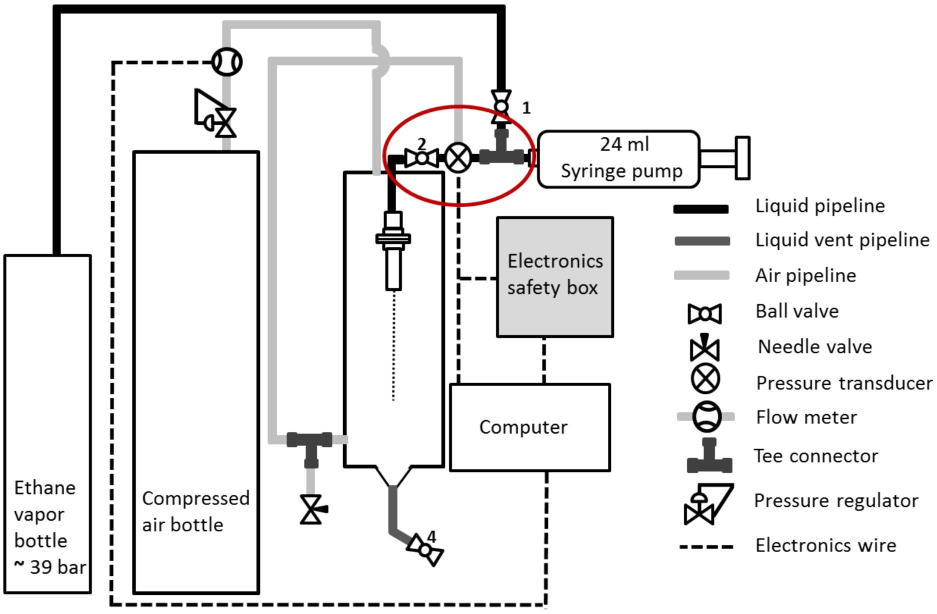

Figure 4.2: Schematic diagram of a connection of air pressurization system and a fluid supply system

2. The air in the fluid supply system was initially purged by using high-pressure ethane vapor from the bottle (about 37-41 bar). In this case, the second valve was opened and the first valve was used for the flows control of ethane vapor. Positions of all control valves are shown in Figure 4.2
3. After the air was purged from the fluid supply system, the first and the second valves were then closed. The plunger of the syringe was then pulled back to get 24 ml.
4. After that, ethane vapor was filled to the fluid supply system controlled by the first valve. The pressure of ethane vapor in this system was the same as the pressure of ethane vapor in the storage tank.
5. The next step was to pressurize air in the high-pressure chamber to the pressure ethane will be in liquid phase: typically 2 bar higher than the phase boundary between liquid and gaseous phase. For example, the pressure at an equilibrium between gas and liquid phase at 23°C is about 40 bar. Air in the high-pressure chamber in this case needs to be pressurized at least 42 bar. In this step, the pressure was increased with a flow rate in the range of 0.025-0.100 g/s following the pressure control method in Section 3.2.4.
6. After that air in the test chamber had been pressurized to the desired pressure for measurements, ethane vapor in the fluid supply system was then pressurized to a pressure greater than air pressure contained in the test chamber. In the pressurization step, the plunger was pushed to reduce the volume and pressurize ethane until a pressure higher than the air pressure around 0.3-0.7 bar. For example, when the pressure of air is 42 bar, ethane was pressurized to the pressure of 42.5 bar. In this process, all ethane vapor in the fluid supply system was assumed to be converted in liquid before injecting to the injection system.

7. For the liquid injection process, the second valve was opened to inject liquid ethane to the droplet generator. It was injected at a volume flow rate of 5 ml/min.
8. After that, the liquid in the syringe was evacuated, then the second valve was closed. A plunger of syringe was pulled back to get 24 ml of volume again and the first valve was opened to refill the fluid supply system with ethane.
9. Steps 6-8 were repeated again in order to fill the droplet generator and pipeline with liquid. This step was repeated until liquid ethane came out from droplet generator. After liquid ethane droplets came out, the optical rainbow measurements were performed.

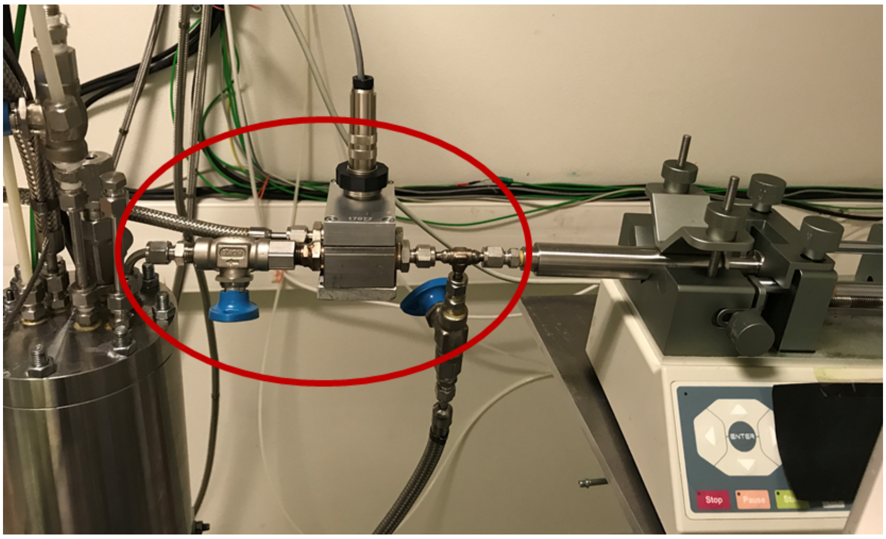

Figure 4.3: Schematic diagram of a fluid supply system

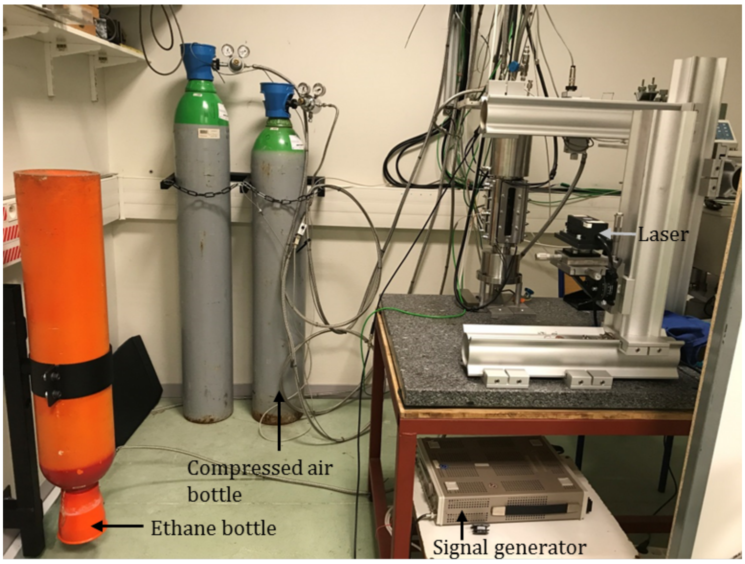

Figure 4.4: Experiment setup

4.2.2 The optical measurement on free-falling ethane droplets

This section describes the optical measurement method on ethane droplets under high-pressure up to 46 bar. The optical setup for measurements of light scattering around ethane rainbow angle was modified from the setup used for water and ethanol. The new setup allows us to observe light scattering around ethane rainbow angle for the thermodynamic conditions selected in this study. The side-view of a schematic diagram of light path and the setup for this optical measurement are shown in Figure 4.5. The light was emitted from the 0.532 μm 200 mW green laser and passed through the optical window to enter through the high-pressure test chamber. Then it passed through ethane droplets. After that, the scattered light came back outside the test chamber and traveled toward the screen. This situation is a particular case of the optical measurement presented in Section 3.2.6. The optical measurement method for liquid ethane is the same as the one used for water and ethanol. Though, the ethane droplets measurements were performed in series at the same thermodynamical conditions (typically 2-3 measurements).

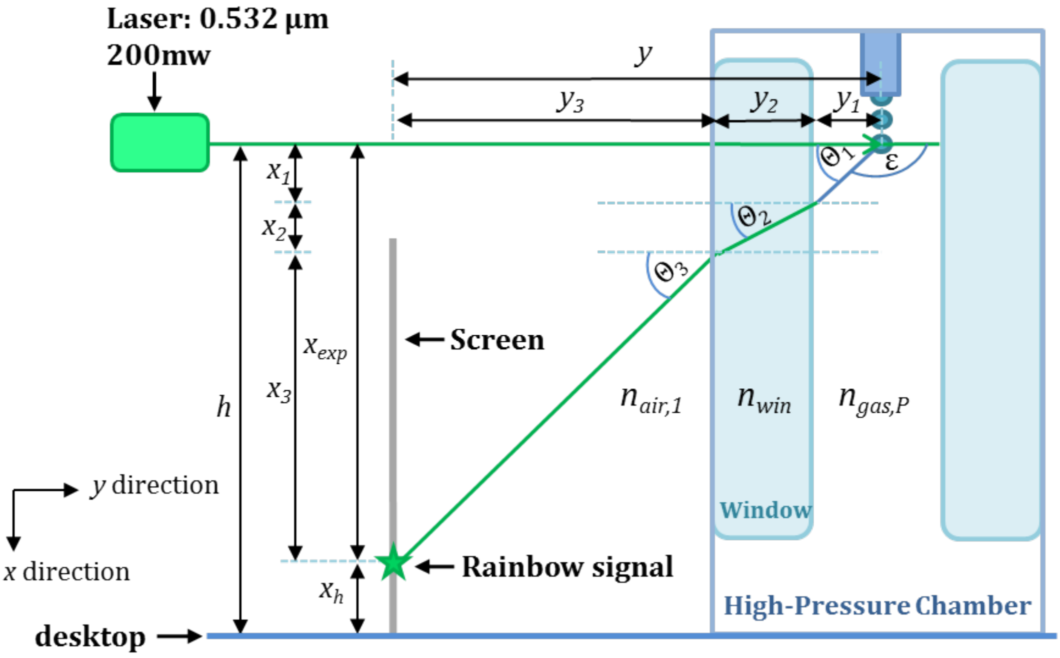

Figure 4.5: Side-view of the schematic diagram of light path through ethane droplets and scattered at the rainbow angle

4.3 Analysis of the results from the optical measurements on ethane droplets

4.3.1 Determination of the absolute refractive index of ethane droplets during the first injection

As in Chapter 3, the absolute refractive index can be determined from the positions of rainbow signal's bright patterns observed from experiments. The positions of bright patterns were firstly used to define their angular positions. After that, the rainbow signals were simulated based on Debye theory (p=2). The peak positions of these rainbow signals were then fitted to the angular positions of the bright patterns. The signal providing the best-fit peak positions was used to determine the average relative refractive index and the average droplet size of ethane droplets from experiments. During the first injection of ethane inside the test chamber, the gas inside the test chamber was assumed to be pure air. Therefore, the absolute refractive index was finally determined from the relative refractive index and refractive index of air under high pressure.

4.3.2 Determination of the absolute refractive index of gas in chamber after the first injection

When we performed measurements on ethane droplets, the rainbow locations change after each injection of liquid ethane inside the test chamber. When the absolute refractive index of liquid ethane in the second and third injections are deduced with the same procedure as the one used for water (gas in chamber is only air), the value of absolute refractive indices of liquid ethane are different. One reason explaining this result is that now, the thermodynamic conditions of injection of ethane are close to conditions in which the evaporation of ethane into the test chamber cannot be neglected. Performing successive experiments of injection of liquid ethane into the test chamber without purging the test chamber modifies the species composition of the gas surrounding droplets. During the first injection of ethane, the gas is assumed to be pure air whereas for the second and the third injection a mixture of air with vapor ethane will be present. Modification of the refractive index of the gaseous phase may then change the data processing of the rainbow measurements. In the next sections, the method of the determination of the relative refractive index of ethane droplets ($n'_{ethane,P}$) and absolute refractive index of gas phase after the first injection ($n_{gas,P}$) are now detailed.

4.3.2.1 Calculation of an angular position of rainbow signal's peak position

For the calculation of the peak angular position, the calculation is the same as the one used for water (3.3.3) excepted that the change on the refractive index of gas surrounding droplets must be taken into account according to the mixing of air with evaporated ethane. As the refractive index of the gas phase is an unknown value, we firstly generate possible values of refractive index of gas. The refractive indices of gas in the test chamber (n_{gas,l_a}) were from 1.0001 to 1.0800 where $l_a = 1$ to 800. The generated values were increased by 0.0001. After that, the angular positions of rainbow signal's peaks for each of n_{gas,l_a} were computed using the same calculation presented in Section 3.3.3 (use n_{gas,l_a} instead of $n_{air,P}$ for a calculation). Finally, the angular position of the rainbow signal's peak for each value of n_{gas,l_a} was obtained and this one was defined as $\varepsilon_{l_a,match}$. Examples of these results follow:
l_a=1, $n_{gas,1}$=1.0001; $\varepsilon_{1,match}$ corresponding to x_{exp} was derived
l_a=2, $n_{gas,2}$=1.0002; $\varepsilon_{2,match}$ corresponding to x_{exp} was derived
l_a=3, $n_{gas,3}$=1.0003; $\varepsilon_{3,match}$ corresponding to x_{exp} was derived
.
.
.
k=800, $n_{gas,800}$=1.0800; $\varepsilon_{800,match}$ corresponding to x_{exp} was derived .

Note that the first peak and second peak were used for measurements on ethane droplets.

4.3.2.2 Determination of absolute refractive index of gas in the test chamber

This section describes a method to determine the absolute refractive index of gas in the test chamber after the first injection of liquid ethane. In this step, the angular positions of rainbow's peaks for each computed n_{gas,l_a} determined in Section 4.3.2.1 will be compared with those deduced from simulated rainbow signals. The values providing the best-fit peak's positions will be used to determine the average relative refractive index of ethane droplets and the absolute refractive index of gas. In this simulation, there are two fixed parameters corresponding to n_{gas,l_a}: the wavelength of the incident light illuminating ethane droplets (λ_{c,l_a}) and the relative refractive index of liquid droplet (n'_{ethane,l_a}). The droplet size is a parameter to be varied to find the best-fit peak positions for each n_{gas,l_a}. The wavelength (λ_{c,l_a}) corresponding to n_{gas,l_a} is calculated from the following equation:

$$\lambda_{c,l_a} = \frac{0.532\mu m}{n_{gas,l_a}}. \tag{4.1}$$

The absolute refractive index of ethane was initially assumed to be the one measured at the first injection when measurements were performed in the same thermodynamic conditions. Accordingly, the relative refractive index (n'_{ethane,l_a}) for the simulation corresponding to each n_{gas,l_a} are calculated from:

$$n'_{ethane,l_a} = \frac{n_{ethane,P}}{n_{gas,l_a}}. \tag{4.2}$$

For the last parameter, sizes of droplets (d_{l_a,l_b}) for simulation were generated from 101 to 250 μm increasing by 1 μm. The value l_a is connected to the number of generated absolute refractive indices of gas. The value l is connected to the number of generated sizes where $l_b = 1$ to 150. After the parameters (n'_{ethane,l_a},λ_{c,l_a} and d_{l_a,l_b}) were defined, the rainbow signals for the fitting procedure were simulated. The fitting of the angular positions ($\varepsilon_{l_a,match}$) to the peak positions of the simulated rainbow signals were performed for each n_{gas,l_a}. After the fitting, the size producing best fitting-positions ($d_{l_a,fit}$) and the associated error ($err_{l_a,fit}$) were obtained for each n_{gas,l_a}. Examples of these results are as follows:
l_a=1, $n_{gas,1}$=1.0001; $n'_{ethane,1}$, $\lambda_{c,1}$ and $d_{1,fit}$ produced the best-fit signal to $\varepsilon_{1,match}$ with $err_{1,fit}$ was obtained,
l_a=2, $n_{gas,2}$=1.0002; $n'_{ethane,2}$, $\lambda_{c,2}$ and $d_{2,fit}$ produced the best-fit signal to $\varepsilon_{2,match}$ with $err_{2,fit}$ was obtained,
l_a=3, $n_{gas,3}$=1.0003; $n'_{ethane,3}$, $\lambda_{c,3}$ and $d_{3,fit}$ produced the best-fit signal to $\varepsilon_{3,match}$ with $err_{3,fit}$ was obtained,

.

.

.

l_a=800, $n_{gas,800} = 1.0800$; $n'_{ethane,800}$, $\lambda_{c,800}$, $d_{800,fit}$ produced the best-fit signal to $\varepsilon_{800,match}$ with $err_{800,fit}$ was obtained.

Errors from the best-fit signal for each n_{gas,l_a} were then compared to find the signal providing the smallest error ($err_{l_{a-min},fit}$). The $d_{l_{a-min},fit}$ and $n'_{ethane,l_{a-min}}$ providing the minimal value of error were assumed to be the average size and the average relative refractive index of ethane droplets. The $n_{gas,l_{a-min}}$ corresponding to $d_{l_{a-min},fit}$ and $n'_{ethane,l_{a-min}}$ was assumed to be the absolute refractive index of gas. Finally, the relative refractive index of liquid ethane ($n'_{ethane,P}$), the absolute refractive index of gas during measurement ($n_{gas,P}$) and the average droplet size (d) are estimated from the values providing the minimum error in the fitting procedure.

4.3.2.3 Estimation of the concentration of ethane vapor from optical measurement

This section details the method used to estimate the ethane vapor concentration in the gas surrounding ethane droplets. According to the previous section, the absolute refractive index of gas in the test chamber ($n_{gas,P}$) and relative refractive index of ethane droplet ($n'_{ethane,P}$) after the first injection were determined by using absolute refractive index of ethane droplet ($n_{ethane,P}$) from the first injection. Knowing absolute refractive index of gas ($n_{gas,P}$), the concentration of ethane vapor in the test chamber (x) can be estimated from:

$$n_{gas,P} = x n_{ethane-vapor,P} + (1-x) n_{air,P}. \tag{4.3}$$

Note that the estimation of the absolute refractive index of ethane vapor ($n_{ethane-vapor,P}$) is provided in Appendix B and $n_{air,P}$ is provided in Section 3.3.1. Finally, the percentage of ethane vapor concentration (x) after the first injection is estimated.

4.3.2.4 Estimation of the concentration of ethane vapor from the amount of injected ethane

Alternatively, the concentration of vapor ethane can be estimated directly from the volume of injected liquid ethane, the volume of the chamber, the pressure and the temperature. For this estimation, the volume of the test chamber was calculated only from the main housing dimensions. It is approximately 410 ml. In this work, the mass of gas can be estimated from an ideal gas law written as

$$PV = nRT, \tag{4.4}$$

where P is the pressure of the gas in Pascal, V is the volume of gas in cubic meters, n is the amount of substance in moles, R is the ideal gas constant and T is the temperature of gas in Kelvin. R has the value of 8.3144598 J/(K·mol). The amount of substance (n) is equal to the total mass of the gas (m_{gas}) in grams divided by the molar mass (M) in grams per mole:

$$n = \frac{m_{gas}}{M}. \tag{4.5}$$

The mass of air (m_{air}) and mass of ethane vapor (m_{ethane}) before an injection of liquid ethane under high-pressure, can be estimated from Equation 4.4 and 4.5. After liquid ethane was injected into the test chamber, we estimated the concentration of ethane vapor for the case of full evaporation. For example, the mixture measured in the second injection was assumed to be air and evaporated ethane that was injected during first injection. The mole of air in chamber was calculated from the volume of 410 ml. The volume of syringe for one injection used in this calculation is 24 ml. In the same way, the concentration of ethane vapor for the third injection was estimated from liquid ethane injected from the first and the second injections. Finally, the ethane vapor concentration from this basic estimation was obtained and it was compared with the concentration estimated from the optical measurements.

4.4 Experimental results

4.4.1 The study of the production of liquid ethane

Generating liquid ethane is one of the most important step in this study. Since the ethane in the tank is originally in a vapor phase, we need to pressurize it to convert it into liquid. In this work, the procedure to produce liquid had been studied and it was presented in Section 4.2.1. In comparison with water and ethanol experiments, the experimental setup had been modified to optimize the production of liquid ethane. For that, the volume of fluid supply system was minimized to reach higher pressure. This process transforms ethane vapor to liquid faster. An example of the transition of gaseous phase to liquid phase is shown in Figure 4.6. The blue triangle represents the state of ethane in a bottle at pressure of 39 bar for a temperature equal to 23°C. The orange triangle represents an injected liquid ethane for measurements at pressure of 42 bar and at temperature of 23°C. In this example, ethane vapor was pressurized to cross the line of equilibrium between liquid and gas and then it reached pressure of 42 bar, a state in the liquid phase. As seen in Figure 4.6, the orange triangle is in the liquid phase above the phase change between liquid and gas. After ethane was pressurized in the liquid phase, it has been injected. Moreover, the red circle shows an area of the thermodynamic conditions for experiments. These experiments were performed at temperature of 19-25°C and at pressure of 40-46 bar. The gray triangle shows the state of liquid ethane in an experiment at the highest pressure reached in this work.

The jet of liquid ethane was presented in Figure 4.7(a) and Figure 4.7(b). Liquid ethane in these two images was produced at volume flow rate of 5 ml/min under pressure of 40 bar and temperature of 20°C. Figure 4.7(a) shows injected liquid ethane and Figure 4.7(b) shows injected liquid ethane and the position of laser illuminated at 1 cm from the exit of injector at the same condition. The spray part can be visualized in a red circle in Figure 4.7(b). The volume flow rate fixed to inject liquid ethane in this study was 5 ml/min while it was set as 1.2-2.2 ml/min for the case of liquid water and liquid ethanol injection. In this case, ethane droplet size was not calculated based on the Rayleigh breakup of laminar fluid jets. It was determined by the analysis of results from rainbow measurements. Apart from that, the minimum pressure selected to pressurize ethane in our procedure is around 2 bar greater than the phase change between liquid and gas at a given temperature. If the value is less than this one, we cannot create droplets in the range of 100-200 μm as seen in Figure 4.7(c). In this case, the rainbow signal does not occur, however, a scattered light is still visible as presented in a red circle in Figure 4.8. Figure 4.9 shows the rainbow signal of ethane droplets produced at pressure higher than the equilibrium curve around 2 bar. Finally, the condition and procedure to produce ethane droplets for the optical measurements has been studied.

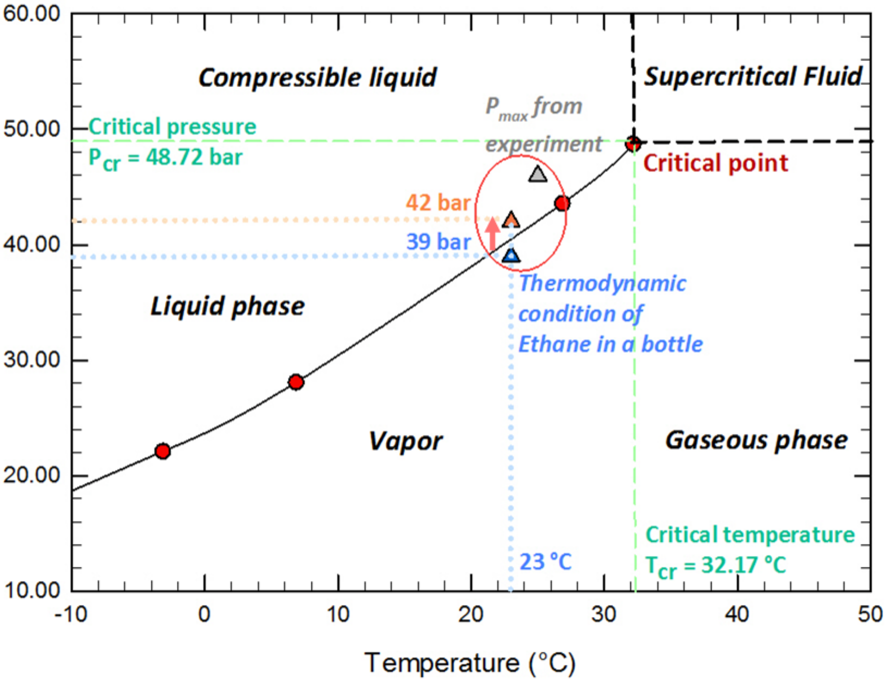

Figure 4.6: The status of ethane for the measurements in this work on pressure-temperature diagram

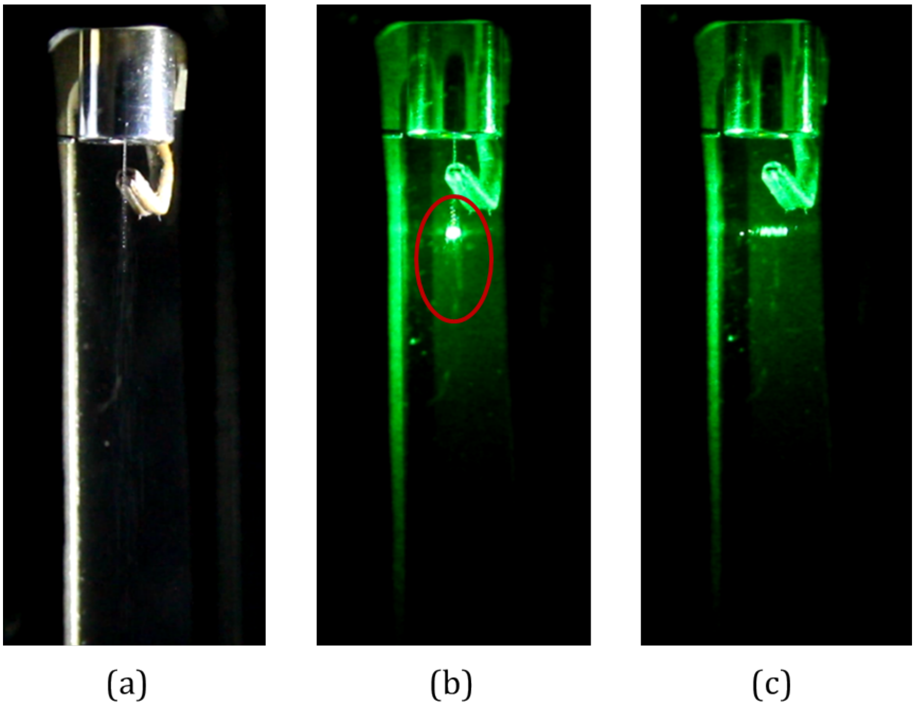

Figure 4.7: Visualization of ethane droplets generated in elevated pressures

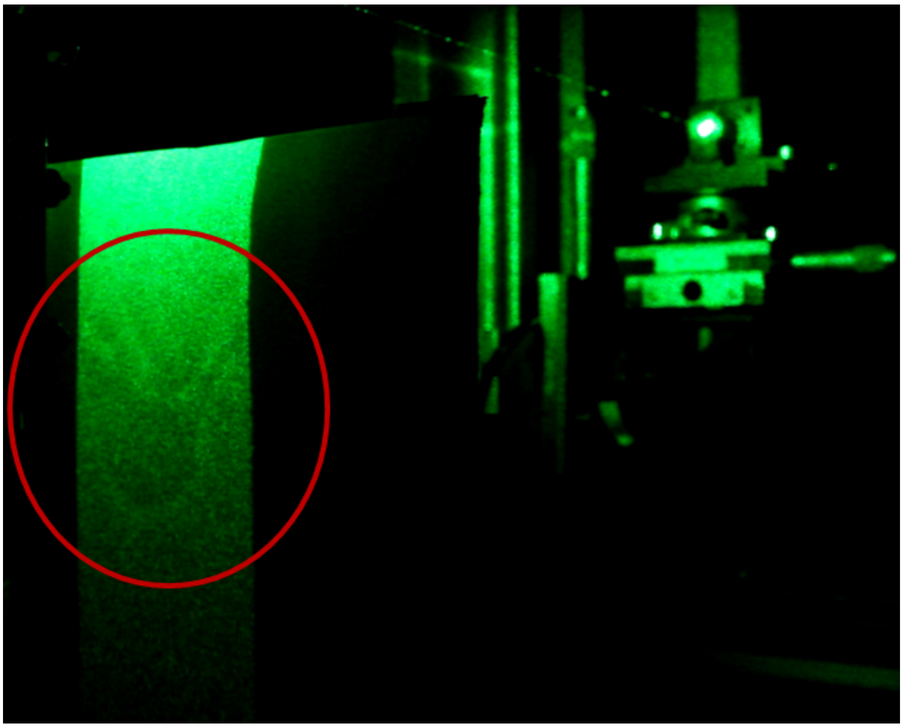

Figure 4.8: Scattered light produced from the illumination of ethane with the green laser beam

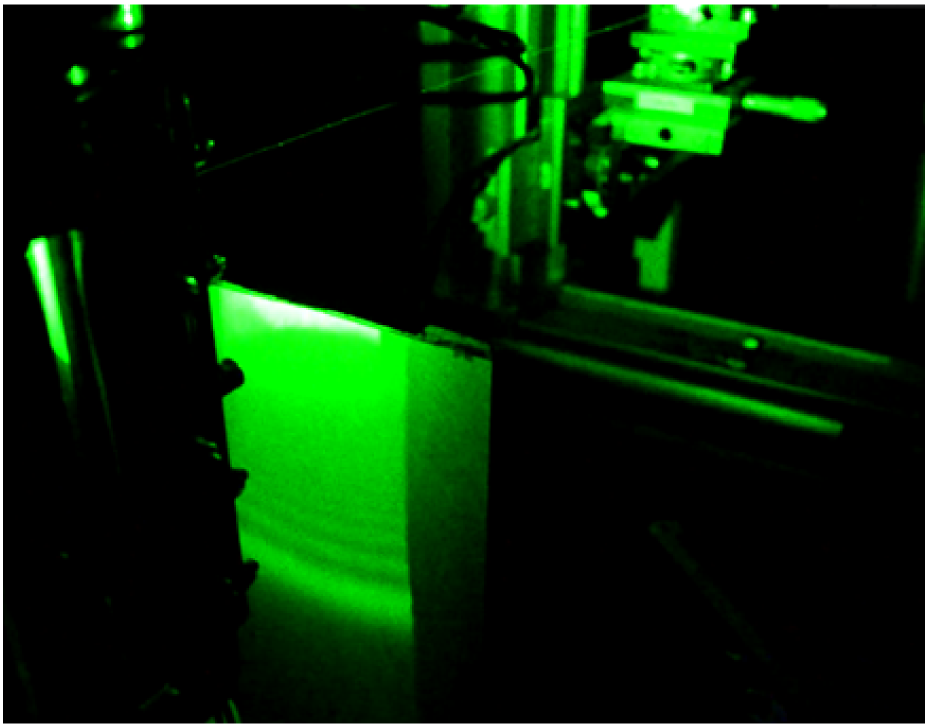

Figure 4.9: Rainbow signal from ethane droplets

4.4.2 Result of the observation of rainbow signals from ethane droplet

The optical set up used to measure the rainbows of ethane droplets is presented in Figure 4.10. For each pressure, experiments were performed in series. For example, the free-falling ethane droplets have been successively measured at pressure around 42 bar and temperature of 23°C 3 times. In the experiments, ethane vapor was pressurized from pressure around 39 bar to 42 bar in order to transform ethane vapor into liquid. The ethane droplets are created after liquid ethane was filled into all parts of the liquid system and the droplet generator. We firstly observe a rainbow signal during the first injection. For the second and third injections, liquid ethane was injected without purging the test chamber chamber. The rainbow signal measured in the second injection shifted down from the result from the first injection as presented in Figure 4.11. Furthermore, the rainbow signal observed from the third injection shifted down from result of measurements in the second injection as well.

Figure 4.12 shows the state of liquid water, ethanol and ethane produced in this work and line of equilibrium of water and ethane in the pressure-temperature phase diagram. The state of injected liquid ethane represented as the black triangle down is close to its critical point (green star). Whereas, the state of water and ethanol from our measurement is represented by a gray triangle up. They are far from the critical point of water and ethanol (blue star and yellow star, respectively) compared to those for ethane. Since the heat of vaporization of a substance will be very small when the thermodynamic conditions are close to the critical point, the evaporation rate of injected droplets was assumed to be high in case of ethane droplets measurements. For this reason, we assumed that the shifting of the rainbow signal after the first injection is related the mixture of air and evaporated ethane. Therefore, the refractive index of the gas surrounding droplets depends on the concentration of ethane in the gaseous mixture.

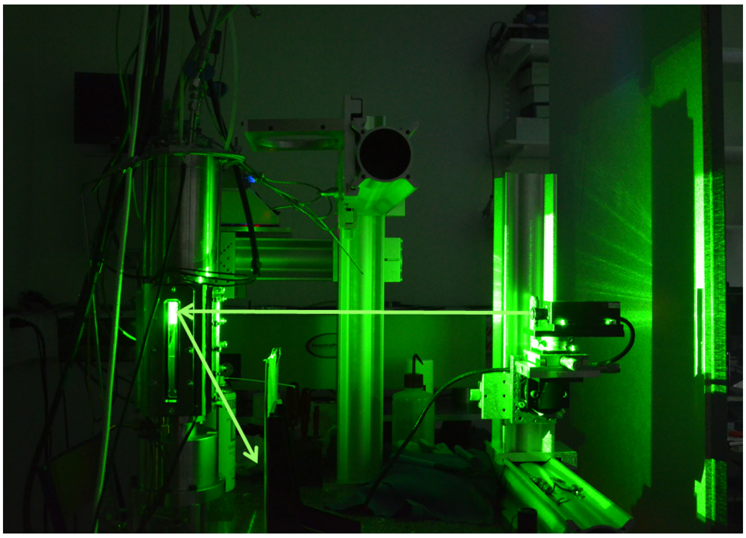

Figure 4.10: Image of the experiment setup used rainbow measurements of free-falling ethane droplets

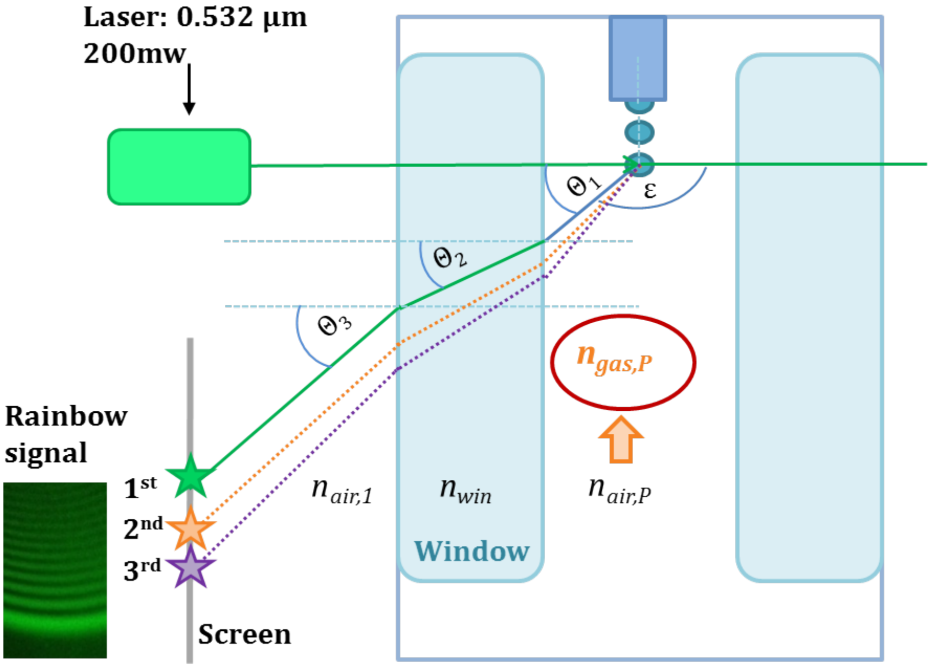

Figure 4.11: Schematic diagram of the shift of the rainbow signal after the first injection of liquid ethane

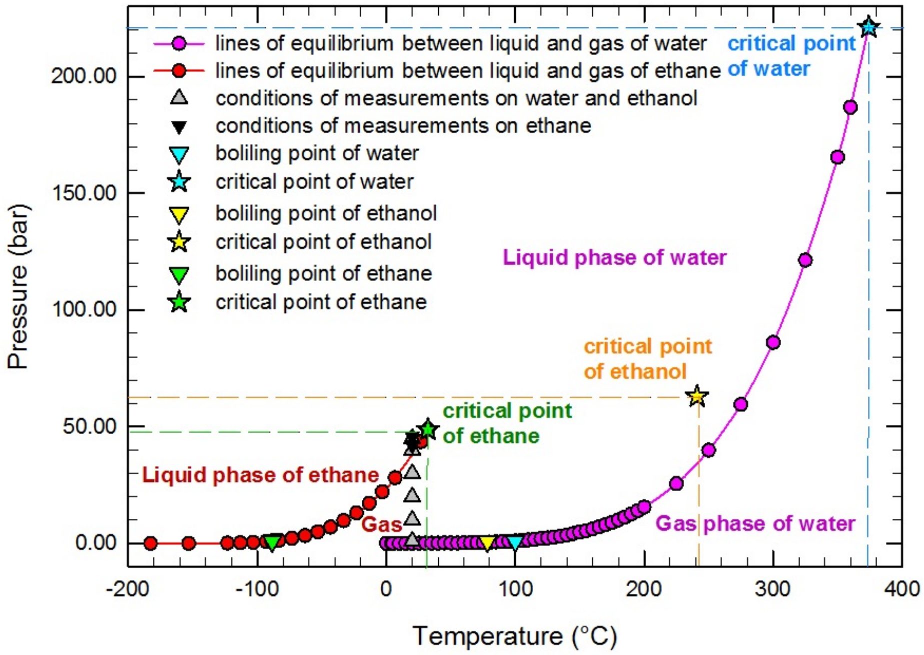

Figure 4.12: The line of equilibrium between liquid and gas of water and ethane and the status of the measurements on water, ethanol and ethane droplets on the pressure-temperature phase diagram

4.4.3 Results of refractive index measurements

For the first injection's measurement, the series of measurement of May 23rd, 2017, the absolute refractive index of free-falling ethane droplets was determined to be 1.2545 ± 0.002. This value was assumed to be the absolute refractive index value for the second and third injections as well. The relative refractive index of ethane droplets and the absolute refractive index of gas for the second and third injections were then determined. Results of the optical measurements on May 23rd, 2017 are shown in Table 4.1. We found that the absolute refractive index of the gas mixture increased with the number of injections. In addition, the average size of ethane droplets were determined from the optical measurements and they are in the range of 120-150 μm as seen in Table 4.1.

After that, the absolute refractive index of gas in the test chamber was obtained, the concentration of ethane vapor in the test chamber for each measurement was estimated. The concentration of ethane vapor for the different injections for measurements of May 19 and 23, 2017 are shown in Table 4.2. For the second injection, we assumed that ethane vapor in the test chamber comes only from the first injection. In the same way, for the third measurement, we assumed that ethane vapor in the test chamber comes from the first and second injections. Figure 4.13 shows the absolute refractive index of gas versus the number of injections of ethane. According to this graph, the absolute refractive index of the gas mixture increases with the number of injection of ethane. Moreover, the increase of absolute refractive index of the gas mixture appears to be mainly linear. For each point, it was indicated the estimated percentage of ethane vapor in a gas mixture. The percentage of ethane vapor after the first injection of the measurement at pressure of 42 bar on May 23, 2017 is about 7.4%. After the second injection, it is about 15.2%: two times the quantity after the first injection. The percentage of ethane vapor of the second and third measurements at 41 bar on May 19, 2017 are 4.3 % and 9.5%, respectively. The concentration of the third measurement is also a double value of the second measurement.

Furthermore, the quantity of ethane vapor in the gas phase can be estimated from the injected liquid ethane as well. For this study, the computed mass of liquid ethane during each injection is 1.15 grams (equal to 0.038 mole). The concentration of ethane vapor estimated from the injection are presented in Table 4.3. According to the estimation, after the first injection, we must obtained about 5% of ethane vapor in a gas mixture. After the second injection, it is about 10% of ethane vapor in a gas mixture. The concentration of ethane vapor estimated from the rainbow measurement and the injection have the same trend, i.e. an increase with the number of injections of liquid ethane.

Lastly, we presented the relative and absolute refractive indices of ethane determined in Figure 4.14. This graph shows that the increase of concentration of ethane vapor in a gas mixture is in agreement with a change of the relative refractive index deduced from the rainbow measurement.

Table 4.1: Measurement data and results from the rainbow signal fitting process from an experiment performed on May 23rd, 2017

Injection	P_{inside} (bar)	T_{inside} (°C)	λ_c (μm)	$d_{fitting}$ (μm)	$n_{air,P}$	n_{rela}	$n_{gas,P}$	n_{abs}
1st	42.50	22.00	0.52591	140	1.0115768	1.2404	1.0116	1.2548
2nd	42.44	22.20	0.52424	124	1.0115514	1.2365	1.0148	1.2548
3rd	42.43	22.50	0.52259	123	1.0115354	1.2324	1.0182	1.2548

Table 4.2: Percentage of the estimated concentration of gaseous mixture from experiments

Date	Injection	P_{inside} (bar)	T_{inside} (°C)	Concentration of gas (% by mole) ethane	air
19/05/2017	1st	41.29	21.7	0	100
	2nd	41.26	21.6	4.3	95.7
	3rd	41.13	21.6	9.5	90.5
	4th	41.29	21.6	10.3	89.7
23/05/2017	1st	42.50	22.20	0	100
	2nd	42.44	22.50	7.4	92.6
	3rd	42.43	22.50	15.2	84.8

Table 4.3: The percentage of estimated concentration of ethane vapor from an injected ethane

Date	Injection	P_{inside} (bar)	T_{inside} (°C)	Concentration of ethane vapor (% by mole) estimated for 100% evaporation
19/05/2017	1st	41.29	21.7	0
	2nd	41.26	21.6	5.3
	3rd	41.13	21.6	10.3
	4th	41.29	21.6	15.1
23/05/2017	1st	42.50	22.20	0
	2nd	42.44	22.50	5.1
	3rd	42.43	22.50	10.6

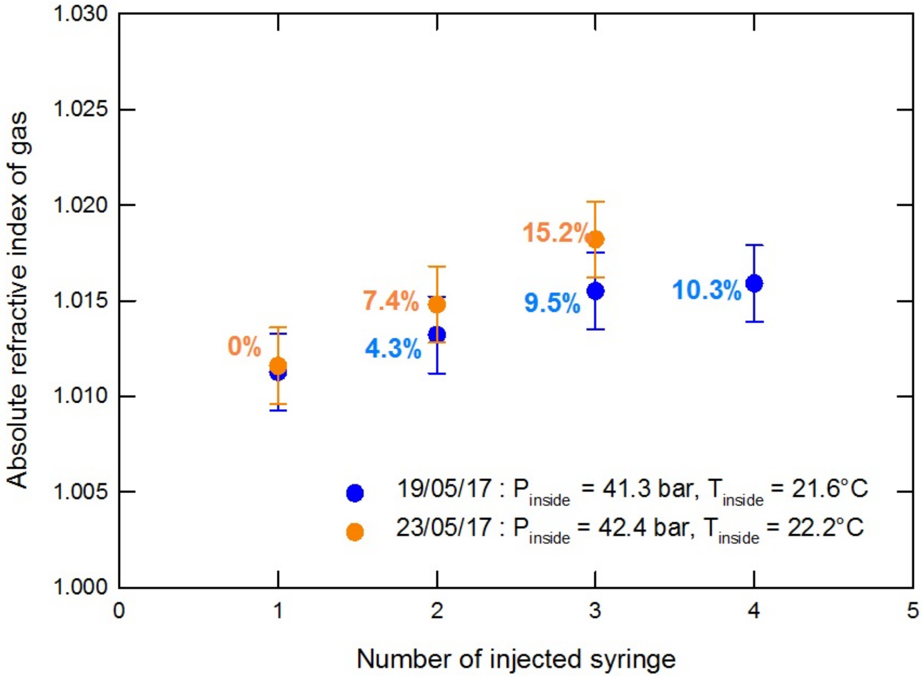

Figure 4.13: The refractive index of gas in chamber measured versus the number of injected syringe and the percentage of the ethane vapor concentration indicated on the plots

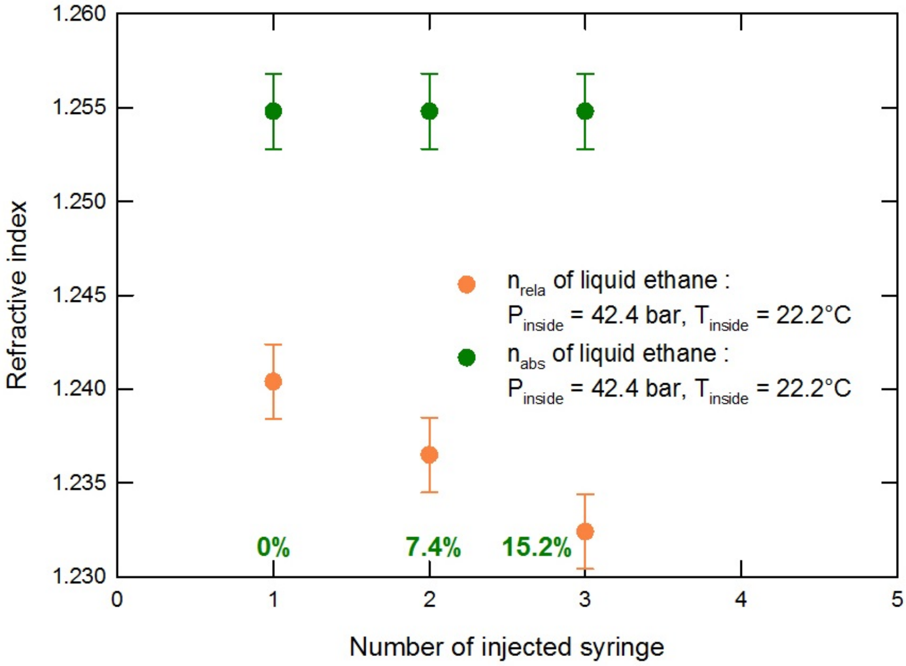

Figure 4.14: Absolute and relative refractive index of liquid ethane droplets results number of times of injection of liquid ethane and the estimated percentage of ethane vapor in a gas mixture from the experiment on May 23rd, 2017

4.5 Conclusions

A study of free-falling ethane droplets at pressure of 40-46 bar and temperature 18-25°C close to critical point was performed. Liquid ethane was produced by the pressurization of ethane vapor of 36-41 bar, depending on temperature, to reach a pressure greater than the phase change between gas and liquid. An adapted global rainbow refractometry was the technique used for measurements of physical properties of free-falling ethane droplets under sub-critical conditions. For each measurement, the absolute refractive index of liquid ethane are determined from measurements during the first injection of liquid ethane. The absolute refractive index of ethane droplets measured at pressure of 42.50 bar and temperature of 22°C is equal to 1.255 ± 0.002 (measurement on May 23rd, 2017). For the second and third series of measurements at the same thermodynamic conditions to the first injection, the absolute refractive indices of ethane droplets were assumed to be the same as the one measured during the first injection. The relative refractive index of ethane droplets and absolute refractive index of gas are determined from the rainbow measurement as well. In the measurements after the first injection of liquid ethane, the relative refractive index of ethane droplets decreases with the number of injections of liquid ethane because the refractive index of gaseous mixture surrounding droplets increases.

The estimated refractive index of gaseous mixture can be used to estimate the concentration of ethane vapor in gas mixture. The percentage of the concentration of ethane vapor increases with the number of injections of liquid ethane. This increase is essentially linear. Furthermore, the concentration of ethane vapor was estimated directly from the quantity of the injected liquid ethane by assuming that this one is fully evaporated. The results estimated from optical measurements were compared to those from the injected liquid ethane. A same trend with the number of injections is found.

In conclusion, to measure absolute refractive index of liquid ethane in high pressure, the change of the refractive index of the gaseous mixture surrounding the droplets must be taken into account due to the strong evaporation of ethane vapor. The absolute refractive index and size of free-falling ethane droplets under sub-critical condition finally determined. Moreover, the absolute refractive index of the gaseous mixture into the test chamber are also estimated. Further study must be done in the future to enable an optical method able to measure simultaneously the refractive index of gaseous mixture surrounding droplets as well as the refractive index of liquid fuel in order to measure accurately the properties of droplets when the fuel is in a situation in which high evaporation rate is noted.

CHAPTER 5

Conclusions

In this study, the relative and absolute refractive index of water and ethanol have been measured on free-falling droplets under pressure up to 45 bar by using an adapted global rainbow technique. As a function of pressure and temperature, the refractive index of water at temperature of 50°C and pressure of 1 and 10 bar have been measured as well. The experimental absolute refractive index on free-falling water droplets are in agreement with data issued from literature for the measurement of water in cell. These results confirmed the reliability of the experimental methodology developed in this work and proved that we are able to measure the absolute refractive index of free-falling droplets as a function of pressure and temperature.

For measurements near the critical point, ethane was selected because its critical point is 48.7 bar and 32.2°C. Refractive index measurement on ethane droplets has been carried out at pressure in the range of 40-46 bar and temperature of 18-25°C. A measurement of the absolute refractive index of ethane droplets gives a value of 1.255 ±0.002 at pressure of 42.50 bar and temperature of 22°C.

CHAPTER 6

Future work

6.1 Future work

For the measurement of absolute refractive index of liquid ethane near the critical point, the change of the refractive index of the gas surrounding droplets must be taken into account due to the strong evaporation of ethane droplets. Therefore, in the real combustion device, we need also to measure simultaneously the refractive index of gaseous mixture and refractive index of liquid in the same time. We propose an optical measurement methodology to measure n_{gas} by measuring the transmission of the light inside the chamber. A schematic diagram of the optical setup for this measurement is shown in Figure 6.1. In this method, the intensity of light passing through the test chamber (I_2) and the intensity of light traveling directly to power meter (I_1) will be measured. Due to the change of n_{gas} the transmitted light will not be the same. Then the change of I_2/I_1 can be measured when the species composition of gas inside the chamber changes. We will estimate the percentage of intensity change due to n_{gas} from our measurement to predict the result. It is shown in Table 6.1.

Table 6.1: The percentage of intensity change estimated from n_{gas} obtained from the measurement in this work

Date	Injection	P_{inside} (bar)	n_{gas}	Transmitted light (%)	Change of transmitted light (%)
19/05/2017	1st	41.29	1.0003	86.72	
	2nd	41.26	1.0113	87.07	0.35
	3rd	41.13	1.0131	87.12	0.06
	4th	41.29	1.0153	87.19	0.07
	4th	41.29	1.0157	87.20	0.01
23/05/2017	1st	42.50	1.0003	86.72	
	1st	42.50	1.0116	87.08	0.36
	2nd	42.44	1.0146	87.17	0.09
	3rd	42.43	1.0180	87.27	0.10

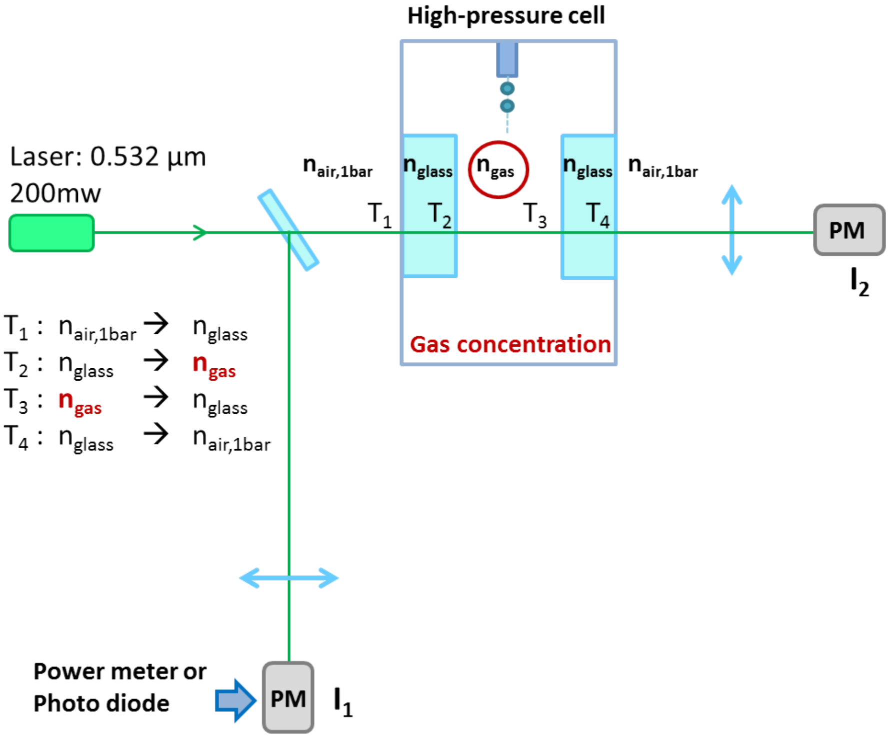

Figure 6.1: The predicted global rainbow pattern of ethane droplet when the thermodynamics condition is approaching to critical point

6.2 Perspectives

According to this study, we are now able to inject droplets of ethane and to measure absolute refractive index of liquid ethane not so far of the critical point. The next step of measurements will be to change slowly the temperature to approach as close as possible the critical point. The physical characteristics of ethane approaching the critical state will be then possible to analyze.

APPENDIX A

Calculation of the diameter of monodisperse droplets

A.1 Introduction

Monodisperse droplets generating is an important process for the study of droplet characteristic. According to monodisperse spray technology, it allows specific monodisperse sprays with adjustable droplet diameters to be generated. The formation of this droplet is based on the Rayleigh decay of multi-layered liquid jets. For this process, the monodisperse droplet of known size is produced by introducing vibratory disturbances in liquid jets. The calculation of droplet size is shown in this appendix [31].

A.1.1 Theoretical basics for calculation of diameter of monodisperse droplet

Base on the Rayleigh breakup of laminar fluid jets, a jet decays into droplet as stable criteria when the wavelength of deformation on the jet surface is bigger than the circumference of the jet;

$$\lambda = \frac{u_D}{f_G} \geq \pi D \tag{A.1}$$

where λ is wavelength, u_D is jet velocity, f_G is excitation frequency and D is a pinhole diameter. In order to generate droplets which are the same size and predictable diameter by using excitation wave to influence the fluid jet, the dimensionless wavelength ($k = \frac{\pi D}{\lambda}$) is located between $0.3 \leq k \leq 0.9$.

$$k = \frac{\pi D f_G}{u_D}, \tag{A.2}$$

where k is dimensionless wavelength. From Equation A.2, the frequency range which can be used to create monodisperse droplets is determined and shown below;

$$\frac{0.3 u_D}{\pi D} \leq f_G \leq \frac{0.9 u_D}{\pi D} \tag{A.3}$$

where D is a selected pinhole size in μm. The jet velocity (u_D) can be calculated from this equation;

$$u_D = \frac{\dot{V}}{A}, \tag{A.4}$$

where $\dot{V}$ is volume flow rate and A is a cross section area. The cross section area can be calculated from following equation;

$$A = \frac{\pi D^2}{4}. \tag{A.5}$$

To calculate u_D, $\dot{V}$ is obtained from the fitting of 2^{nd} order polynomial function between the volume flow rate and pinhole droplet size provided by TSI Incorporated [34]. This relation is shown as

$$\dot{V} = 2.1974 \times 10^4 D^2 - 5.863 \times 10^4 D + 0.0617, \tag{A.6}$$

where $\dot{V}$ is in the unit of cm^3/min. Finally, range of excitation frequency can be determined. To calculate a diameter of monodisperse droplets (d), the following equation is used;

$$d = \left(\frac{3u_D D^2}{2f_G}\right)^{1/3}. \tag{A.7}$$

A.1.2 Estimate droplet diameter size from pinhole diameter

To define the size of droplet, the pinhole diameter is selected first. According to Equation A.2 and A.7, the relation between droplet and pinhole diameter can be written in term of k as following equation;

$$d = D\left(\frac{3\pi}{2k}\right)^{1/3}. \tag{A.8}$$

As the limit of k is from 0.3 to 0.9, the range of pinhole diameter can be written in an equation below;

$$0.4d \leq D \leq 0.57d. \tag{A.9}$$

This range is used for selection pinhole diameter corresponding to chosen droplet diameter for experiment.

A.1.3 Determination of droplet size, and frequency value for monodisperse droplet generating

From theoretical basic calculation, volume flow rate, jet velocity, range of frequency and range of droplet diameter for different pinhole sizes are obtained. All of these parameters are shown in Table A.1. Volume flow rate and frequency are the parameters to be adjusted in an experiment. Table A.2 shows the range of frequency to be adjusted for different volume flow rates and pinhole diameter of 50, 75 and 100 μm. The volume flow rate is the main parameter to be adjusted under high pressure as the lower volume flow rate provides more stable rainbow signal.

Table A.1: Range of excited frequency and volume flow rate to produce monodisperse droplets corresponding to different pinhole sizes

D (μm)	A (cm^2)	$\dot{V}$ (ml/min)	$u_D = \dot{V}/A$ (cm/min)	Range of f_G (kHz)	Range of d (μm)
35	0.0000096	0.31	32268	$14.673 \leq f_G \leq 44.020$	$87.50 \geq d \geq 61.40$
50	0.0000196	0.58	29634	$9.433 \leq f_G \leq 28.299$	$125.00 \geq d \geq 87.72$
75	0.0000442	1.25	28384	$6.023 \leq f_G \leq 18.070$	$187.50 \geq d \geq 131.58$
100	0.0000785	2.20	28021	$4.460 \leq f_G \leq 13.379$	$250.00 \geq d \geq 175.44$

Table A.2: Range of excited frequency corresponding to volume flow rate to produce monodisperse droplets

D (μm)	$\dot{V}$ (ml/min)	Range of f_G (kHz)	Range of d (μm)
50	0.6	$9.727 \leq f_G \leq 29.181$	$125.22 \geq d \geq 86.82$
75	1.25	$6.004 \leq f_G \leq 18.013$	$187.83 \geq d \geq 130.23$
100	1.2	$2.432 \leq f_G \leq 7.295$	$250.44 \geq d \geq 173.65$
100	1.4	$2.837 \leq f_G \leq 8.511$	$250.44 \geq d \geq 173.65$
100	1.6	$3.242 \leq f_G \leq 9.727$	$250.44 \geq d \geq 173.65$
100	1.8	$3.648 \leq f_G \leq 10.943$	$250.44 \geq d \geq 173.65$
100	2.0	$4.053 \leq f_G \leq 12.159$	$250.44 \geq d \geq 173.65$
100	2.2	$4.458 \leq f_G \leq 13.374$	$250.44 \geq d \geq 173.65$

APPENDIX B

Effect of temperature and pressure on the refractive index of ethane gas from literature

B.1 Estimation of ethane gas refractive index from literature

In this work, we obtained the refractive index of ethane gas data from George et al., 1973 [10] in order to find the relation between refractive index of ethane and temperature at constant pressure. They presented the refractive refractive index of ethane measured at four temperature which are 37.94, 71.33 104.22 and 120.89°C and pressure from 6 to 103 bar. We considered the relation of temperature and refractive index of ethane at pressure of 41.37 and 48.26 bar. In this work, the curve fitting with the data from George et al., 1973 by using the rational function ($T = \frac{1+b_1 n_{632.8nm}}{b_2+b_3 n_{632.8nm}}$) had been carried out for these two pressures in order to find the correlation between refractive index of ethane and temperature. At pressure of 41.37 bar, the correlation from the curve fitting is as follow;

$$n_{632.8nm} = \frac{-0.04340347T - 1}{-0.906614 - 0.042939T}. \tag{B.1}$$

The correlation for the pressure of 48.26 bar is as follow:

$$n_{632.8nm} = \frac{-0.459242T - 1}{-0.196664 - 0.452482T}. \tag{B.2}$$

Finally, these correlations can be used to estimate refractive index of ethane gas for these two pressure at different temperatures. Figure B.1 shows the best fitting curve and data at pressure of 41.37 and 48.26 bar.

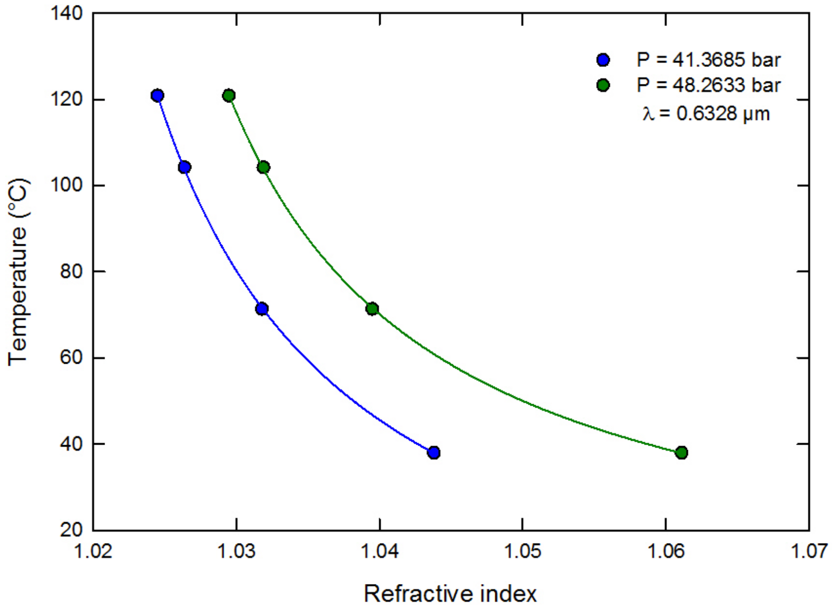

Figure B.1: Refractive index for ethane gas versus temperatures at the pressure of 41.3685 and 48.2633 bar from George et al., 1973 [10] and their best fitting curve

REFERENCES

[1] A typical phase diagram. `https://en.wikipedia.org/wiki/Phase_diagram`, August 2017. (Cited on pages ix & 4).

[2] Sven Horstmann. *Theoretische und experimentelle Untersuchungen zum Hochdruckphasengleichgewichtsverhalten fluider Stoffgemische fr die Erweiterung der PSRK-Gruppenbeitragszustandsgleichung [Theoretical and experimental investigations of the high-pressure phase equilibrium behavior of fluid mixtures for the expansion of the PSRK group contribution equation of state]*. PhD thesis, Carl-von-Ossietzky Universitt Oldenburg, July 2000. (Cited on pages ix & 4).

[3] Toshiharu Takagi and Hiroshi Teranishi. Refractive index of liquids under high pressure. *Journal of Chemical and Engineering Data*, 27(1):16–18, 1982. (Cited on pages ix, 5, 6 & 7).

[4] John A Adam. The mathematical physics of rainbows and glories. *Physics reports*, 356(4):229–365, 2002. (Cited on pages ix, 10 & 11).

[5] JPAJ Van Beeck. Rainbow phenomena: development of a laser-based, non-intrusive technique for measuring droplet size, temperature and velocity. *Technical University of Eidoven, The Netherlands*, 1997. (Cited on pages ix & 12).

[6] P Schiebener, Johannes Straub, JMH Levelt Sengers, and JS Gallagher. Refractive index of water and steam as function of wavelength, temperature and density. *Journal of physical and chemical reference data*, 19(3):677–717, 1990. (Cited on pages x, 20, 55 & 56).

[7] Joseph S Rosen. The refractive indices of alcohol, water, and their mixtures at high pressures. *JOSA*, 37(11):932–938, 1947. (Cited on pages x, 5, 21 & 22).

[8] CC Chen and K Vedam. Piezo-and elasto-optic properties of liquids under high pressure. iii. results on twelve more liquids. *The Journal of Chemical Physics*, 73(9):4577–4584, 1980. (Cited on pages x, 21 & 22).

[9] RJ Jiménez Riobóo, Martine Philipp, MA Ramos, and Jan-Kristian Krüger. Concentration and temperature dependence of the refractive index of ethanol-water mixtures: Influence of intermolecular interactions. *The European Physical Journal E*, 30(1):19, 2009. (Cited on pages x, xiii, 21 & 23).

[10] George J Besserer and Donald B Robinson. Refractive indexes of ethane, carbon dioxide, and isobutane. *Journal of Chemical and Engineering Data*, 18(2):137–140, 1973. (Cited on pages xii, 23, 91 & 92).

[11] Michael Wensing, Thomas Vogel, and Gudrun Götz. Transition of diesel spray to a supercritical state under engine conditions. *International Journal of Engine Research*, 17(1):108–119, 2016. (Cited on page 1).

[12] Anthony Clifford and Tony Clifford. *Fundamentals of supercritical fluids.* Oxford University Press, 1999. (Cited on page 3).

[13] Thos C Poulter, Carter Ritchey, and Carl A Benz. The effect of pressure on the index of refraction of paraffin oil and glycerine. *Physical Review*, 41(3):366, 1932. (Cited on page 5).

[14] RM Waxler and CE Weir. Effect of pressure and temperature on the refractive indices of benzene, carbon tetrachloride, and water. *Precision Meas. and Calibration*, 10(2):52–60, 1963. (Cited on page 5).

[15] RM Waxler, HW SCHAMP, and CE WEIR. Effect of pressure and temperature upon the optical dispersion of benzene, carbon tetrachloride and water. *JOURNAL OF RESEARCH OF THE NATIONAL BUREAU OF STANDARDS SECTION A-PHYSICS AND CHEMISTRY*, (5):489–498, 1964. (Cited on page 5).

[16] Everett M Stanley. Refractive index of pure water for wavelength of 6328 ang at high pressure and moderate temperatures. *Journal of Chemical & Engineering Data*, 16(4):454–457, 1971. (Cited on pages 5 & 6).

[17] Donglin Wang, Kun Yang, and Yin Zhou. Measuring refractive index and volume of liquid under high pressure with optical coherence tomography and light microscopy. *Applied optics*, 55(9):2435–2438, 2016. (Cited on pages 5 & 6).

[18] Frédéric Grisch and Mikaël Orain. Role of planar laser-induced fluorescence in combustion research. *AerospaceLab*, (1):p–1, 2009. (Cited on page 8).

[19] Gang Chen, Md Mohiuddin Mazumder, Richard K Chang, J Christian Swindal, and William P Acker. Laser diagnostics for droplet characterization: application of morphology dependent resonances. *Progress in energy and combustion science*, 22(2):163–188, 1996. (Cited on page 9).

[20] JPAJ Van Beeck, D Giannoulis, Laurent Zimmer, and ML Riethmuller. Global rainbow thermometry for droplet-temperature measurement. *Optics letters*, 24(23):1696–1698, 1999. (Cited on pages 9 & 13).

[21] H Moyes Nussenveig. *The theory of the rainbow.* WH Freeman, 1977. (Cited on page 9).

[22] Hendrik Christoffel Hulst and Hendrik C van de Hulst. *Light scattering by small particles*. Courier Corporation, 1957. (Cited on page 10).

[23] S Saengkaew. *Development of novel global rainbow technique for characterizing spray generated by ultrasonic nozzle*. PhD thesis, University of Chulalongkorn (Thailand) and Rouen (France), 2006. (Cited on pages 10, 12 & 13).

[24] N Roth, K Anders, and A Frohn. Simultaneous measurement of temperature and size of droplets in the micrometer range. *Journal of Laser Applications*, 2(1):37–42, 1990. (Cited on page 13).

[25] Norbert Roth, Klaus Anders, and Arnold Frohn. Refractive-index measurements for the correction of particle sizing methods. *Applied optics*, 30(33):4960–4965, 1991. (Cited on page 13).

[26] Sawitree Saengkaew, Tawatchai Charinpanikul, Claire Laurent, Yves Biscos, Gérard Lavergne, Gérard Gouesbet, and Gérard Gréhan. Processing of individual rainbow signals. *Experiments in fluids*, 48(1):111–119, 2010. (Cited on page 13).

[27] Jantarat Promvongsa, Pumyos Vallikul, Bundit Fungtammasan, Annie Garo, Gerard Grehan, and Sawitree Saengkaew. Multicomponent fuel droplet evaporation using 1d global rainbow technique. *Proceedings of the Combustion Institute*, 36(2):2401–2408, 2017. (Cited on page 13).

[28] Pascal Lemaitre, Emmanuel Porcheron, G Grehan, and L Bouilloux. Development of a global rainbow refractometry technique to measure the temperature of spray droplets in a large containment vessel. *Measurement Science and Technology*, 17(6):1299, 2006. (Cited on page 15).

[29] J Badoz, M Le Liboux, R Nahoum, G Israel, F Raulin, and JP Torre. A sensitive cryogenic refractometer. application to the refractive index determination of pure or mixed liquid methane, ethane, and nitrogen. *Review of scientific instruments*, 63(5):2967–2973, 1992. (Cited on page 24).

[30] Chemyx Inc., 10905 Cash Road, Stafford, TX 77477 USA. *Nexus Series User Manual*, January 2016. (Cited on page 31).

[31] FMP TECHNOLOGY GMBH, Fluid measurement and projects. *Monodisperse droplet generator for industrial and university research applications*, 2011. (Cited on pages 31, 63 & 87).

[32] Bengt Edlén. The refractive index of air. *Metrologia*, 2(2):71, 1966. (Cited on page 40).

[33] Corning Inc. *Corning HPFS 7979, 7980, 8655 Fused Silica*, July 2014. Optical materials product information, Specialty materials division. (Cited on page 42).

[34] J. Promvongsa. *On Experimental Study to Evaluate Evaporation Rate of Liquid Fuel Sprays.* PhD thesis, King Mongkut's University of Technology Thonburi, 2013. (Cited on page 88).